1-1-2017

An Effective Methodology For Suppressing Structure-Borne Sound Radiation

Lingguang Chen
Wayne State University,

AN EFFECTIVE METHODOLOGY FOR SUPPRESSING STRUCTURE-BORNE SOUND RADIATION

by

LINGGUANG CHEN

DISSERTATION

Submitted to the Graduate School

of Wayne State University,

Detroit, Michigan

in partial fulfillment of the requirements

for the degree of

DOCTOR OF PHILOSOPHY

2017

MAJOR: MECHANICAL ENGINEERING

Approved By:

_____

Advisor Date

_____

_____

_____

DEDICATION

To my parents

ACKNOWLEGMENTS

As the final project of my Ph.D. journey, this dissertation summarizes all my hard works and efforts during the past 4 years. However, without the help and the support from several individuals, this cannot be made possible. So, I would like to express my sincere thanks to the following individuals here and for the rest of my life.

My deepest gravity goes to my advisor, Professor Sean Wu. The difficulty of gaining my Ph.D. degree is significantly reduced by his knowledge and instruction. Under his guidance, all my research and study are like standing on the shoulders of giants. It is a great honor for me to have the opportunity to further develop and expand theory of HELS (Helmholtz equation least-square) method which Professor Wu has been studied for over 15 years. He is a great mentor not only from the academic point of view but also from the perspective of life. The strong work ethic I learned from him will benefit me for life.

Thanks to Professor Chin-An Tan for his detailed instruction of vibration course and his guidance for my research. His vibration course is my first course at Wayne State University and I'm very impressed by his knowledge and care for students. After that, he also offers me much help for my experiments. Thanks to Professor Emmanuel Ayorinde and Professor Pai-Yen Chen for their careful review and agreeing to serve as my committee member.

Thanks to Dr. Wu Zhu and Dr. Logesh Natarajan for their help for this dissertation. My research is along the same line with their previous works, so, their help greatly relieves the "pain point" of my research. My thanks also extended to Yazhong Lu and Dr. Pan Zhou for their valuable suggestions.

And special thanks to my parents and my fiancée Mengyu Li for their unconditional love and continued support.

Finally, hope this dissertation will not be the end of my academic research journey and hope this sentence is not just a hope.

TABLE OF CONTENTS

LIST OF TABLES

LIST OF FIGURES

CHAPTER 1: INTRODUCTION

1.1 Motivation

In the development process of any product that subjects to mechanical excitation, reducing the radiated noise that is harmful to human health and environment is always a crucial concern. Due to the complexities of predicting the real vibro-acoustic behavior of a structure and utilization of idealistic properties as well as simplified boundary conditions, many noise control targets that are set a design stage cannot be achieved. This causes most noise control tasks, especially structure-borne noise control tasks, to be done at the final stage with respect to a prototype. So, experimental noise diagnoses are widely used in industry.

The key factor of experimentally diagnosing the noise source is to find the interrelationship between structural vibration and resultant sound radiation, which may be summarized as: "While sound is produced by vibrations, not all vibrations can produce sound." This is because the majority of structural vibrations produce the evanescent waves whose amplitudes decay exponentially as they travel away from the vibrating structure. In fact, only a small portion of structural vibrations can produce sound waves that can travel to the far-field. So, identifying and then suppressing the components of structural vibrations that are directly related to sound radiation is the most cost-effective way to reduce noise.

However, many noise reduction strategies that are currently used in industry simply equate noise control to vibration control. Typically, these strategies aim at reducing the noise radiated at certain frequencies (or bands) by suppressing structural vibrations at the same frequencies. More specifically, these approaches attempt to suppress the natural modes or operating deflection shapes of a structure at or near the target frequencies. Such methods are effective for control of vibration, however, but not sound radiation. Because the vibration component that contributes most to noise

radiated at specific frequencies might not necessarily be the nature modes or operating deflection shapes at or near these frequencies. For example, the efficiency in sound radiation for any specific normal mode is often not the highest at its corresponding natural frequency. Therefore, we must first establish the interrelationships between sound and vibration at any frequency and then identify the specific vibration components that are directly related to sound radiation at this frequency.

1.2 Objective

The ultimate goals of this dissertation are to develop an innovative diagnosis technique that enables one to analyze vibro-acoustic responses of a complex structure, identify the most critical vibration components that are directly responsible for sound radiation, and provide guidelines on where to start and how far to go to suppress structural-borne sound, based on the time and resources available.

To this end, we set to two specific tasks. First, we develop a general methodology that may be applicable to an arbitrarily shapes structure, yet convenient to use in practice to determine the interrelationships between structural vibrations and sound radiation. Second, we develop a tool to assess the effectiveness of each vibration components toward sound radiation, thus identifying the most critical vibration components that are directly responsible to the offensive sound radiation.

The first goal is accomplished by reconstructing the vibro-acoustic field generated by an arbitrary shaped vibrating structure. There are many ways to reconstruct vibro-acoustic quantities that include the Fourier transform-based nearfield acoustic holography (NAH), boundary element method (BEM) based NAH, Helmholtz equation least-square (HELS) method-based NAH, as well as empirical approaches based on the reciprocity principle. In this dissertation HELS method-based NAH was selected over other method to identify the interrelationships between surface vibration and resultant sound radiation. The reason of using this approach is that it can handle any geometry with relatively few measurement points, and is suitable for a non-ideal test environment. However,

the original HELS method uses the nearfield sound pressure as input, which can be problematic in practice because more often than not, it is not possible to set an array of measurement microphones around a vibrating structure in a near field. Moreover, setting up a conformal array of microphones around an arbitrarily shaped vibrating structures is extremely time consuming. Scenarios get even worse when there are auxiliary parts around the test object, which makes nearfield sound pressure measurements impossible.

To overcome these practical issues, a modified HELS-based NAH is developed uses a combination of the normal surface velocity and radiated acoustic pressure as inputs. The normal surface velocity distribution can be easily obtained by using a scanning laser vibrometer over the surface areas that are exposed to the laser beam. This strategy significantly simplifies the test setup and data acquisition, because laser measurements are noninvasive, noncontact and may be done at a remote location. For surface area of a target structure that is not accessible to a laser beam, the normal surface velocity distribution is obtained by using a modified HELS method. Meanwhile, in order to correlate surface vibrations to sound radiation, the field acoustic pressures are measured around the target structure. These acoustic pressure data can also be used to improve the accuracy in the reconstruction of the field acoustic pressure. Since the acoustic pressure measurements are taken at certain distances away from the vibrating structure, the measurement setup is very easy to make. Once these measurements are taken, we can reconstruct all vibro-acoustic quantities on the surface of a target structure and the radiated acoustic pressure field. Most importantly, we can establish a correlation between structural vibrations and acoustic radiation.

To analyze relative contribution of each vibration component to sound radiation at various frequencies, a widely-used approach is to calculate the radiation efficiencies of individual normal mode of a vibrating structure. Since analytic solutions to the normal modes only exist for special geometry subject specific boundary conditions, most research papers are focused on calculating

the radiation efficiency of the normal modes of a baffled plate or a cylinder shell. No prior studies have been found on dealing with the radiation efficiency of an arbitrarily shaped geometry. Most importantly, since the normal modes of a vibrating structure are not related to sound radiation, the radiation efficiency calculated in terms of normal modes cannot reveal the true characteristics of sound radiation.

In order to determine the correlations between structural vibrations of an arbitrarily shaped geometry, we propose to expand the transfer function that correlates structural vibrations to sound radiation in terms of the forced vibro-acoustic components (F-VAC). These F-VACs are mutually orthogonal, hence they can be used to uniquely describe sound radiation from an arbitrarily shaped vibrating structure. The efficiencies of all F-VACs are then calculated and ranked. In this way, we identify the most critical component of structural vibrations that is directly responsible for sound radiation.

To validate this new concept, we then compare the effectiveness of noise reduction based on F-VAC analyses and experimental modal analyses of an arbitrarily shaped vibrating structure.

1.3 Outline of Chapters

In this dissertation, we start with reviewing the current techniques that are widely used in industry in Chapter 2. Most of these methods do not even consider the interrelationships between sound and vibration and simply equating noise control to vibration control.

Chapters 3 and 4 present the modified HELS based NAH that takes combined normal surface velocities and radiated acoustic pressure as inputs. This is accomplished by using a laser vibrometer to measure the normal surface velocity on several discrete points that are accessible to a laser beam, and a simple array of microphones to measure the field acoustic pressure. The normal surface velocities over other surface areas that are not accessible to a laser beam are reconstructed by using the modified HELS method. Chapter 3 depicts the mathematical formulations of modified

HELS based NAH together with hybrid regularization techniques. Those theoretical discussions are followed by specific procedures to implement this modified HELS method. Chapter 4 demonstrates a simulation study with respect to a simply-supported baffled plate under different excitation conditions. Meanwhile, the effects of various parameters on reconstruction results are examined through error analyses. These numerical simulation results are used to develop practical guidelines for selecting optimal parameters in using the modified HELS method.

Chapter 5 presents the concept of F-VAC for analyzing the vibro-acoustic responses of an arbitrarily shaped vibrating structure and for identifying the critical vibration components that are directly responsible for sound radiation. Mathematical formulations and physical meanings of F-VAC are discussed and illustrated in detail.

Chapter 6 illustrates the experimental validations of using the concept of F-VAC to reduce sound radiation from an arbitrarily shaped cookies box. A Bluetooth speaker is used to excite this box from the inside and sound radiation from this box is measured by a simple array of microphones. Once the critical F-VACs that are directly responsible for sound radiation from this box are identified, damping tapes are applied at a few discrete locations to dampen specific F-VACs. The modified structure is excited by the same signal from the inside, and the acoustic pressures at the same locations outside the box are measured by the array of microphones. The same noise reduction measures are applied to this box based on an experimental modal analysis and the radiated acoustic pressures at the same locations are measured. The effectivenesses of noise reduction using F-VAC and experimental modal analysis are compared.

Conclusions of the present dissertation are drawn and presented in Chapter 7. Future work to further improve this innovative noise control strategy is outlined as well.

CHAPTER 2: LITERATURE REVIEW

This chapter reviews current noise diagnosis and vibro-acoustic analysis techniques that target at the structural borne noise. The pros and cons of each involved technique are presented. This review is divided into three parts. First, traditional structural borne noise control approaches that widely used in industry are investigated. Then, characterization methods for vibro-acoustic responses of a vibrating surface are reviewed. Finally, based on analyses and comparisons of these current state-of-the-art techniques, we investigate the possibility of developing an innovative methodology to do structure borne noise control in a cost-effective manner.

2.1 Structural borne noise control strategies

Conventional experimental noise control strategies can be divided into three categories: pure modal analysis based noise control, acoustic radiation analysis based noise control and frequency response function (FRF) reciprocity based noise control. From section 2.1.1 to section 2.1.3, I will only introduce the basic concepts and development histories of these methodologies. And in section 2.1.4, their advantages and limitations will be discussed.

2.1.1 Modal analysis based approaches

In many industrial applications, controlling structure-borne noise at certain frequencies/ bands is just simply equated to controlling vibration at the same frequencies/bands. Two well-developed experimental vibration analysis techniques are: Experimental Modal Analysis (EMA) and Operational Modal Analysis (OMA).

The traditional EMA[1,2] is done in the laboratory and excited with known sources (impulse, broadband, sine wave, swept sine wave, chirp etc.). The vibration characteristics (natural frequencies, normal mode shapes, frequency response functions, damping factors etc.) then thus be determined through evaluation of transfer functions between the excitation source and measured vibration response. The main restriction of conventional modal analysis approach is that the test is

done out of the operating environment, the real operation conditions are difficult to simulate in the laboratory environment. What's more, due to the complexity or size of certain structures, artificial excitations sometimes are hard to implement.

To circumvent these difficulties, OMA is developed later[3,4]. OMA aims at obtaining structural modal properties based on measurement of vibration information when the target structure is running at its normal working condition. Except for OMA's capability of obtaining modal properties while the structure is running, another advantage of OMA is that it does not need any information of excitation signals. The vibration responses are the only input information of the determination process.

2.1.2 Acoustic radiation analysis based approaches

Unlike the widely used pure modal analysis based approaches, in academia, there is a consensus that reduction of sound radiation from vibrating structures should be based on analysis of structural acoustic radiation.

The structure borne sound radiation is traditionally evaluated by the acoustic radiation efficiency. Acoustic radiation efficiency, especially regarding thin plate, has been studied extensively since the 1960s. Acoustic radiation efficiency is usually calculated with modal summation, so the radiation efficiency of a single mode is also called modal radiation efficiency. Note that, in literature, both the name "radiation efficiency" and "radiation resistance" are used. Radiation efficiency is just normalized radiation resistance with respect to surface geometry and medium characteristics. Mathematically, it is defined by

$$\sigma = \frac{R_{rad}}{\rho c S} = \frac{W_{rad}}{\rho c S \left\langle \overline{v^2} \right\rangle}, \tag{1.1}$$

where R_{rad} represents radiation resistance, W_{rad} represents sound power radiated from vibrating surface, S represents the area of the target surface, $\langle \overline{v^2} \rangle$ represents the mean square of normal

surface velocities distribution on the vibrating surface, ρ and c are density and speed of sound in the propagating medium.

In 1962, Oideon Maidanik[5] put forward statistical approach to estimate the structure vibrating response of ribbed panels to acoustic excitation. The radiation resistance of ribbed panel in the whole frequency range under different wavenumber regions are investigated. Effects of various boundary conditions are also studied theoretically and experimentally.

Then, in 1972, numerical integrations seeking approximation solutions for single modal radiation efficiency of baffled beam and rectangular panel are presented by Wallace[6,7]. The radiation resistance corresponding to the individual mode is calculated in terms of the acoustic power radiated to the far field. Approximations for modes of frequency above, about and below the critical frequency are clearly simulated. The effects of radiation efficiency of the inter-nodal areas and pertaining aspect ratio are also investigated.

Thereafter, many other studies focus on different aspects are published. Gomperts[8] examined the acoustic radiation efficiency of a baffled rectangular plate under general boundary conditions. The results show that enforcing constraints in edge areas might not always increase acoustic waves radiated into far field. He also found that the radiation efficiencies of two-dimensional vibration patterns differ rather considerably from those for one-dimensional vibration patterns. Heckl[9] analyzed radiation pattern of planer sources by using a Fourier transform approach in wavenumber domain. Leppinton etc.[10] published several asymptotic formulae to estimate radiation efficiency of different regions of plate wavenumber space, especially for the region near critical frequency and large structural wavenumber. Williams[11] proposed a series of expansions in ascending powers of structural wavenumber k for analyzing sound power originated from planer sources. Mathematical model for approximating acoustic power radiated at low frequencies of

rectangular thin baffled plate under different boundary conditions are derived through Fourier transform of surface velocity and its corresponding derivatives in wavenumber domain.

The above researchers focus on modal radiation efficiency of certain individual mode. Thus, the total radiation power is simply calculated by the sum of contributions from each involved mode. By ignoring cross coupling effects between each mode, the attendant side effects are obvious. This problem has long been realized and the main reason of still doing so is simply because of computational complicity. So many scholars developed various optimization algorithms that take modes coupling into consideration.

Keltie and Peng[12] published a paper specialized the modal coupling effects on the acoustic power radiation from panels with finite long and finite width. Their results show that cross coupling of modes play a more important role for acoustic waves radiated at low frequency and off-resonant frequencies. Targeted on low-frequency range same as that of the individual modal radiation efficiencies, Snyder[13] derived a set of simpler formulations based on Fourier transforms. Later, Li etc.[14] also examined in detail about physical characteristics of cross-modal coupling and their corresponding impacts on the radiation power. Based on those analyses, they show that the mutual terms caused by the cross-modal coupling can be calculated easily and accurately in the whole frequency range, even at resonant frequencies.

Having the acoustic power radiation estimated in terms of the contributions from the individual normal mode, the results are used to design either passive or active structural borne control strategies.

Passive noise control seeks to reduce sound radiation by the modification of the vibrating structure itself. Koorosh etc. [15] examined a material tailoring approach to optimize structure for minimizing sound power radiation. The first and foremost part of implementing this strategy is to establish a mathematical model of structure's vibration-acoustic response in terms of material

properties desired to be optimized. The mathematical model is then combined with the vibro-acoustic model to give out the radiated sound power for the optimization analysis. The variances of the acoustic radiation corresponding to structure property are used as indicators to determine optimum structure parameters which minimize the power radiated into the far field. The tailored structure with minimum acoustic radiation is designated as "weak radiator" by Koopmann and Fahnline.[16] They were the first few, among many others, scholars to examine the physical properties of the weak radiator. Thereafter, many other researches are conducted.

Active structural acoustic control is a more recently developed technique utilizing vibration sensors and secondary actuators to reduce the sound radiation from vibrating structures. In the early 1990s, Fuller etc. applied time-domain least mean square adaptive feedforward control techniques to reduce sound radiation by using point force or acoustic control inputs analytically[17] and experimentally[18]. More recently, piezoelectric sensors and actuators mounted on the surface are used to control noise radiation not only from rectangular plates but also from cylinder shells[19]. Basically, most of the active structural borne noise control approaches focus on the development of control algorithms. For example, to tackle broadband structural actuation, the traditional least mean square algorithm need to be combined with a semi empirical model that related to input and output[20]. This method has been shown good noise reduction results, especially for the lightly damping structures.

2.1.3 FRF-reciprocity based approaches

FRF-reciprocity[21] based approaches aim at controlling sound pressure levels at some pre-selected filed point locations by suppressing vibration of localizing areas. Two representatives of these approaches are transfer path analysis (TPA)[22] and panel contribution analysis (PCA)[23]. Of course, the fundamental of these approaches is frequency response function (FRF) between structural vibration and radiated acoustic waves at certain pre-selected filed point locations.

TPA enable one to identify the structure-borne as well as air-borne sound transfer path between excitation sources and targeted receiver locations in the sound reduction process. Instead of examining the whole structure, TPA restricts itself to carefully chosen measurement filed points including excitation source locations, transfer path locations, and receiver locations. Based on the measurement results, the contributions of each source locations to sound pressure levels at selected receiver locations, as well as sound transfer paths can thus be determined through reciprocity principle. PCA also based on FRF-reciprocity principle, however, unlike TPA, it takes measurements over the whole vibrating structure. Then the whole source surface is artificially divided into several panels/areas. Except for the difference of source measurement, PCA and TPA use the similar technique to identify the contribution of source points/panels to sound radiation at pre-selected field receiver locations. The noise control strategies based on these FRF-reciprocity analyses are simply to suppress vibration at dominant source locations or disturb the strongest transfer path of target propagated sound.

2.1.4 Discussion

There are many common beliefs in industrial areas. Since structural borne noise control can be accomplished through vibration control, they simply equate noise control to vibration control. More specifically, suppressing certain vibration at one frequency/band could effectively eliminate sound radiated at the same frequency/band. In particular, suppressing a flexural structure's resonance can reduce the sound at corresponding resonant frequency effectively. These common concepts are obviously not true. Sound radiation from vibrating structure is totally different physical phenomenon from structural vibration. The sound radiation is related not only to distribution of surface vibration but also connected with surrounding radiation environment and geometry shape of the source structure itself. The previous mentioned EMA and OMA analysis are very useful for suppression of the vibration at certain frequencies, however, they could not

provide interrelationships between vibration and resultant sound radiation. So, the two widely used conventional vibration analysis techniques are always proved either ineffective or cost prohibitive.

This problem has been noticed by almost all the peer-reviewed academic papers for a long time and this is also one of the main motivations for the development of radiation efficiency analysis. It is well known that acoustic radiation efficiency reveals the contribution of each vibration mode to overall sound radiation power at certain frequency/band. Based on these results, structural noise control of rectangular plates and cylinder shells have been achieved in both passive and active manner. However, what acoustic radiation efficiency provided is the comprehensive effect of all the factors mentioned above, the acoustic radiation behavior could not be completely reflected. In other words, acoustic radiation efficiency describes the contribution of vibration component to sound radiation in terms of normal modes, whereas the acoustic radiation of certain points on the structural surface cannot be shown. Thus, it cannot give out direct guide for noise control strategies. For example, it cannot answer the questions of how many actuators are needed and where they should be placed for active structural borne noise control. Structural noise control based on acoustic radiation efficiency analysis can only be effectively accomplished by suppressing many high radiation efficiency modes together. Noise control strategy with respect to only one or two dominant modes cannot provide you best noise reduction results. Also, although acoustic radiation efficiency has been studied for few decades, most of current available researches and applications are still restricted to regular geometry shape structures. Acoustic radiation efficiency analysis of arbitrary shape structures is seldom mentioned.

Compared with pure vibration model analysis based noise control and acoustic radiation analysis, based vibro-acoustic analysis, the FRF-reciprocity based vibro-acoustic analysis do establish certain interrelationships between source vibration and resultant sound radiation and is not subject to geometry shape restrictions. However, TPA and PCA are restricted to the pre-

selected measurement locations and not effective at other non-examined locations. The thus obtained interrelationships cannot be extended to the whole vibrating surface and all field points. In air-borne noise control, the noise sources can be abstracted into several discrete point sources, this may not be a big problem. However, for structural-borne sound, vibration behavior of the whole structure need to be considered, so accurately identify the dominant structural vibration component that responsible for sound radiation by using reciprocity method need an excessive number of measurement points. This is not practical and not cost-effective.

After reviewing of the current state-of-the-art techniques and their pros and cons, we can found that establishing the interrelationships between sound and vibration in the most cost-effective manner is crucially important to effectively control structural borne noise. So, in next subsection, vibro-acoustic analysis strategies could be used to correlate structural vibration with sound radiation will be reviewed.

2.2 Vibro-acoustic analysis strategies

To predict sound radiated from vibrating surfaces experimentally, we can do the following three analyses: acoustic radiation efficiency analysis, empirical approaches based on reciprocity principle, and nearfield acoustic holography (NAH).

As discussed above, the first two approaches have already been applied to structural noise control for decades, whereas their limitations are obvious. Experimentally identification of model radiation efficiencies of arbitrary structure is difficult. Even radiation efficiencies are obtained, the results are of course expressed in terms of structure's normal modes and which exact locations vibration contribute most to sound radiation at target frequency cannot be given directly. For reciprocity principle based vibro-acoustic analysis, the most significant advantage is its simplicity in formulation and flexibility in application. No matter how complex the test objects are and how many obstruct reflecting surfaces exist in the environment, the vibrating surface is all represented

by simple sound sources. However, regardless how many measurement points are taken to get the transfer matrices, the obtained acoustical quantities are discrete in space and only valid at measurement points. The transfer function between every surface point's vibration and every field location's sound pressure are not available. Thus, the dominant vibration component that directly responsible for noise radiation cannot be further identified.

These above problems that conventional vibro-acoustic analysis techniques encountered can be overcome by NAH. Through NAH, every vibro-acoustic quantity includes the sound pressure, the normal component of the particle velocity, and acoustic intensity at any field point as well as the interrelationships between surface vibration and radiated sound can all be reconstructed. However, applications of NAH technology in structural noise control are seldom discussed previously. So, in this subsection, we focus on reviewing different current implementation approaches of NAH. Over the past several decades, several different NAH implementations have been developed, including Fourier transform based NAH, boundary element method (BEM) based NAH, and Helmholtz equation least-square (HELS) method based NAH as well as some other attempts trying to circumvent difficulties encountered in practice.

2.2.1 Fourier transform based NAH

Fourier transform based NAH is evolved from acoustical holography[24] which uses similar approaches as those of laser holography and takes the measurement in the far field. From acoustical holography to NAH, the most significant progress is the inclusion of nearfield information. Without this nearfield information, which is physically expressed as evanescent waves, the spatial resolution is restricted to the wavelength of the interested acoustic wave. In other words, the acoustic waves originated within a distance less than a wavelength cannot be properly discerned. This is not a problem for laser holography, since the wavelengths of the laser are nanoscale, so its spatial resolution is extremely high even without nearfield information included.

In the early 1980s, the original Fourier transform based sound radiation analysis is theatrically illustrated and numerically simulated by Williams and Maynard.[25,26] Then, in 1985, the concept of NAH[27] is put forwarded and detail instructions for implementation[28] is given. Thereafter, the original planner NAH is expanded to cylindrical shapes by using a so-called generalized NAH[29]. The application of Fourier based NAH was also extended to broadband low frequency excitation with respect to cylinder shells[30].

As its name suggests, Fourier transform based NAH reconstructs the vibro-acoustic field by using temporal and spatial Fourier transforms. The obtained time domain sound pressures are transferred to the corresponding frequency domain and then another spatial Fourier transform projects them onto wavenumber domain. In wavenumber domain, the sound pressures on hologram surface can be projected to any parallel surfaces in a source-free region through transfer functions. Once this is done, sound pressure at any filed points in the time domain can be reconstructed through inverse spatial and temporal Fourier transform.

. However, Fourier transform requires an equal interval in each dimension. So, it is only applicable to standard surfaces with a constant coordinate no matter in Cartesian, cylindrical or spherical coordinates. More specifically, the planar surface with constant z coordinate, cylindrical surface and spherical surface with a constant radius. Also, it is only valid for an unbounded source-free region. In other words, if a confined or partially confined space which includes several reflecting surfaces or a medium that contains other sources are desired, the Fourier transform-based NAH will no longer be suitable.

2.2.2 BEM based NAH

For an arbitrarily shaped surface, no analytic solution of Helmholtz integral equation is available. A commonly used approach seeks to find the numerical solution is BEM-based NAH. It divides the target surface into several segments, each of which is represented by a finite number

of nodes and a set of element equations to the original Helmholtz integral equation. The vibro-acoustic quantities anywhere in the field can be calculated by multiplying the inverse transfer matrix and the sound pressures on the measured surface.

Gardner and Bernhard are among the first few scholars that investigate the potential of using a numerical method to reconstruct the acoustic quantities of an interior region bounded by arbitrarily shaped structures[31]. The formal theoretical derivation of using inverse finite element method based NAH to analysis interrelationships between structural vibration on the source surface and acoustic quantities at any field points in an interior region were given by Veronesi and Maynard.[32] Then, the BEM-based NAH which is an improvement and expansion of previous works was developed by Huang.[33] In 1992, a more complete deception of BEM-based NAH, as well as several numerical simulation examples were given by Bai.[34]

The main advantage of BEM-based NAH is its capability of reconstruction of the acoustic quantities of an arbitrarily shaped structure. It does not need the measurement locations to be equally distributed on the holography surface so long as these measurement points are in the nearfield. Also, unlike Fourier transform based NAH which requires the reconstruction points located at plane parallel with holography plane, BEM-based NAH is suitable for any points on the source surface or in the free field. However, enormous numerical computation is its main disadvantage. Since the source surface is discretized into many elements, in order to acquire satisfactory reconstruction spatial resolution, one must ensure a minimum number of sampling points per wavelength. This is especially true when it tries to account for the nonuniqueness difficulties encountered at the characteristic frequencies.

2.2.3 HELS method based NAH

Unlike Fourier transform or BEM based NAH, HELS method seeks the best approximation of the vibro-acoustic field by expressing the solution of Helmholtz equation under spherical

coordinate as expansions of certain spherical basis functions. HELS approach greatly simplifies the reconstruction process, yet still, ensures its capability to tackle arbitrarily shapes source surface with relatively few measurement points. The expansion coefficients associated with these basis functions are determined by matching the assumed solutions to the measured sound pressures, and then the errors are minimized by least squares.

In 1997, the theoretical foundation and two numerical examples of HELS based NAH were published by Wang and Wu.[35] Later in 2000, numerical simulation with respect to a full-size four-cylinder engine[36] and experimental validations for acoustic radiation from a simulated front end of passenger vehicle[37] were presented. Satisfactory results were obtained under both random and harmonic excitations. Thereafter, implementation of HELS theory has been expanded to many areas. It has been combined with BEM-based NAH to simply BEM approach's measurement scheme.[38] With sound pressures measured at relatively few nearfield locations, the more additional field points' acoustic pressures were regenerated by using HELS approach, and then the whole data set is used as the input for BEM-based NAH to reconstruct the vibro-acoustic field. It has also been extended to reconstruct acoustic radiation from a spherical surface that subjects to transient excitations in the free field.[39] A technique named panel acoustic contribution examination method based on HELS based NAH has been developed to simplify the determination process of critical vibration component that directly responsible for sound radiation from enclosed arbitrarily shapes structures.[40]

HELS approach solves the Helmholtz equation directly and always lead to unique optimized solutions at all frequencies, so it is immune to the nonuniqueness difficulty encountered in BEM based NAH. HELS based NAH tackles that reconstruction problem by matching measured data with assuming form solutions, so its reconstruction accuracy heavily related to the quality of input data as well as whether the assumed solution fit the target vibro-acoustic field. This is where

the main limitations of HELS approach lay on. The measurement errors embedded in the input data and disturbance from background noise is inevitable in practice. There is also no one fit all set of assumed solutions that yield good reconstruction for all kinds of geometry surfaces. For example, the chosen spherical coordinate system is good for convex surface but not for some highly-elongated surface such as flat of slender bodies. All these difficulties can only be circumvented to some extent by applying suitable regularization techniques.

2.3 Proposed F-VAC analysis based on modified HELS approach

After reviewing current techniques available for structural borne noise control, we can confidently draw a conclusion that the core factor about finding the most cost-effective way to do noise control is establishing certain relationships between resultant sound radiation and structural vibration. More specifically, the components of structural vibrations that are directly responsible for unwanted sound radiation need to be identified based on vibro-acoustic correlations reconstruction.

NAH is a perfect technique to acquire such interrelationship. For the implementation of NAH, HELS method based NAH is selected over the others for its simplicity in formulation, efficiency in computation and flexibility in application. The original HELS based NAH uses sound pressure acquired in the nearfield as inputs. In order to take sound pressure measurements in the nearfield with respect to arbitrary shape structure, it is necessary to design unique conformal microphone array for every different test object which is not economic. It is very time-consuming for engineers to assemble the special microphone array to ensure equal normal distance between each measurement points and source surface. An important rule of thumb of any technique that is intended for industry application is ease of use. To simplify its application, the original HELS algorithm is modified to utilize normal surface particle velocities as inputs. The normal surface velocity can be easily obtained by using a scanning laser vibrometer which significantly facilitates

test setup and data acquisition. What's more, acoustic quantities measured just on the surface contains more nearfield effects that are very helpful for achieving accurate reconstruction of the whole vibro-acoustic field.

Through modified HELS based NAH, we can establish the interrelationships between structural vibration and acoustic radiation. These interrelationships can lead directly to transfer matrices between forced vibration and sound radiation, which are calculated but not measured. Then, this transfer matrices are further decomposed into several F-VACs, which indicate the dominant structural vibration of the undesired sound radiation.

In summary, the vibration components that are directly responsible for sound radiation can be determined by expanding the surface vibration in terms of the F-VACs. The critical vibration component can be identified by calculating the relative contributions of F-VACs responsible for target noise radiation. Target noise reduction can be achieved by suppressing the critical vibration component (dominant F-VAC) thus identified. Such an approach will yield target noise reduction in the most cost-effective manner.

CHAPTER 3: THEORY OF MODIFIED HELS METHOD BASED NAH WITH NORMAL SURFACE VELOCITY AS INPUT

In this chapter, the proposed modified HELS based NAH approach will be presented in detail, including mathematical model and specific implementation procedures. A complete derivation of fundamental spherical wave functions and original HELS algorithm could be found in previous publications.[41,42] This dissertation will focus on the modification part of how to reconstruct vibro-acoustic field by using normal component particle velocities measured just on the source surface.

3.1 Introduction

Since the early 1980s, many NAH implementation methods, including Fourier transform based NAH, BEM-based NAH, HELS method based NAH as well as other attempts trying to circumvent difficulties encountered in practice, have been developed. In the majority of these conventional NAH approaches, the inputs are sound pressures obtained in the nearfield.

Attempts of using alternative acoustic quantities as inputs could date back to as early as 1988. Loyau etc. proposed a so called broadband acoustic holography from intensity measurements (BAHIM).[43] The BAHIM method is implemented by means of energy measurements including acoustic intensity vector and potential energy density. Numerical simulations and experimental verifications all perform acceptable vibro-acoustic field reconstruction results.

In 2005, Jacobsen and Liu first considered using particle velocities directly measured by a particle velocity probe as inputs to do planner NAH.[44] The particle velocity in this approach is obtained by using particle velocity sensors take measurements in the nearfield. The numerical simulations indicate similar reconstruction accuracy to traditional pressure to pressure reconstruction. And the velocity to pressure reconstruction performs even better for backward reconstruction. Then, Leclère and Laulagnet[45] published a similar technique yet the particle

velocities were obtained by measuring vibration response of a light tensionless membrane artificially placed in the holography plane. Satisfactory reconstruction results are also obtained.

Harris etc. published a method with the representation of the pressure field at the holography plane obtained by a combination of near-field sound pressure and in-plane particle velocity measurements.[46] In this approach, the sound pressures and two orthogonal in-plane particle velocities are measured simultaneously by using a pressure-velocity (P-U) probe. Results show that with both sound pressure and particle velocity information available, total measurement locations can be decreased by approximately 70%.

Zhang etc. compared the performance of implementing NAH based equivalent source method (ESM) with different types of input.[47] Saying ESM based on measurement of sound pressure, ESM based on measurement of particle velocity and ESM based on hybrid measurement of both sound pressure and particle velocity. The numerical simulation demonstrated that the reconstructions using the hybrid P-U method agree better with benchmark data than that of only using sound pressure or particle velocity.

In general, the input information of current NAH implementations is acoustic quantities, either acoustic pressure, acoustic intensity or particle velocity, that measured on a holography surface at a standoff distance to the source surface. For obvious reasons, the standoff distance is set as small as possible. Is it possible to set the standoff distance zero? In other words, is it possible to use acoustic quantities on the source surface, instead of on a holography surface, as inputs, yet still in a non-contact manner? If so, theoretically, more nearfield effects (evanescent waves) can be captured, thus might achieve better reconstruction results.

To answer this question, first, we need to figure out what kind of acoustic quantities on the source surface could be measured directly. Currently, it is very difficult to obtain surface acoustic pressure and surface acoustic intensity directly, however, the normal component of particle

velocity on the surface is measurable by using scanning laser vibrometer taking measurements at a distance.[48] Then after carefully studying the potential of using normal surface velocity as inputs, a modified HELS based NAH is developed. The description and application of this method have already been discussed by Zhu[49] and Chen[50] recently. In this and the following chapter, along with the same line as these previous works, more complete theory illustration and extensive numerical simulations are demonstrated. Based on these results, guidelines for selection of regularization parameters and implementation process are explained in detail.

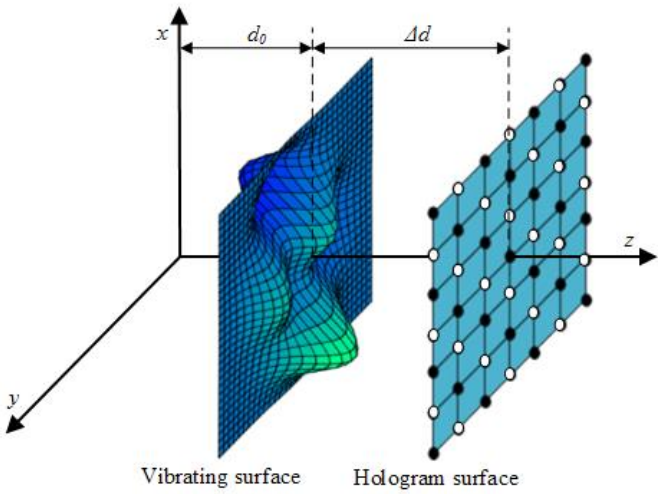

Figure. 3.1 Sketch illustrating the test setup

The proposed normal surface velocity measurements based NAH is sketched in figure 3.1. Since spherical expansion functions are used to generate assumed solutions in HELS approach, the coordinate origin must be moved out of the vibrating surface and placed at a distance d_0 from the vibrating surface on the opposite side of the surface where the vibro-acoustic field are to be predicted. The Cartesian coordinates are oriented in such a way that the *z*-axis is in the normal direction of the plate, and *x* and *y* axes are in transverse and longitudinal directions, respectively.

The normal surface velocities are certainly measured just on the vibrating surface. The prediction distance is designated as Δd.

3.2 Mathematical model

Consider a complex vibrating structure radiating sound at frequency ω into an unbounded fluid medium. The HELS model assumes that the radiated sound pressure can be expressible as a superposition of a finite number of spherical expansion functions that governed by the Helmholtz equation under Sommerfeld radiation condition. Mathematically, the radiated sound pressure at location $\vec{x}$ on the holography plane can be expressed in matrix form as

$$\left\{\hat{p}\left(\mathbf{x}_i;\omega\right)\right\}=\sum_{j=1}^{J}\psi_j(\mathbf{x}_i;\omega)C_j(\omega), \tag{3.1}$$

where $\left\{\hat{p}\left(\mathbf{x}_i;\omega\right)\right\}$ represents the complex amplitude of the radiated acoustic pressures at desired reconstructed field points, $\psi_j(\mathbf{x}_i;\omega)$ represents j^{th} expansion function that is particular solution to the Helmholtz equation and $C_j(\omega)$ represents unknown expansion coefficients related to corresponding expansion function and J is the number of expansion functions included.[51] Assume that N number of points are targeted on the holography plane, for easy illustration later, equation (3.1) is rewritten in matrix form as

$$\left\{\hat{p}\left(\mathbf{x};\omega\right)\right\}_{N\times 1}=\left[\Psi\left(\mathbf{x};\omega\right)\right]_{N\times J}\left\{C\left(\omega\right)\right\}_{J\times 1}, \tag{3.2}$$

where $\mathbf{x}=[\mathbf{x}_1,\mathbf{x}_2,\ldots\mathbf{x}_N]$ represent the location vectors of all N prediction points; sound pressure $\hat{p}\left(\mathbf{x};\omega\right)$ and expansion coefficients $\{C(\omega)\}$ are row vectors expressed as $\hat{p}(\mathbf{x};\omega)=\{\hat{p}(\mathbf{x}_1;\omega),\hat{p}(\mathbf{x}_2;\omega),\ldots\hat{p}(\mathbf{x}_N;\omega)\}$ and $C(\omega)=\{C_1(\omega),C_2(\omega),\ldots C_J(\omega)\}$ respectively; the expansion function $\psi_j(\mathbf{x}_i;\omega)$ is the i^{th} row and j^{th} column entry of expansion matrix $[\Psi(\mathbf{x};\omega)]$. Under spherical coordinates, the expansion functions are expressed in terms of spherical Hankel functions and spherical harmonics. The specific format of the assumed solutions will depend on

geometry shape of holography surface as well as if it is an interior or exterior problem. For exterior problem, the spherical Hankel functions of the first kind is involved

$$\psi_j(\mathbf{x}_i;\omega)=\psi_{n_j l}(r_i,\theta_i,\phi_i;\omega)=h_{n_j}^{(1)}(kr_i)Y_{n_j}^{l_j}(\theta_i,\phi_i). \tag{3.3}$$

and for the interior problem, spherical Hankel function of the second kind is used

$$\psi_j(\mathbf{x}_i;\omega)=\psi_{n_j l}(r_i,\theta_i,\phi_i;\omega)=h_{n_j}^{(2)}(kr_i)Y_{n_j}^{l_j}(\theta_i,\phi_i). \tag{3.4}$$

The normalized spherical harmonic is formulated by angle functions and expressed as

$$Y_{n_j}^{l_j}(\theta_i,\phi_i)=\sqrt{\frac{(2n_j+1)(n_j-l_j)!}{4\pi(n_j+l_j)!}}P_{n_j}^{l_j}(\cos\theta_i)e^{\sqrt{-1}l_j\phi_i}, \tag{3.5}$$

where $P_n^l(\cos\theta)$ is Legendre function of the first kinds. The scripts j, n_j and l_j are related via $j = {n_j}^2 + n_j + l_j + 1$ with n_j range from 0 to N^* and l_j range from - n_j to n_j. Thus, for each combination of n_j and l_j, j could change from 1 to $(N^*+1)^2$. Hence, we have the maximum number of expansion functions $J=(N^*+1)^2$.

The spherical Hankel functions of order n_j of the first kind and second kind are represented in terms of spherical Bessel function of the first kind $j_{n_j}(kr_i)$ and spherical Bessel function of the second kind $y_{n_j}(kr_i)$ as follows

$$h_{n_j}^{(1)}(kr_i)=j_{n_j}(kr_i)+iy_{n_j}(kr_i), \tag{3.6}$$

$$h_{n_j}^{(2)}(kr_i)=j_{n_j}(kr_i)-iy_{n_j}(kr_i). \tag{3.7}$$

Formulation of these spherical basic functions are readily available in many libraries, so they will not be given here. Having the assumed-form formulations, next, we will derive the reconstruction process for normal surface velocity, sound pressure, and acoustic intensity respectively.

3.3 Solution of reconstructing acoustic quantities

3.3.1 Solution of reconstructing normal particle velocity

Note that in this proposed modified HELS approach, normal surface velocity measured by laser vibrometer are used as inputs to predict the whole vibro-acoustic field. For continuous reasons, the measured normal surface velocity is equal to the acoustic particle velocity on the surface. The particle velocity is related to sound pressure through the Euler's equation

$$\rho_0 \frac{\partial \vec{v}}{\partial t} = -\nabla p, \tag{3.8}$$

where ρ_0 is the ambient density of the fluid medium. Its Fourier transform yields

$$i\omega\rho_0 \hat{v} = \nabla \hat{p} \bullet \vec{n}, \tag{3.9}$$

where $\vec{n}$ is unit vector in normal direction on the source surface. Assume that normal surface velocities at L locations are measured by laser vibrometer. To this end, gradient in the direction orthogonal to the surface is taken with respect to equation (3.2) and combined with Euler's equation lead to

$$i\omega\rho_0 \left\{\hat{v}_n\left(\mathbf{x}_l^{meas};\omega\right)\right\}_{L\times 1} = \left\{\nabla\left[\Psi\left(\mathbf{x}_l^{meas};\omega\right)\right]\cdot\vec{n}\right\}_{L\times J}\left\{C(\omega)\right\}_{J\times 1}, \tag{3.10}$$

where $\left\{\hat{v}_n\left(\mathbf{x}_l^{meas};\omega\right)\right\}_{L\times 1}$ represents normal components of particle velocity on the surface at L locations. And J is the total number of expansion terms. The gradient of spherical expansion functions is given by

$$\left\{\nabla\left[\Psi\left(\mathbf{x}_l^{meas};\omega\right)\right]\right\}_{L\times J} = \left\{\left(\frac{\partial}{\partial r}\vec{e}_r + \frac{1}{r}\frac{\partial}{\partial\theta}\vec{e}_\theta + \frac{1}{r\sin\theta}\frac{\partial}{\partial\phi}\vec{e}_\phi\right)\Psi\left(\mathbf{x}_l^{meas};\omega\right)\right\}_{L\times J}, \tag{3.11}$$

where $(\vec{e}_r, \vec{e}_\theta, \vec{e}_\phi)$ represent unit vectors in each spherical coordinate directions. The partial differentiation of $\Psi\left(\mathbf{x}_l^{meas};\omega\right)$ with respect to r, θ and ϕ can be calculated as follows

$$\frac{\partial \Psi(\mathbf{x};\omega)}{\partial r} = \frac{\partial}{\partial r}\left[h_n(kr)\right] Y_n^l(\theta,\phi),$$

$$\begin{aligned}\frac{\partial \Psi(\mathbf{x};\omega)}{\partial \theta} &= h_n(kr)\frac{\partial}{\partial \theta}\left[Y_n^l(\theta,\phi)\right] \\ &= \sqrt{\frac{(2n+1)(n-l)!}{4\pi(n+l)!}} e^{il\phi} h_n(kr)\frac{\partial}{\partial \theta} P_n^l(\cos\theta),\end{aligned} \tag{3.12}$$

$$\begin{aligned}\frac{\partial \Psi(\mathbf{x};\omega)}{\partial \phi} &= h_n(kr)\frac{\partial}{\partial \phi}\left[Y_n^l(\theta,\phi)\right] \\ &= il\sqrt{\frac{(2n+1)(n-l)!}{4\pi(n+l)!}} h_n(kr) P_n^l(\cos\theta) e^{il\phi}.\end{aligned}$$

More specifically, partial differentiation of spherical Hankel function with respect to r and partial differentiation of Legendre function with respect to θ are given as follows

$$\frac{\partial}{\partial r}\left[h_n(kr)\right] = \begin{cases} k\left[h_{n-1}(kr) - \dfrac{n+1}{kr} h_n(kr)\right] & (n \geq l) \\ \left(ik - \dfrac{1}{r}\right) h_0(kr) & (n=0) \end{cases}, \tag{3.13}$$

$$\frac{\partial}{\partial \theta} P_n^l(\cos\theta) = \frac{-(n+1)\cos\theta P_n^l(\cos\theta) + (n-l+1) P_{n+1}^l(\cos\theta)}{\sin\theta}. \tag{3.14}$$

In equation (3.10), having the velocity measured by laser vibrometer $\left\{\hat{v}_n\left(\mathbf{x}_l^{meas};\omega\right)\right\}_{L\times 1}$ and gradient of spherical expansion functions $\left\{\nabla\left[\Psi\left(\mathbf{x}_l^{meas};\omega\right)\right]\right\}_{L\times J}$ governed by source geometry shapes, the only unknown factor is expansion coefficients $\left\{C(\omega)\right\}_{J\times 1}$. Mathematically, equation (3.10) is an inconsistent system of equations consisting of L number of equations and J number of unknowns. When $J \leq L$, we have an overdetermined system and when $J > L$, the problem turns out to be underdetermined. Although even the underdetermined system could be solved by singular

value decomposition, the reconstruction accuracy may be reduced. Therefore, the number of expansion terms is set to be no larger than that of the number of input points.[52]

To solve this inconsistent system of equations, pseudoinverse approach is considered. Theoretically, the unknown expansion coefficients $\left\{C(\omega)\right\}_{J\times 1}$ can thus be obtained by taking a pseudo inversion of gradient of expansion functions,

$$\left\{C(\omega)\right\}_{J\times 1} = i\omega\rho_0 \left\{\nabla\left[\Psi\left(\mathbf{x}_l^{meas};\omega\right)\right]\right\}^{\dagger}_{J\times L} \left\{\hat{v}_n\left(\mathbf{x}_l^{meas};\omega\right)\right\}_{L\times 1}, \tag{3.15}$$

where a superscript † implies a pseudo inversion of a rectangular matrix defined as

$$\left\{\nabla\left[\Psi\left(\mathbf{x}_l^{meas};\omega\right)\right]\right\}^{\dagger}_{J\times L} = \left\{\left\{\nabla\left[\Psi\left(\mathbf{x}_l^{meas};\omega\right)\right]\right\}^{H}_{J\times L} \left\{\nabla\left[\Psi\left(\mathbf{x}_l^{meas};\omega\right)\right]\right\}^{\dagger}_{L\times J}\right\}^{-1} \left\{\nabla\left[\Psi\left(\mathbf{x}_l^{meas};\omega\right)\right]\right\}^{H}_{J\times L}, \tag{3.16}$$

where the superscript *H* represents the Hermitian transpose of a matrix. Note that HELS method requires that the number of reconstruction points no more than number of measurement points. So, assume that the normal components of particle velocities at *S* ($S \le L$) locations need to be reconstructed. Regarding normal surface velocity at *S* reconstructed locations $\mathbf{x}_s^{rec}$, equation (3.10) can be rewritten as

$$i\omega\rho_0 \left\{\hat{v}_n\left(\mathbf{x}_s^{rec};\omega\right)\right\}_{S\times 1} = \left\{\nabla\left[\Psi\left(\mathbf{x}_s^{rec};\omega\right)\right]\right\}_{S\times J} \left\{C(\omega)\right\}_{J\times 1}. \tag{3.17}$$

Substituting equation (3.15) into equation (3.17) leads to the formulation that correlating particle velocities at *L* measurement points to other *S* reconstructed locations:

$$\left\{\hat{v}_n(\mathbf{x}_s^{rec};\omega)\right\}_{S\times 1} = \left\{\nabla\left[\Psi\left(\mathbf{x}_s^{rec};\omega\right)\right]\right\}_{S\times J} \left\{\nabla\left[\Psi\left(\mathbf{x}_l^{meas};\omega\right)\right]\right\}^{\dagger}_{J\times L} \left\{\hat{v}_n\left(\mathbf{x}_l^{meas};\omega\right)\right\}_{L\times 1}. \tag{3.18}$$

For simplicity, equation (3.18) can also be written as,

$$\left\{\hat{v}_n\left(\mathbf{x}_s^{rec};\omega\right)\right\}_{S\times 1} = \left[G_{\hat{v}_n\hat{v}_n}\left(\mathbf{x}_s^{rec} \mid \mathbf{x}_l^{meas};\omega\right)\right]_{S\times L} \left\{\hat{v}_n\left(\mathbf{x}_l^{meas};\omega\right)\right\}_{L\times 1}, \tag{3.19}$$

where $\left[G_{\hat{v}_n\hat{v}_n}\left(\mathbf{x}_s^{rec}\,|\,\mathbf{x}_l^{meas};\omega\right)\right]_{S\times L}$ is the transfer function, which is given by

$$\left[G_{\hat{v}_n\hat{v}_n}\left(\mathbf{x}_s^{rec}\,|\,\mathbf{x}_l^{meas};\omega\right)\right]_{S\times L}=\left\{\nabla\left[\Psi\left(\mathbf{x}_s^{rec};\omega\right)\right]\right\}_{S\times J}\left\{\nabla\left[\Psi\left(\mathbf{x}_l^{meas};\omega\right)\right]\right\}_{J\times L}^{\dagger}. \tag{3.20}$$

Having the solution formulations determined from measured data and source geometry shape, the only unknown parameter need to be determined is the number of expansion terms *J*. Theoretically, the number of expansion terms should be determined with respect to the highest structural wave number. However, errors and background noised contaminated in the measurement data cannot be avoided. And error analysis proved that the errors contaminated in the high order terms are more easily to be exaggerated unboundedly during the reconstruction process. Also, as discussed above, to ensure reconstruction accuracy, the number of expansion terms are set no larger than the number of measurement points. For obvious reasons, an excessive number of measurement locations are impractical which is especially true for relatively small structures. So, determine an optimized number of expansion terms is essential.

As the name suggests, one of the simplest regularization technique, least square method, is a built-in part of original HELS approach. The optimal number of expansion terms J_{op} is obtained by minimizing the least square errors between trail solutions and measured data in an iterative manner. To this end, the normal surface velocities at another S locations, designated as $\left\{\hat{v}_n\left(\mathbf{x}_s^{ver};\omega\right)\right\}_{S\times 1}$, are supplemented as verification data. Mathematically, the least square optimization process is expressed as

$$\min_J \sum_{i=1}^{S}\left\|\hat{v}_n\left(\mathbf{x}_{s,i}^{rec};\omega\right)-\hat{v}_n\left(\mathbf{x}_{s,i}^{ver};\omega\right)\right\|_2^2 \to J_{op}, \tag{3.21}$$

where $\hat{v}_n\left(\mathbf{x}_{s,i}^{rec};\omega\right)$ is the trail reconstructed particle velocity at the i^{th} velocity verification location $\vec{x}_{s,i}$ calculated by equation (3.19).

3.3.2 Solution of reconstructing acoustic pressure

Next, the sound waves radiated into the field are reconstructed based on normal surface velocity measurement. The interrelationship between radiated sound pressure and expansion functions are given in equation (3.2) and the expansion coefficients are calculated based on measured normal surface velocity in equation (3.15). So, predicting sound pressures at N field locations based on normal surface velocity measured at L locations can be easily achieved by substituting equation (3.15) into equation (3.2) and yield

$$\left\{\hat{p}\left(\mathbf{x}_n^{rec};\omega\right)\right\}_{N\times 1}=\left[G_{\hat{p}\hat{v}_n}\left(\mathbf{x}_n^{rec}\,|\,\mathbf{x}_l^{meas};\omega\right)\right]_{N\times L}\left\{\hat{v}_n\left(\mathbf{x}_l^{meas};\omega\right)\right\}_{L\times 1}, \tag{3.22}$$

where $\left[G_{\hat{p}\hat{v}_n}\left(\mathbf{x}_n^{rec}\,|\,\mathbf{x}_l^{meas};\omega\right)\right]_{N\times L}$ is the transfer function that reveals the interrelationships between structural vibration and resultant sound radiation, which is given by

$$\left[G_{\hat{p}\hat{v}_n}\left(\mathbf{x}_n^{rec}\,|\,\mathbf{x}_l^{meas};\omega\right)\right]_{N\times L}=i\omega\rho_0\left[\Psi\left(\mathbf{x}_n^{rec};\omega\right)\right]_{N\times J}\left\{\nabla\left[\Psi\left(\mathbf{x}_l^{meas};\omega\right)\right]\right\}^{\dagger}_{J\times L}. \tag{3.23}$$

As discussed above, to ensure reconstruction accuracy, the number of expansion terms J should be constrained smaller than the number of input normal surface velocities. The more points' normal surface velocities are inputted, the larger the maximal number of expansion terms J could be, and the more details in the reconstructed results could be included. Thus, the potential of reconstruction accuracy is increased. However, an excessive number of measurement points might not be practical especially for small size structures. In order to increase the accuracy of reconstruction, normal surface velocities at more other locations on the surface are regenerated first. The input points can thus be increased from L to M ($M >> L$). It should be pointed out that the reason for doing so is just to increase the upper limit of J and such a process will not increase the accuracy of input data. Since the regenerated surface velocities are just mathematical products.

Reconstruction of normal surface velocities at S locations based on L measurement normal surface velocities has already been given in equation (3.19). In order to obtain normal surface

velocities at M ($M = k \times S$) locations, the reconstruction of S locations needs to be repeated for k times regarding point set S_1, S_2, … S_k. Mathematically, it can be written as follows,

$$\left\{\hat{v}_n\left(\mathbf{x}_m^{rec};\omega\right)\right\}_{M\times 1} = \begin{Bmatrix} \left[G_{\hat{v}_n\hat{v}_n}\left(\mathbf{x}_{s_1}^{rec} \mid \mathbf{x}_l^{meas};\omega\right)\right]_{S\times L} \\ \left[G_{\hat{v}_n\hat{v}_n}\left(\mathbf{x}_{s_2}^{rec} \mid \mathbf{x}_l^{meas};\omega\right)\right]_{S\times L} \\ \vdots \\ \left[G_{\hat{v}_n\hat{v}_n}\left(\mathbf{x}_{s_k}^{rec} \mid \mathbf{x}_l^{meas};\omega\right)\right]_{S\times L} \end{Bmatrix}_{M\times L} \left\{\hat{v}_n\left(\mathbf{x}_l^{meas};\omega\right)\right\}_{L\times 1}. \tag{3.24}$$

Next, the reconstructed normal surface velocities are used as input to predict sound radiation and equation (3.10) is then be rewritten as

$$i\omega\rho_0\left\{\hat{v}_n\left(\mathbf{x}_m^{rec};\omega\right)\right\}_{M\times 1} = \left\{\nabla\left[\Psi\left(\mathbf{x}_m^{rec};\omega\right)\right]\right\}_{M\times J}\left\{C\left(\omega\right)\right\}_{J\times 1}. \tag{3.25}$$

Similar to determining the velocity reconstruction expansion coefficients with respect to L measurement points in equation (3.15), $\left\{C\left(\omega\right)\right\}_{J\times 1}$ can also be determined by taking a pseudo inversion of equation (3.25),

$$\left\{C\left(\omega\right)\right\}_{J\times 1} = i\omega\rho_0\left\{\nabla\left[\Psi\left(\mathbf{x}_m^{rec};\omega\right)\right]\right\}_{J\times M}^{\dagger}\left\{\hat{v}_n\left(\mathbf{x}_m^{rec};\omega\right)\right\}_{M\times 1}. \tag{3.26}$$

Substituting equation (3.26) into equation (3.2) yields the acoustic pressures at N reconstructed field locations

$$\left\{\hat{p}\left(\mathbf{x}_n^{rec};\omega\right)\right\}_{N\times 1} = i\omega\rho_0\left[\Psi\left(\mathbf{x}_n^{rec};\omega\right)\right]_{N\times J}\left\{\nabla\left[\Psi\left(\mathbf{x}_m^{rec};\omega\right)\right]\right\}_{J\times M}^{\dagger}\left\{\hat{v}_n\left(\mathbf{x}_m^{rec};\omega\right)\right\}_{M\times 1}, \tag{3.27}$$

For simplicity, equation (3.27) is also rewritten with respect to transfer function

$$\left\{\hat{p}\left(\mathbf{x}_n^{rec};\omega\right)\right\}_{N\times 1} = \left[G_{\hat{p}\hat{v}_n}\left(\mathbf{x}_n^{rec} \mid \mathbf{x}_m^{rec};\omega\right)\right]_{N\times M}\left\{\hat{v}_n\left(\mathbf{x}_m^{rec};\omega\right)\right\}_{M\times 1}, \tag{3.28}$$

where the transfer function $\left[G_{\hat{p}\hat{v}_n}\left(\mathbf{x}_n^{rec} \mid \mathbf{x}_m^{rec};\omega\right)\right]_{N\times M}$ is given by

$$\left[G_{\hat{p}\hat{v}_n}\left(\mathbf{x}_n^{rec}\mid\mathbf{x}_m^{rec};\omega\right)\right]_{N\times M}=i\omega\rho_0\left[\Psi\left(\mathbf{x}_n^{rec};\omega\right)\right]_{N\times J}\left\{\nabla\left[\Psi\left(\mathbf{x}_m^{rec};\omega\right)\right]\right\}^{\dagger}_{J\times M}. \tag{3.29}$$

Combine equation (3.24) with equation (3.28), the interrelationships between L measured normal surface velocities and sound pressures at N desired field locations can thus be derived as follows

$$\left\{\hat{p}\left(\mathbf{x}_n^{rec};\omega\right)\right\}_{N\times 1}=\left[H_{\hat{p}\hat{v}_n}\left(\mathbf{x}_n^{rec}\mid\mathbf{x}_l^{meas};\omega\right)\right]_{N\times L}\left\{\hat{v}_n\left(\mathbf{x}_l^{meas};\omega\right)\right\}_{L\times 1}, \tag{3.30}$$

where $\left[H_{\hat{p}\hat{v}_n}\left(\mathbf{x}_n^{rec}\mid\mathbf{x}_l^{meas};\omega\right)\right]_{N\times L}$ is the transfer function, which is given by

$$\begin{aligned}&\left[H_{\hat{p}\hat{v}_n}\left(\mathbf{x}_n^{rec}\mid\mathbf{x}_l^{meas};\omega\right)\right]_{N\times L}\\&=\left[G_{\hat{p}\hat{v}_n}\left(\mathbf{x}_n^{rec}\mid\mathbf{x}_m^{rec};\omega\right)\right]_{N\times M}\left\{\left[G_{\hat{v}_n\hat{v}_n}\left(\mathbf{x}_{s_1}^{rec}\mid\mathbf{x}_l^{meas};\omega\right)\right]_{S\times L},...,\left[G_{\hat{v}_n\hat{v}_n}\left(\mathbf{x}_{s_k}^{rec}\mid\mathbf{x}_l^{meas};\omega\right)\right]_{S\times L}\right\}_{M\times L}.\end{aligned} \tag{3.31}$$

Same as the reconstruction of normal surface velocity, given the geometry information of measured and reconstructed surface as well as measured normal surface velocities, the only unknown parameter will be the number of expansion terms J.

In original HELS approach, same optimal number of expansion terms is used to predict both particle velocity and sound pressure. Actually, the optimal number of expansion terms obtained through comparing with measured normal surface velocities has proved to be very effective for velocity to velocity prediction. However, the thus obtained J_{op} may not be the best for velocity to pressure prediction. This is because errors contaminated in the measurement will be heavily amplified in cross prediction. Such errors include amplitude and phase mismatch, the background noise, interference signals, etc. To circumvent such problem, in this dissertation, different optimal J (J_{opv} and J_{opp}) are determined respectively to do velocity to velocity prediction and velocity to pressure prediction.

In this section, only the simplest least square method is presented and more complex regularization techniques will be discussed in section 3.4. The optimal expansion terms J_{opp} is

obtained by minimizing the least square errors between trail reconstructed results and measured sound pressures in an iterative manner. To this end, acoustic pressures measured at N field locations, designated as $\hat{p}\left(\mathbf{x}_{n,i}^{ver};\omega\right)$, are supplemented as verification information. Mathematically, the optimization process is expressed as

$$\min_{J}\sum_{i=1}^{N}\left\|\hat{p}\left(\mathbf{x}_{n,i}^{rec};\omega\right)-\hat{p}\left(\mathbf{x}_{n,i}^{ver};\omega\right)\right\|_2^2\rightarrow J_{\text{opp}}, \tag{3.32}$$

where $\hat{p}\left(\mathbf{x}_{n,i}^{rec};\omega\right)$ is the trail reconstructed acoustic pressured at i^{th} pressure verification location $\vec{x}_{n,i}$ calculated by equation (3.30).

3.3.3 Solution of reconstructing time averaged acoustic intensity and sound power

Having the sound pressure and particle velocity in the fluid field be reconstructed, other acoustic quantities including time averaged acoustic intensity and sound power can be easily calculated.

The normal-component of time averaged sound intensity $\hat{I}_n$ of any field location at frequency ω can be calculated through the product of the complex conjugate of the normal component of particle velocity and the complex amplitude of sound pressure at that field location, see equation (3.33).

$$\hat{I}_n\left(\mathbf{x}^{rec};\omega\right)=\frac{1}{2}\text{Re}\left(\hat{p}\left(\mathbf{x}^{rec};\omega\right).\hat{v}_n^{*}\left(\mathbf{x}^{rec};\omega\right)\right) \tag{3.33}$$

The sound power radiated into far-field can be obtained by summation of contributions of sound power radiated from each the discretized surface element. Assume that the structural surface is divided into K discrete area elements ΔS_k, then the normal component of the time averaged normal intensity on the k^{th} element area $\left\{\hat{I}_n\left(\mathbf{x}^{rec};\omega\right)\right\}_{S(k)}$ can be calculated by using equation (3.33). The total acoustic power can thus be calculated by

$$P(\omega) = \sum_{k=1}^{K} \Delta S_k \left\{ \hat{I}_n \left(\mathbf{x}^{rec}; \omega \right) \right\}_{S(k)}. \tag{3.34}$$

3.4 Regularization

Theoretically, if all the vibration information on the surface can be measured without any error, then the predicted vibro-acoustic field obtained using the above formulations will be absolutely accurate as J approaches infinity.[53] However, this is impossible in practice. The transfer functions that were given in Eq. (20) and Eq. (29) have extremely large condition numbers that indicate the reconstruction problems are severely ill-posed. Accordingly, even small background noise and/or other interfering signals contaminated in the measurements may lead to unbounded prediction results. Strategies used to ensure bounded results and to attain meaningful reconstruction can be summarized in one word: regularization.[54] The ultimate goal of all regularization techniques is to smooth the dependence of the output results on the input data. There is no specific regularization strategy that provides best optimization results for all inverse problems since different inversion approaches yield different physical characteristics.

As discussed above, one of the simplest regularization techniques, least square approach, is a built-in part of original HELS method. The optimal number of expansion terms J_{op} is obtained by minimizing the least square errors between trail solutions and measured data in an iterative manner. To circumvent the difficulty that optimal number of expansion terms determined through velocity-to-velocity reconstruction is usually not best for velocity-to-pressure reconstruction, different optimal numbers of expansion terms are induced, designated as J_{opv} and J_{opp}. Their determination processes are given in subsection 3.3.1 and subsection 3.3.2.

Although the simple least square approach ensures a bounded result, it cannot guarantee meaningful reconstruction. This is because that by excluding all expansion terms higher than J_{opv} and J_{opp} completely, not only the terms that severely affected by contaminated errors are truncated,

other high order terms that are essential for details reconstruction are also ignored. Due to low signal to noise ratio of input data or not properly chosen test parameters, what usually happens in practice is that the optimal number of expansion terms determined through simple least square method could be extremely small even target source is a complex structure under random excitations. Thus, the resultant reconstruction turn out to be superposition of first few low order expansion terms, saying monopole, dipole and quadrupole etc., which are obviously not what we expected.

To circumvent this problem, before determining optimal number of expansion terms, the measured normal component of surface velocity should be regularized first by applying a filter or other weighting techniques to restrain the embedded perturbation. [55] Currently, various regularization techniques have been applied to NAH including standard Tikhonov (TR) method,[56] modified Tikhonov (MTR) method, Landweber iteration,[57] and the conjugate gradient approach[58] etc.

Generally speaking, all these regularization techniques aim at eliminating the effects of noise embedded in the detail evanescent waves by applying low pass filter in wavenumber domain. Different regularization techniques imply different shape of the low pass filter. Except for the shape of these filters, the break point of the filter also needs to be determined by other techniques. Such a break point is demonstrated by an undetermined parameter. The parameter selection techniques can be divided into two categories by whether the knowledge of noise information is needed. One of the most popular parameter selection technique that requires an estimate of the noise variance is the discrepancy principle of Morozov. Representatives of methods that do not require prior knowledge of noise variance include ordinary cross validation (OCV) and generalized cross validation (GCV).

Previous studies have indicated that the MTR with its regularization parameter determined from GCV provides the best regularization results for HELS algorithm. Mathematically, this hybrid regularization scheme is expressible as

$$\min_{J}\sum_{i=1}^{S}\left\|\hat{v}_n\left(\mathbf{x}_{s,i}^{rec,\beta};\omega\right)-\hat{v}_n\left(\mathbf{x}_{s,i}^{ver};\omega\right)\right\|_2^2\rightarrow J_{\text{opv,MTR}}, \tag{3.35}$$

$$\min_{J}\sum_{i=1}^{N}\left\|\hat{p}\left(\mathbf{x}_{n,i}^{rec,\gamma};\omega\right)-\hat{p}\left(\mathbf{x}_{n,i}^{ver};\omega\right)\right\|_2^2\rightarrow J_{\text{opp,MTR}}, \tag{3.36}$$

where the trail reconstructed acoustic quantities $\hat{v}_n\left(\mathbf{x}_{s,i}^{rec,\beta};\omega\right)$ and $\hat{p}\left(\mathbf{x}_{n,i}^{rec,\gamma};\omega\right)$ with regularization parameter β and γ are calculated as follows

$$\left\{\hat{v}_n\left(\mathbf{x}_{s}^{rec,\beta};\omega\right)\right\}_{S\times 1}=[V_{\hat{v}_n\hat{v}_n}]_{S\times S}[F_{\hat{v}_n\hat{v}_n}^{\beta}]_{S\times S}[\Sigma_{\hat{v}_n\hat{v}_n}]_{S\times L}^{-1}[U_{\hat{v}_n\hat{v}_n}]_{L\times L}^{H}\left\{\hat{v}_n\left(\mathbf{x}_{l}^{meas};\omega\right)\right\}_{L\times 1}, \tag{3.37}$$

$$\left\{\hat{p}\left(\mathbf{x}_{n}^{rec,\gamma};\omega\right)\right\}_{N\times 1}=[V_{\hat{p}\hat{v}_n}]_{N\times N}[F_{\hat{p}\hat{v}_n}^{\gamma}]_{N\times N}[\Sigma_{\hat{p}\hat{v}_n}]_{N\times L}^{-1}[U_{\hat{p}\hat{v}_n}]_{L\times L}^{H}\left\{\hat{v}_n\left(\mathbf{x}_{l}^{meas};\omega\right)\right\}_{L\times 1}, \tag{3.38}$$

where $[V_{\hat{v}_n\hat{v}_n}]$ and $[U_{\hat{v}_n\hat{v}_n}]$ in equation (3.37) are the right and left unitary matrices, respectively, of the matrix $\left[G_{\hat{v}_n\hat{v}_n}\left(\mathbf{x}_{s_1}^{rec}\,|\,\mathbf{x}_{l}^{meas};\omega\right)\right]_{S\times L}$ in equation (3.20), $[\Sigma_{\hat{v}_n\hat{v}_n}]$ is the diagonal matrix that contains singular values of the corresponding matrix; whereas $[V_{\hat{p}\hat{v}_n}]$ and $[U_{\hat{p}\hat{v}_n}]$ in equation (3.38) are the right and left orthonormal matrices, respectively, and $[\Sigma_{\hat{p}\hat{v}_n}]$ is the diagonal matrix containing singular values of velocity-to-pressure transfer function $\left[H_{\hat{p}\hat{v}_n}\left(\mathbf{x}_{n}^{rec}\,|\,\mathbf{x}_{l}^{meas};\omega\right)\right]_{N\times L}$ in equation (3.31). $[F_{\hat{v}_n\hat{v}_n}^{\beta}]$ and $[F_{\hat{p}\hat{v}_n}^{\gamma}]$ are the low-pass filter containing the singular values ε_i in matrix $[\Sigma_{\hat{v}_n\hat{v}_n}]$ and η_i in matrix $[\Sigma_{\hat{p}\hat{v}_n}]$, which are defined as,

$$[F_{\hat{v}_n\hat{v}_n}^{\beta}]_{S\times S}=diag\left(\cdots,\frac{\varepsilon_i^2(\beta+\varepsilon_i^2)^2}{\beta^3+\varepsilon_i^2(\beta+\varepsilon_i^2)^2},\cdots\right), \tag{3.39}$$

$$[F^{\gamma}_{\hat{p}\hat{v}_n}]_{N\times N} = diag\left(\cdots, \frac{\eta_i^2(\gamma+\eta_i^2)^2}{\gamma^3+\eta_i^2(\gamma+\eta_i^2)^2}, \cdots\right), \tag{3.40}$$

where regularization parameters β and γ are determined by GCV through a minimization process given by,

$$\min_{\beta}\left(\frac{\left\|\left[F^{\beta}_{\hat{v}_n\hat{v}_n,h}\right]_{L\times L}\left[U_{\hat{v}_n\hat{v}_n}\right]^H_{L\times L}\left\{\hat{v}_n\left(\mathbf{x}_l^{meas};\omega\right)\right\}_{L\times 1}\right\|_2^2}{\left(\text{Trace}\left[F^{\beta}_{\hat{v}_n\hat{v}_n,h}\right]_{L\times L}\right)^2}\right), \tag{3.41}$$

$$\min_{\gamma}\left(\frac{\left\|\left[F^{\gamma}_{\hat{p}\hat{v}_n,h}\right]_{L\times L}\left[U_{\hat{p}\hat{v}_n}\right]^H_{L\times L}\left\{\hat{v}_n\left(\mathbf{x}_l^{meas};\omega\right)\right\}_{L\times 1}\right\|_2^2}{\left(\text{Trace}\left[F^{\gamma}_{\hat{p}\hat{v}_n,h}\right]_{L\times L}\right)^2}\right), \tag{3.42}$$

where $\left[F^{\beta}_{\hat{v}_n\hat{v}_n,h}\right]$ and $\left[F^{\gamma}_{\hat{p}\hat{v}_n,h}\right]$ are the high-pass filters determined by subtracting the low-pass filters $\left[F^{\beta}_{\hat{v}_n\hat{v}_n}\right]$ and $\left[F^{\gamma}_{\hat{p}\hat{v}_n}\right]$ from the unitary matrix,

$$\left[F^{\beta}_{\hat{v}_n\hat{v}_n,h}\right]_{L\times L} = diag\left[\left(\left[\mathrm{I}\right]_{S\times S} - [F^{\beta}_{\hat{v}_n\hat{v}_n}]_{S\times S}\right), \left[\mathrm{I}\right]_{(L-S)\times(L-S)}\right], \tag{3.43}$$

$$\left[F^{\gamma}_{\hat{p}\hat{v}_n,h}\right]_{L\times L} = diag\left[\left(\left[\mathrm{I}\right]_{N\times N} - [F^{\gamma}_{\hat{p}\hat{v}_n}]_{N\times N}\right), \left[\mathrm{I}\right]_{(L-N)\times(L-N)}\right]. \tag{3.44}$$

Instead of directly using trail reconstruction results to match measured verification data, the hybrid regularization approach applies filtered results to determine the optimized number of expansion terms. For each value of the number of expansion terms, the transfer function is filtered by MTR first while the regularization parameter is obtained by using GCV. Then the regularized reconstructions are compared with verification data to identify an optimal number of expansion terms.

By combining these two regularization methods together, the robustness of the proposed approach could significantly increase. As discussed previously, the error and background noise

contaminated in high order terms are more likely to be amplified unboundedly during the reconstruction process. Original least square approach truncates all terms higher than certain order to ensure bounded results, which often lead to many useful desired detail information be omitted. Whereas the hybrid approach utilized a low pass filter to constrain effect of noise disturbance, by doing so, many high order expansion terms could be included. In other words, with the help of MTR and GCV, the number of expansion terms could go much higher and thus increase reconstruction accuracy for detail evanescent waves.

3.5 Procedures for modified HELS approach

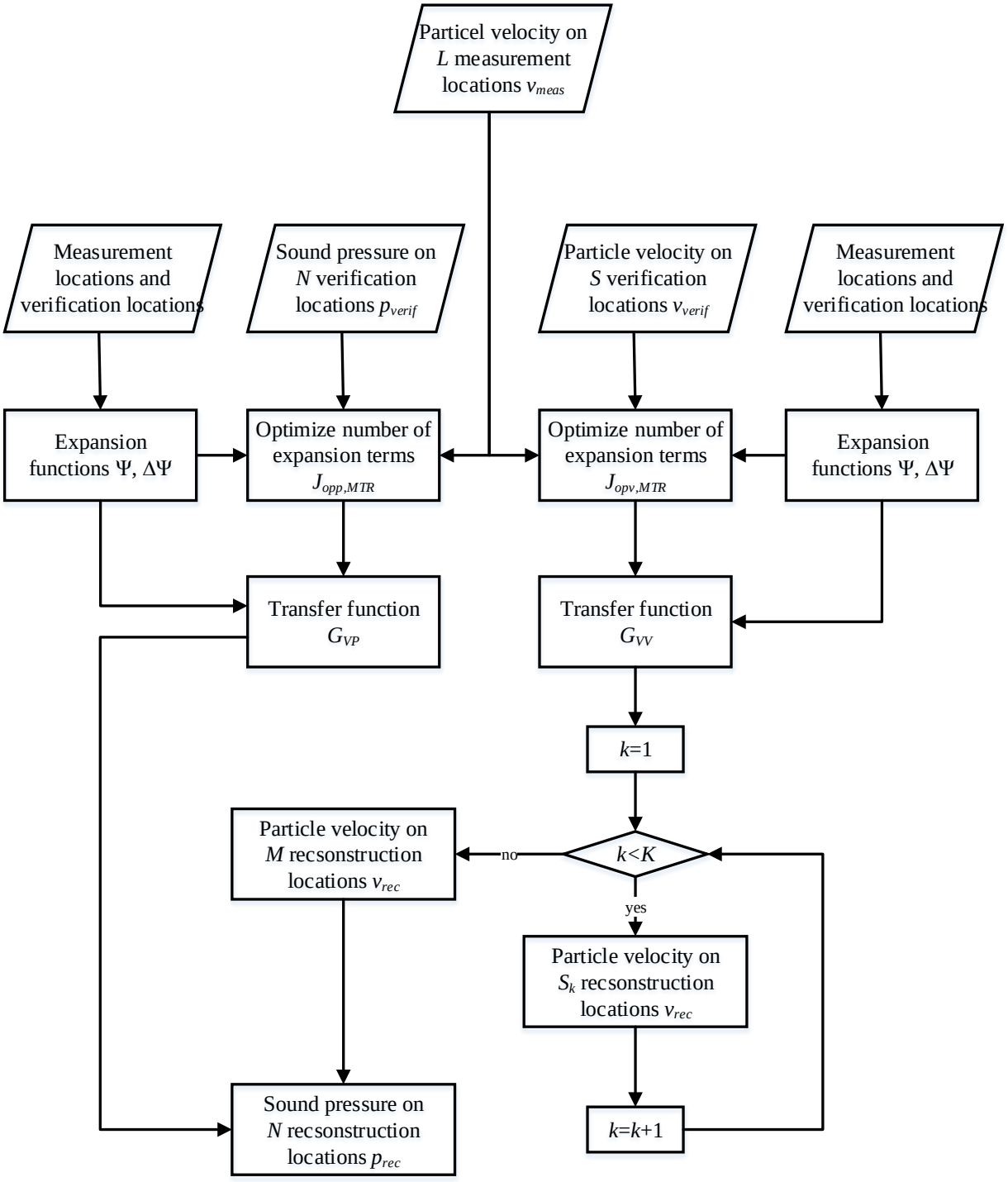

Figure. 3.2 Flowchart of modified HELS algorithm

Having the formulas and regularization techniques for the normal surface velocity based NAH, the detailed implementing procedures are given in this section. Flowchart of the process is described in figure (3.2). To illustrate the procedures, we also assume that normal surface velocities at L number of surface locations are measured as input and sound pressures at N number of field locations are desired.

1. Measure normal surface velocities at L number of input surface locations $\left\{\hat{v}_n\left(\mathbf{x}_l^{meas};\omega\right)\right\}_{L\times 1}$ and S number of supplemented surface locations $\left\{\hat{v}_n\left(\mathbf{x}_s^{ver};\omega\right)\right\}_{S\times 1}$. Measure acoustic pressures at N number of supplemented locations $\left\{\hat{p}\left(\mathbf{x}_n^{ver};\omega\right)\right\}_{N\times 1}$ in the field near desired prediction area. Also, collect coordinates of all the measurement and verification locations;
2. Take $\left\{\hat{v}_n\left(\mathbf{x}_l^{meas};\omega\right)\right\}_{L\times 1}$ as the input to establish the HELS formulations Eq. (3.19) to reconstruct normal surface velocities on S supplemented surface locations $\left\{\hat{v}_n\left(\mathbf{x}_s^{rec,\beta};\omega\right)\right\}_{S\times 1}$. Then comparing with $\left\{\hat{v}_n\left(\mathbf{x}_s^{ver};\omega\right)\right\}_{S\times 1}$ and applying an iteration scheme to determine the optimal expansion term $J_{\text{opv,MTR}}$ and corresponding regularization parameter β;
3. Use $\left\{\hat{v}_n\left(\mathbf{x}_l^{meas};\omega\right)\right\}_{L\times 1}$ as the input to reconstruct normal surface velocities at other S locations with obtained regularization parameters $J_{\text{opv,MTR}}$ and β. Then the reconstruction is repeated k times regarding point set S_1, S_2, … S_k. Finally, normal surface velocities at M ($M = k \times S$) locations $\left\{\hat{v}_n\left(\mathbf{x}_m^{rec};\omega\right)\right\}_{M\times 1}$ are regenerated which are used as input to predict sound radiated from the vibrating surface;

4. Take $\left\{\hat{v}_n\left(\mathbf{x}_m^{rec};\omega\right)\right\}_{M\times 1}$ as the input to establish the HELS formulations to reconstruct acoustic pressures on N supplemented surface locations $\left\{\hat{p}\left(\mathbf{x}_n^{rec,\gamma};\omega\right)\right\}_{N\times 1}$. Then comparing with $\left\{\hat{p}\left(\mathbf{x}_n^{ver};\omega\right)\right\}_{N\times 1}$ and applying an iteration scheme to determine the optimal expansion term $J_{\text{opp,MTR}}$ and corresponding regularization parameter γ.
5. Use $\left\{\hat{v}_n\left(\mathbf{x}_m^{rec};\omega\right)\right\}_{M\times 1}$ as the input to predict the acoustic pressures at as many points as necessary with obtained regularization parameters $J_{\text{opp,MTR}}$ and γ.

3.6 Conclusion

Theory and implementation procedures of the modified HELS approach are illustrated in detail in this chapter. By substituting the sound pressure measured by conformal microphone array with normal surface velocity measured by laser vibrometer as inputs, the data acquisition process has been greatly simplified, while the advantages of HELS method are also retained. Through the application of hybrid regularization strategy, boundedness and meaningful reconstruction results are always desirable.

With the input data changing from sound pressure to particle velocity, optimization process for many test parameters are also changed. The guidelines for implementing the modified HELS based NAH will be discussed in next chapter along with numerical simulation examples.

CHAPTER 4: NUMERICAL VALIDATION OF MODIFIED HELS METHOD BASED NAH WITH NORMAL SURFACE VELOCITY AS INPUT

The forth illustrated formulas and procedures of the modified HELS method based NAH are validated numerically in this chapter. Implementation of the traditional sound pressured inputs based HELS and the proposed normal surface velocity approach share the same guidelines for most of the parameters. However, since individual optimal numbers of expansion terms are used for velocity-to-velocity and velocity-to-pressure reconstruction respectively, the determined optimal number of expansion terms are different from traditional HELS method. Also, since superposition of spherical waves is used to approximate arbitrary shape structures, the origin locations must be chosen carefully per special relationships between measurement surface and reconstruction surface. Such optimal processes will be demonstrated in detail with respect to different simulation scenarios.

4.1 Introduction

The simulation is conducted with respect to a simply-supported, unbaffled thin plate. The reason for selecting this test object is that the vibro-acoustic response of a simply-supported plate is readily available analytically. The measured surface particle velocities in normal direction are simulated by mode summation approach. Once the normal surface velocity distribution is obtained, the benchmark sound pressures in the field that are used to test reconstruction accuracy are calculated by Rayleigh integral.

On the other hand, the simply-supported plate represents a series of geometries that hardly be completely approximated by the superposition of spherical expansion functions which is fundamental to HELS approach. So, the capability of reconstructing the whole vibro-acoustic filed that radiated from this highly non-spherical geometry is a strong proof that the proposed modified HELS approach is suitable for any arbitrary shape structure.

To make the task more challenging, except for simulating vibration of normal modes, vibration pattern with asymmetric velocity distribution at different frequencies are also examined. The impacts of reconstruction parameter include the number of expansion functions, the location of origin and reconstruction distance are also studied in detail. Based on this thorough investigation, implementation guidelines for the normal surface velocity based NAH approach are provided.

4.2 Test apparatus

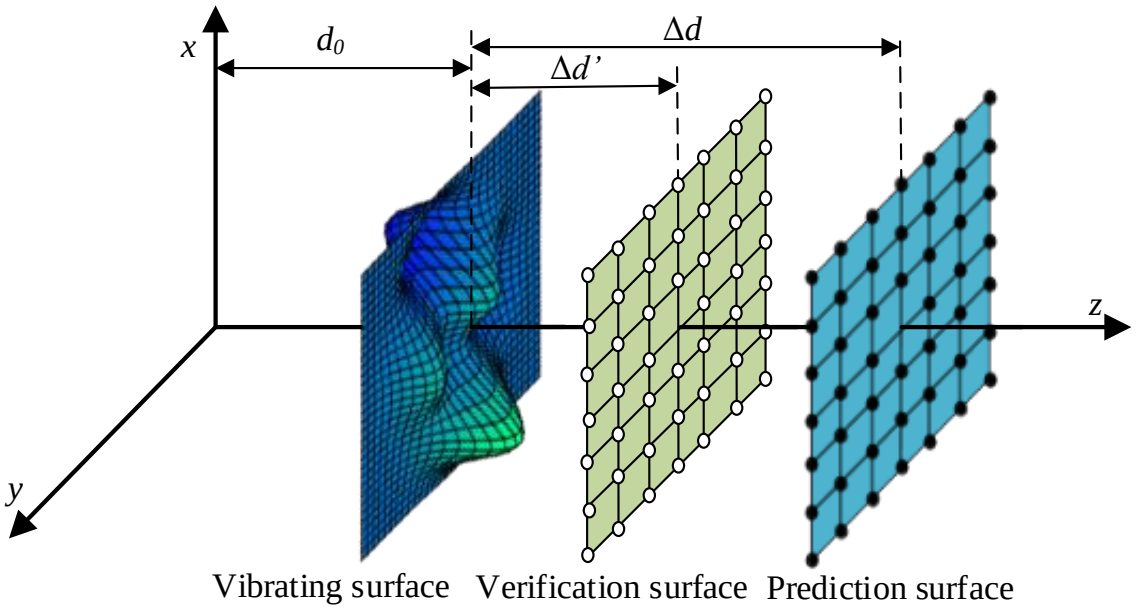

Figure. 4.1 Schematic of the test setup

Figure 4.1 shows the test setup of this numerical simulation in a Cartesian coordinate system. The origin of Cartesian coordinates is placed at a distance d_0 from the vibrating surface on the opposite side of the surface where the vibro-acoustic field is to be predicted. The simulated test object is a steel plate with dimension 0.5×0.5 m^2, and 5 mm thick. The first 9 natural frequencies and associated structural wavenumbers are summarized in Table 3.1.[59]

TABLE 4.1. Natural mode, natural frequency, and structural wavenumber of simulated plate

Natural mode	Natural frequency	Structural wavenumber	
		k_x (m^{-1})	k_y (m^{-1})
(1, 1)	98.1	6.28	6.28
(1, 2)	245.3	6.28	12.56
(2, 2)	392.4	12.56	12.56
(1, 3)	490.5	6.28	18.84
(2, 3)	637.7	12.56	18.84
(3, 3)	883	18.84	18.84
(2, 4)	981	12.56	25.12
(3, 4)	1226.3	18.84	25.12

In this simulation, the number of directly measured normal surface velocity locations is L=64 and normal surface velocities at other S=64 points are used as supplemented verification information to optimize regularization parameters $J_{opv,MTR}$ and β. With these parameters, the velocity-to-velocity reconstruction is repeated k =4 times to regenerate normal surface velocity distribution with $M=k \times S$=256 points. The new generated normal surface velocities are used as input to predict radiated acoustic pressures at N= 64 field locations at prediction surface which is located at a distance Δd from source surface. A virtual supplemented verification microphone array of the same dimension 0.5 × 0.5 m^2 also with N= 64 microphones on sound pressure verification surface is placed at a distance $\Delta d'$ from vibrating surface along positive z-axis. In order to better evaluation of the reconstruction results, except for the discussion about impacts of reconstruction distance to reconstruction accuracy, all other simulations are carried out with sound pressure verification and prediction points located on the same plane. In other words, unless otherwise specified, we have $\Delta d = \Delta d'$.

The simulation includes two parts: vibration-acoustic field caused by vibration at certain resonant frequencies and normal surface velocity field simulated by summation of several different modes. The summation of different modes will generate an asymmetrical vibration deflection

shape, which is much more challenging than simple symmetrical standard normal mode shape. Note that this is just a simulation and such a vibration pattern which only includes a sum of finite number of modes is hard to achieve in practice. It is because that except for the unlikely event of the structural vibration in which motion is excited coinciding exactly with one of the natural modes, all the modes with different weighting coefficients will be excited.

In order to make the simulation more realistic, for all the measured quantities including $\left\{\hat{v}_n\left(\mathbf{x}_l^{meas};\omega\right)\right\}_{L\times 1}$, $\left\{\hat{v}_n\left(\mathbf{x}_s^{ver};\omega\right)\right\}_{S\times 1}$ and $\left\{\hat{p}\left(\mathbf{x}_n^{ver};\omega\right)\right\}_{N\times 1}$, wide-band random white noise has been added to simulate a 20dB signal to noise ratio.

To evaluate both the normal surface velocity and acoustic pressure reconstruction accuracy in an objective manner, normalized L2-norm errors with respect to benchmark data are used as an indicator. Consider acoustic quantities at R locations are reconstructed, the normalized L2-norm errors ξ is defined as:

$$\xi = \frac{\sum_{i=1}^{R}\left\|Q\left(\mathbf{x}_{r,i}^{rec};\omega\right)-Q\left(\mathbf{x}_{r,i}^{bench};\omega\right)\right\|_2^2}{\sum_{i=1}^{R}\left\|Q\left(\mathbf{x}_{r,i}^{bench};\omega\right)\right\|_2^2}\times 100\%, \tag{4.1}$$

where $Q\left(\mathbf{x}_{r,i}^{rec};\omega\right)$ represents reconstructed acoustic quantities at the i^{th} location and $Q\left(\mathbf{x}_{r,i}^{bench};\omega\right)$ represents corresponding benchmark data at the same location.

4.3 Reconstruction results

The analytic solutions of vibration responses of a thin simply-supported plate are given by[60]

$$\begin{aligned} w(x,y,z_0) &= \sum_{\mu}\sum_{\nu} A_{\mu\nu}\sin\frac{\mu\pi(x+L_x/2)}{L_x}\sin\frac{\nu\pi(y+L_y/2)}{L_y}, \\ -\frac{L_x}{2}\le x\le\frac{L_x}{2}, &\qquad -\frac{L_y}{2}\le y\le\frac{L_y}{2}, \end{aligned} \tag{4.2}$$

where $w(x, y, z_0)$ is the complex amplitudes of the flexural vibration displacement of the plate. μ and ν are the index that represents order of certain normal mode along the *x* and *y* direction. $A_{\mu\nu}$ is the amplitude coefficient corresponding to (μ, ν) mode which is obtained from the initial conditions and boundary conditions. L_x and L_y are the width and length of the test object respectively and z_0 is the position of the plate along the *z* axis.

Having the vibration displacement, the corresponding normal surface velocity of the plate $v_n(x, y, z_0)$ can be calculated as

$$v_n(x, y, z_0) = -i\omega w(x, y, z_0), \tag{4.3}$$

where ω is the targeted angular frequency. Given the normal surface velocity on source surface, the sound pressures at any field location (*x'*, *y'*, z') can be calculated through Rayleigh integral as follows

$$p(x', y', z') = \frac{-i\omega\rho_0}{2\pi}\int_{-L_x/2}^{L_x/2}\int_{-L_y/2}^{L_y/2} v_n(x, y, z_0)\frac{e^{ikR}}{R}dxdy, \tag{4.4}$$

where *k* is the acoustic wavenumber corresponding to angular frequency ω and ρ_0 is the ambient density of the fluid medium. R is the distance between desired field location (*x'*, *y'*, z') and surface location (x, y, z_0) and calculated as

$$R = \sqrt{(x'-x)^2 + (y'-y)^2 + (z'-z_0)^2}, \tag{4.5}$$

Having the geometry information of vibrating surface as well as desired sound pressure prediction locations, vibration displacement and normal surface velocity distribution on the surface at specific resonant frequency can be easily calculated through equation 4.2-4.3 by setting μ and ν the corresponding normal mode index. Then, the radiated sound at desired field point can be calculated using equation 4.4. In this simulation example, vibroacoustic field generated at first eight modes are reconstructed.

As introduced before, to make the task more challenging, except for simulating vibration of normal modes, vibration pattern with asymmetric velocity distribution at different frequencies are also investigated. Such a case is simulated by summation of (2, 2) mode and (2, 3) mode with equal amplitude coefficients. Mathematically, substitute size of simulated surface which is 0.5 × 0.5 m^2 and mode index into equation (4.2), this vibration deflection shape is calculated as

$$\begin{aligned} w(x, y, z_0) = A_{22} \sin\frac{2\pi(x+0.5/2)}{0.5}\sin\frac{2\pi(y+0.5/2)}{0.5} \\ + A_{23}\sin\frac{2\pi(x+0.5/2)}{0.5}\sin\frac{3\pi(y+0.5/2)}{0.5}, \\ -\frac{L_x}{2} \le x \le \frac{L_x}{2}, \qquad -\frac{L_y}{2} \le y \le \frac{L_y}{2}, \end{aligned} \tag{4.6}$$

Once again, no matter at which frequency, the vibration pattern with contribution only from 2 normal modes is hard to achieve. In reality, except for the very unlikely event that the structure is excited at one of the resonant frequencies, the deflection shape must be formed with contributions from an infinite number of natural modes. The reason for doing so is just for generating a complex asymmetric velocity distribution. Rayleigh's integral can handle any shape of normal surface velocity distribution at any frequency. So, such a simulation is totally practicable. In this subsection, such a velocity distribution is simulated at 1350 Hz. In next subsection, when we discuss the impact of reconstruction frequency, reconstruction results at two other frequencies will be examined.

The measurement locations and verification locations on the source surface that used in this section are shown in figure 4.2. The L=64 number of directly measured normal surface velocity points are indicated by red round dots and the equally distributed M=256 number of reconstruction points are indicated by green dots. It can be seen that in this case, the measurement surface area is approximately the same as source surface area. The scenario that area covered by measurement points is smaller than vibrating surface will be discussed in next section. Sound pressure

verification and reconstructed surface are simulated 0.2m away from vibrating surface, saying $\Delta d = \Delta d' = 0.2$m. The verification microphones are also equally distributed on the 0.5×0.5 m^2 verification plane.

In this section, the optimized origin distance d_0 is optimized as 0.21m. The detailed determination process of all these parameters will be discussed in next section.

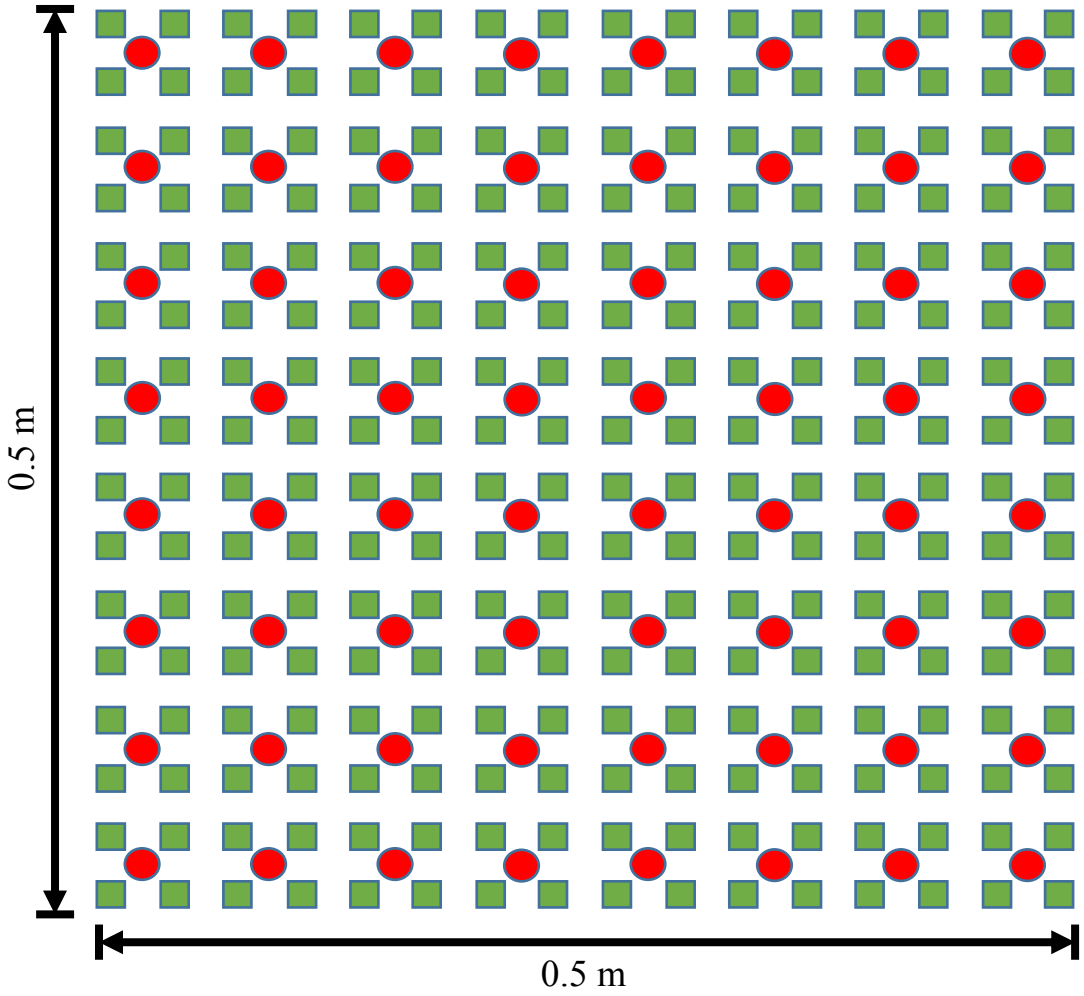

Figure. 4.2 Sketch of 64 measurement locations (red round dots ●) and 256 reconstructed locations (green square dots ■)on the vibrating surface

At resonant frequencies, the comparisons between benchmark data and reconstruction results for velocity-to-velocity and velocity-to-pressure reconstruction are shown in figure 4.3 and figure 4.4 respectively.

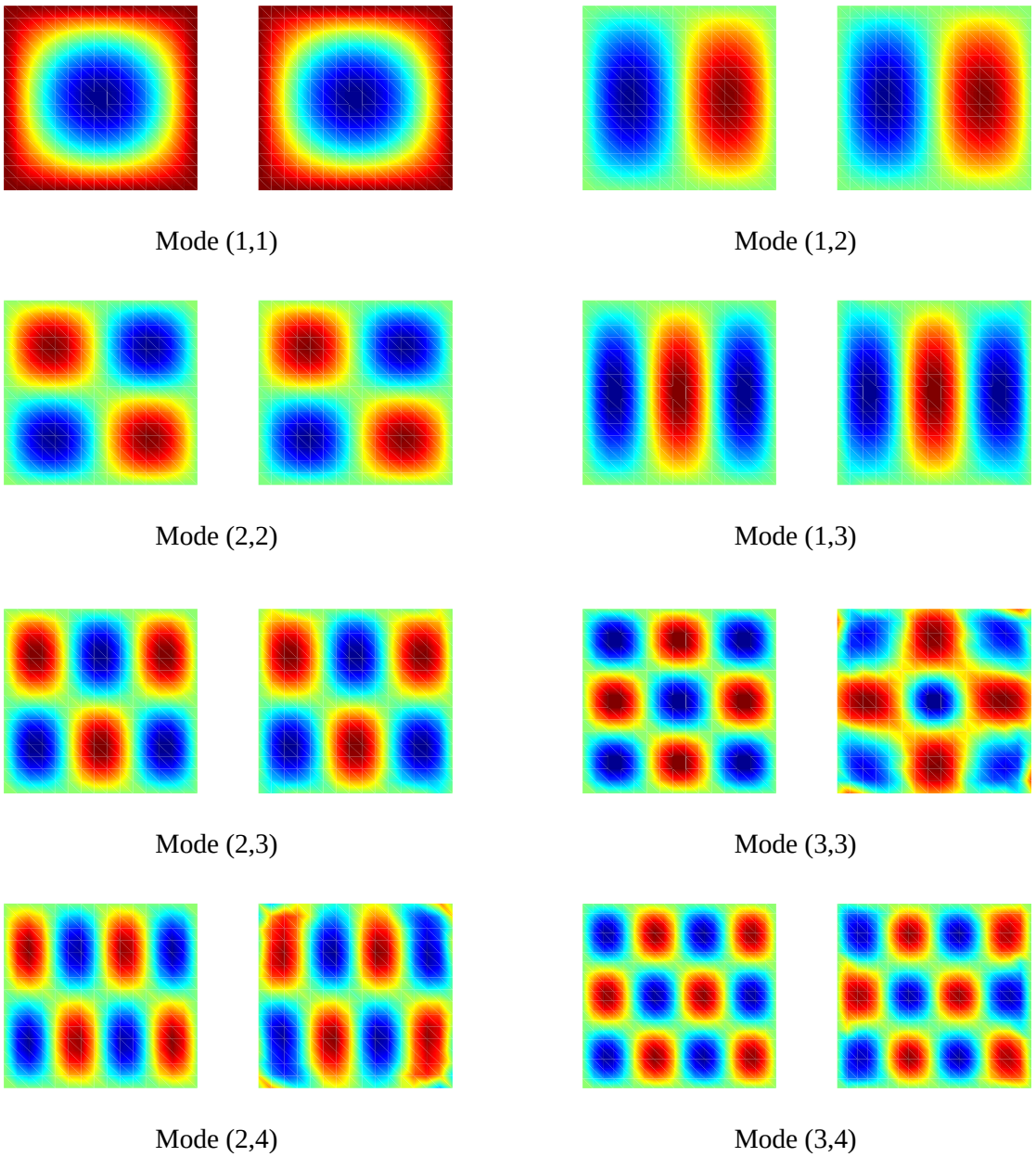

Figure. 4.3 Comparison of normal surface velocities on source surface between benchmark data (*left*) and reconstructed results (*right*) for eight natural modes

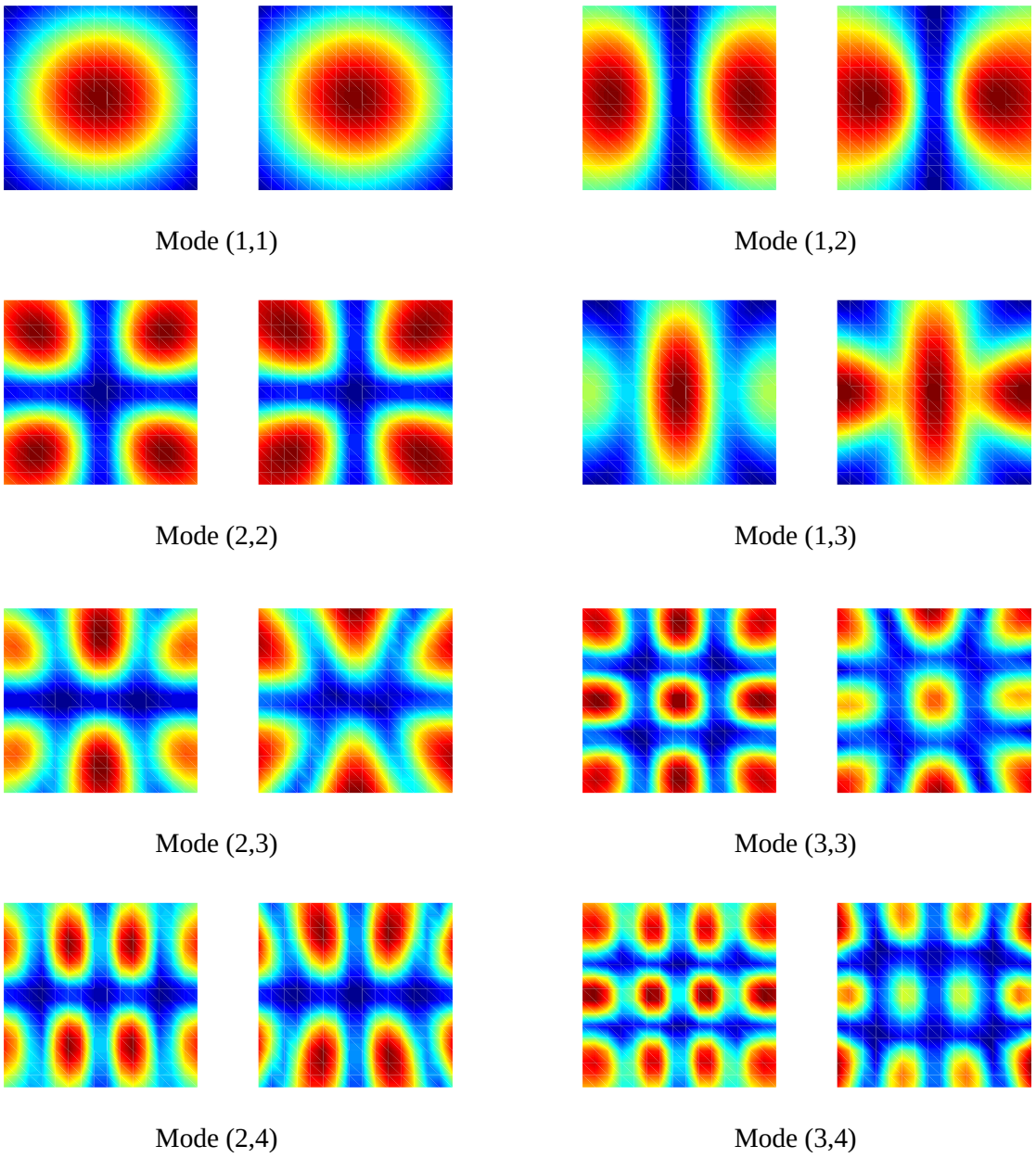

Figure. 4.4 Comparison of sound pressure distribution on prediction plane (Δd = 0.2m) between benchmark data (*left*) and reconstructed results (*right*) for eight natural modes

Generally speaking, the reconstructed normal surface velocities and sound pressures agree well with theatrical data in all these 8 modes, especially for the surface central area and for the lower frequency modes.

For velocity-to-velocity reconstruction, the errors mostly occur near the boundary areas of the plate. What's more, for higher modes, obvious distortion around the boundary can be found. It

is because that spherical expansion functions are used to approximate the velocity distribution on a plane surface and the distance between boundary areas and hypothetical spherical surface are larger than the central areas. This problem is more severe for high order expansion terms which are essential for reconstructing higher modes. This explains why the distortions are more obvious for higher frequency modes.

The velocity-to-pressure reconstructions also provide acceptable results. However, the results are not as good as velocity-to-velocity reconstruction. The theoretical sound radiations are obtained from Rayleigh's integral that utilizes all the surface vibrating information. The inputs of our simulation are just a finite number of velocities at discrete locations which are incomplete. To do sound pressure reconstruction from these incomplete data, our approach is to use superposition of a finite number of spherical expansion functions to approximate sound radiation. Such an approach will make errors embedded in measurement data be exaggerated heavily in the velocity-to-pressure cross reconstruction. To eliminate this side effect, more high order terms which are necessary for accurately reconstructing details are truncated. Therefore, sound pressure reconstructions are a little worse than velocity reconstruction.

Figure 4.5 & 4.6 depict reconstruction results for simulation of summation of (2, 2) mode and (2, 3) mode at 1350 Hz. Similar to simulations at resonant frequencies, the normal component of surface velocities yield a quite high reconstruction accuracy on the whole surface. The sound pressure prediction also shows satisfactory results except for some locations near edge areas. This is also because that the boundary areas are too far from the hypothetical sphere. In this simulation case, spherical expansion functions are used to approximate the vibro-acoustic field generated by a plane surface with asymmetric velocity distribution, thus many high-order terms are needed. However, to account for the distortion in the boundary areas and errors embedded in measurement data, high order terms and small scale information are removed through regularization process.

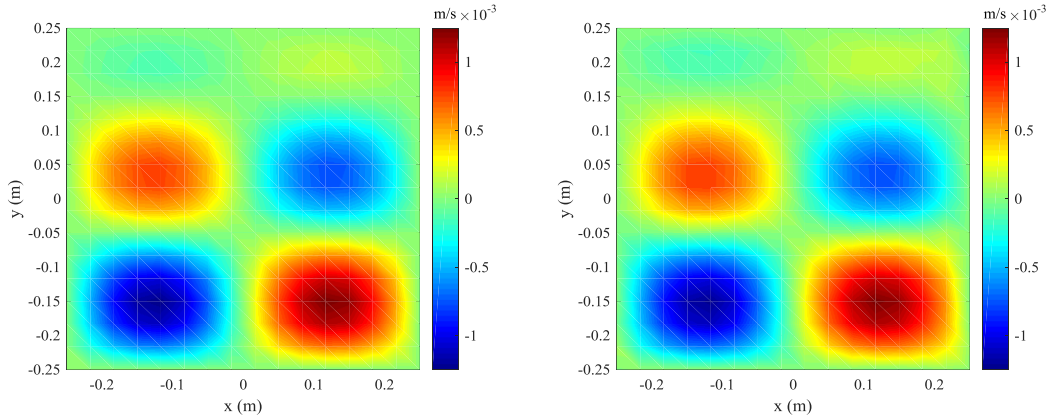

Figure. 4.5 Comparison of normal surface velocities on source surface between benchmark data (left) and reconstructed results (right) for summation of (2, 2) mode and (2, 3) mode

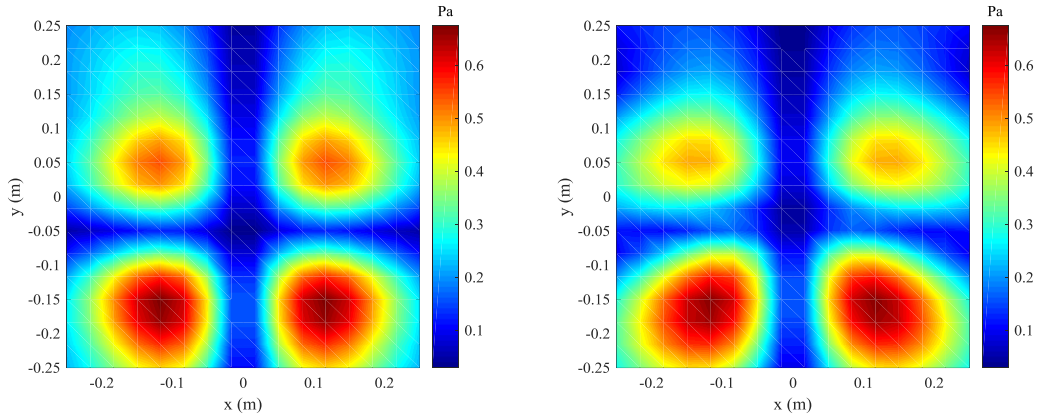

Figure. 4.6 Comparison of sound pressure distribution on prediction plane between benchmark data (left) and reconstructed results (right) summation of (2, 2) mode and (2, 3) mode at 1350 Hz

4.4 Effects of different parameters on reconstruction accuracy

In this section, the effects of various reconstruction parameters will be addressed. Through these error analysis, recommended parameter determination strategies will be given. Guidelines for parameter determination for original HELS based method have been discussed a lot in previous publications.[61,62] For many parameters, the new proposed normal surface velocity based modified HELS approach shares same determination guidelines with original HELS method. However, there are also many parameters optimization processes need to be changed and there are some more new induced variables. Such parameters include measurement locations, regularization parameters, the

location of the origin, prediction distance, relationship between acoustic frequencies and structural wavenumber etc. In this section, we will focus on these parameters.

To evaluate the reconstruction accuracy in an objective manner, when analyzing the impact of certain parameters, only targeted parameter will change while the other variables being held constant. And the reconstruction errors are calculated by equation 4.1.

4.4.1 Optimal number of expansion terms

As illustrated in section 3.4, unlike original HELS based NAH, $J_{\mathrm{opv,MTR}}$ and $J_{\mathrm{opp,MTR}}$ are induced to do velocity-to-velocity and velocity-to-pressure reconstruction respectively. Here, we need to study the regularization process first. Take the simulation of summation of (2, 2) mode and (2, 3) mode at 1350 Hz as an example.

The reconstruction accuracies under a different number of expansion terms for normal surface velocity reconstruction on the vibrating surface and sound radiation on the prediction holography surface are depicted in figure 4.7 and figure 4.8 respectively.

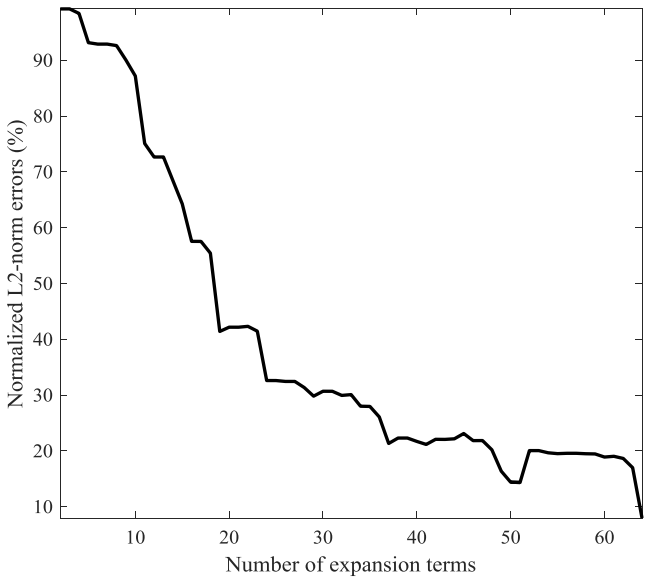

Figure. 4.7 The normalized L2-norm errors curve with respect to different number of expansion terms for reconstruction of normal surface velocity at supplemented verification locations

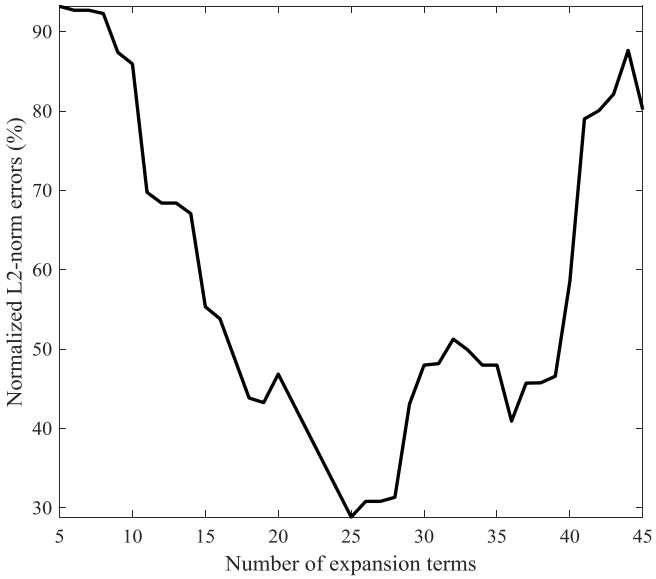

Figure. 4.8 The normalized L2-norm errors curve with respect to different number of expansion terms for reconstruction of sound pressure at supplemented verification locations

From figure 4.7, it can be seen clearly that with the increase of the number of expansion terms, the trend of L2-norm errors curve for velocity reconstruction behave a monotonic decrease. In other words, the more expansion functions are included, the more accuracy the reconstruction could be. This can be easily explained as follows. Many small-scale details are contained in the velocity distribution, which can only be reconstructed through high-order terms. With more expansion functions are utilized, more details will be included in the reconstruction results, thus will improve reconstruction quality. When the number of expansion terms reaches 64, the accuracy of velocity reconstruction is very high (L2-norm error under 10%). For this velocity-to-velocity reconstruction, the measurement locations and reconstruction locations are of course located on the same surface, thus the inevitable errors contaminated in the input data will be not amplified unboundedly in the high order expansion terms reconstruction process.

However, velocity-to-pressure reconstruction with a propagating distance behaves differently with respect to a different number of expansion terms. The L2-norm errors decrease to a certain point than increases thereafter that form a U-shape curve. The decrease or increase of the

curve is all due to the evanescent waves. The more expansion terms are used, the more evanescent waves could be depicted, thus reconstruction error will naturally decrease. However, the errors contaminated in evanescent waves will also be exponentially exaggerated with the increase of propagating distance[63], which might totally distort reconstruction results. So to ensure prediction accuracy, extra high order terms are truncated. On the other hand, these evanescent waves' contributions are relatively small in the prediction plane, so discarding high-order terms will not stop us from getting acceptable prediction results.

4.4.2 Measurement locations

In HELS based NAH, the vibroacoustic field is estimated by matching trial reconstructed results with verification data. We know that any function defined on the holography surface can be uniquely and completely approximated by certain spherical expansion terms. There is a prerequisite that error free velocity measurement needs to be taken at every surface locations which is certainly impossible in practice. However, based on a finite number of discrete measurements and considering about embed errors, the proposed modified HELS approach also yields satisfactory results. In this section, we will discuss the discrete data acquisition strategy. The measurement locations are controlled by two factors: measurement interval distance and measurement covered area.

To ensure reconstruction accuracy of target source, the minimum measurement interval needs to be larger than ¼ λ_s, where λ_s is the shortest structural wavelength of interest. Such recommendation is the same with original HELS and has been examined in many previous publications, so we will not talk about this in detail here.

Except for measurement interval, to finally determine all the measurement locations, covered measurement area also need to be identified. In many cases, when analyzing large size structure such as vehicle panel, it may not that easy to take measurements at locations that all over

the surface. If the whole vibroacoustic field can be reconstructed precisely based on normal surface velocity measured from just a small part of the structure, the overall cost of the data acquisition process will decrease dramatically. To find out this problem, the relationships between ratio of measurement area to vibrating surface area ς and prediction errors ξ are investigated.

The numerical simulation is conducted regarding first eight modes that same with section 4.3. To do so, the ratio of measurement area to vibrating surface area's impact could be revealed comprehensively. The number of measurement points is fixed at 64 and the measurement locations are equally distributed. Note that when changing the measurement area, the measurement interval will also be changed. When ς equals 1, the measurement interval is the largest which is 7 cm. The shortest wavelength of interest λs is 25cm. The largest measurement interval is larger than ¼ λs, which is 25/4=6.25 cm in this case. So, the measurement interval fulfills the requirement. To help readers better understanding how the ratio ς is changed, figure 4.9 listed 4 examples of measurement setups with different ς.

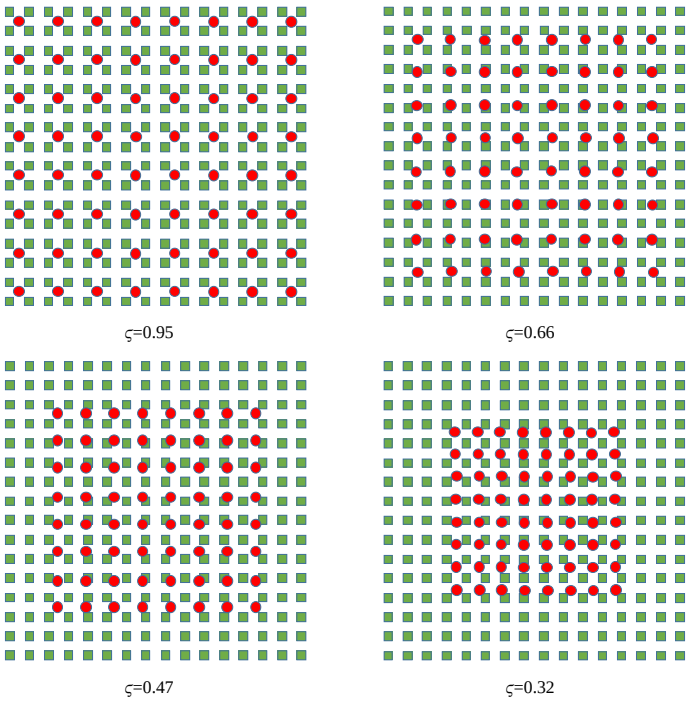

Figure. 4.9 Sketch of measurement locations (red round dots ●) and reconstructed locations (green square dots ■)on the vibrating surface with 4 different ratios of measurement area to vibrating surface area ς.

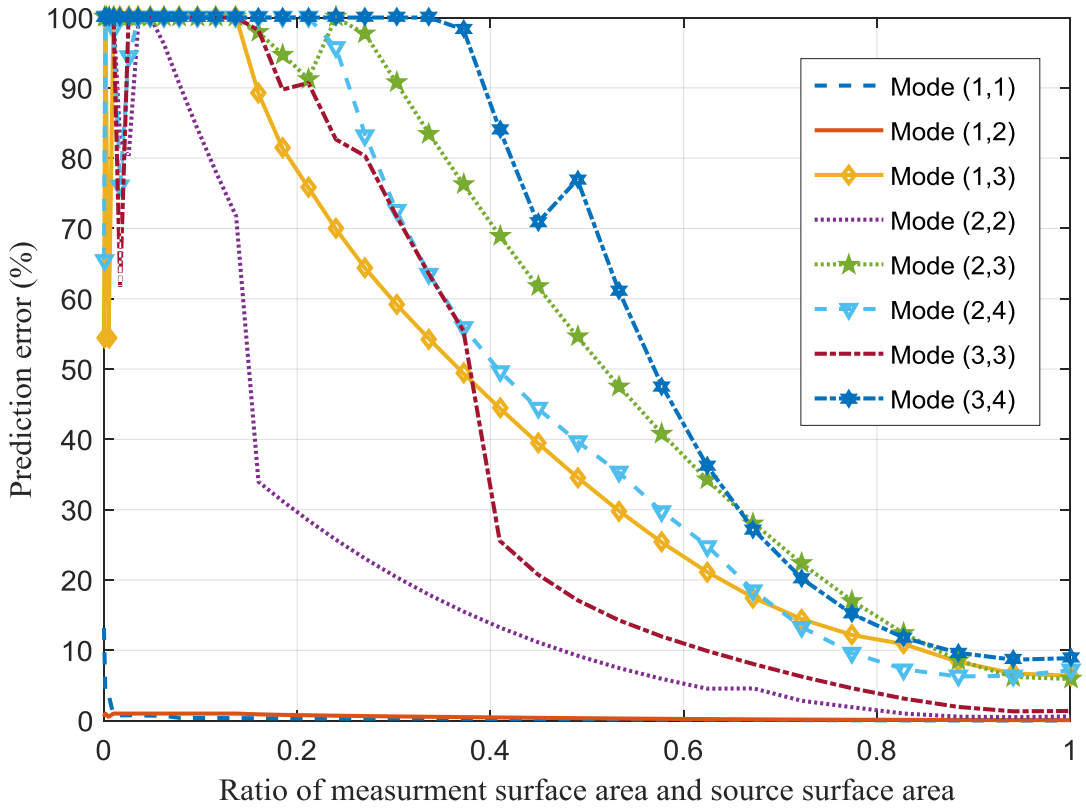

Figure. 4.10 The normalized L2-norm errors curve with respect to different ratio of measurement area to vibrating surface area at 8 natural modes.

The interrelationships between ratio ς and reconstruction accuracy are shown in figure 4.10. On the whole, with the increase of ς, the reconstruction errors decrease for all 8 scenarios. That means that the larger area the measurement locations covered, the higher the reconstruction accuracy could achieve. The results are expected since the regularization process minimizes prediction errors at measurement locations whereas the prediction errors at the not covered portion of the surface are not guaranteed.

For mode (1, 1) and mode (1, 2) the prediction errors remain relatively small even with smallest ς. That is because there are not many details in these two modes, data collected from a small portion of the surface are capable of reflecting overall velocity distribution. However, for those higher modes which contain much more small scale details, information captured from a

small portion of the surface is not enough. Take a closer look at those higher-order modes, you can find that the curves for mode (2, 2) and mode (3, 3) decrease faster. More specifically, for mode (2, 2) and mode (3, 3), the prediction errors decrease to below 10% at ς equals 0.45 and 0.6 respectively whereas for other modes the prediction errors don't decrease to 10% until ς larger than 0.8. The reason is that mode (2, 2) and mode (3, 3) are not only vertically and horizontally symmetry, they also have mirror symmetry along diagonal lines. Whereas, the other modes are only symmetry along vertical and horizontal lines.

Therefore, to obtain better reconstruction results, the area covered by measurement locations should be as large as possible. However, in many real application scenarios, we cannot make measurements covering the whole vibrating surface for various reasons, such as obstacle parts around target object cannot be removed. For such cases, the measurement area could be reduced, however, the ratio of measurement area to vibrating surface area is recommended no less than 0.5.

4.4.3 Location of the origin

In the proposed velocity based HELS, recommended distance between the origin and vibrating surface is different from traditional sound pressure measurement based HELS.

Since spherical holography surfaces are used to approximate arbitrary shape structures in HELS theory, the reconstruction quality is heavily affected by the location of the origin. If the origin distance compares with source surface size is too small, the reconstruction errors might be very large, as this will result in many reconstruction locations away from geometry center going beyond the region of effectiveness. Conversely, if the origin distance is too large, the large radius might make high order expansion terms that responsible for detail information cannot be properly defined on the hypothetical spherical surface, also resulting in reconstruction inconsistencies.

Therefore, the origin location must be carefully selected. However, there are no analytical formulas for determination of this optimal distance.

Many numerical simulations have been conducted regarding original HELS based NAH[64], indicating that the optimal position d_0 falls within ± 10% of the characteristic dimension of source surface D,

$$d_0 = (0.9 \sim 1.1)D, \tag{4.7}$$

where $D = \sqrt{L^2 + W^2}$, L and W are the length and width of source surface respectively. In original HELS based NAH, to capture as many nearfield effects as possible, the standoff distance between measurement microphones and source surface is always set extremely small. The distance between origin and source surface and the distance between origin and measurement surface are approximately the same. Thus, the above optimal position is appropriate for both measurement and source surface.

In the proposed velocity based HELS, the above critical distance is good for velocity-to-velocity reconstruction and nearfield sound pressure prediction, for the same reason that the distances between measurement surface and reconstruction surface are relatively small. However, it is no longer suitable for far-field sound pressure prediction. Note that the origin is placed on the opposite side of the source surface and the actual distance between origin and prediction surface is $d_0 + \Delta d$, see figure 4.1. When determining optimal d_0 for sound pressure prediction, both measurement surface and prediction surface need to be taken into consideration.

Numerical simulations are carried out regarding summation of (2, 2) mode and (2, 3) mode at 1350 Hz to examine the effects of varying origin location to normal surface velocity and sound pressure reconstruction accuracy respectively. In this simulation, d_0 varies from 0 to 1.5D, while the prediction distance Δd is fixed at 0.2m which is about 0.6D. The results are shown in figure 4.11.

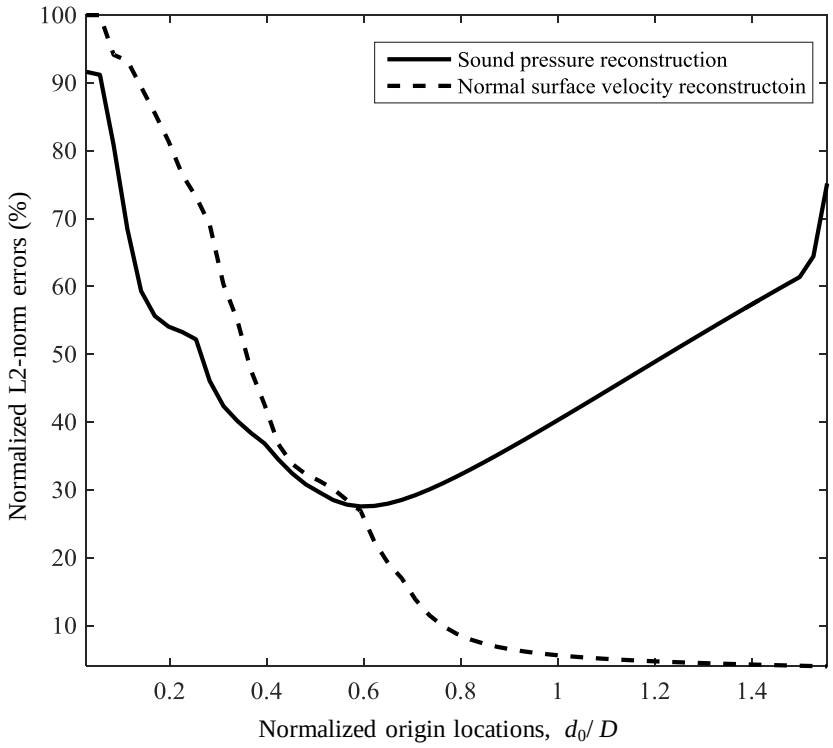

Figure. 4.11 The normalized L2-norm errors curves with respect to different origin locations.

A local minimum that corresponds to optimal origin location for sound pressure prediction can be found at $d_0/\ D \approx 0.6$, whereas the optimal origin location for normal surface velocity reconstruction locates at $d_0/\ D > 1$. Which coincident with above analysis that the optimal position d_0 appropriated for source surface may not necessarily best for far-field prediction surface.

There is always a trade-off between the accurately reconstruction of far-field sound pressure and normal surface velocity. A possible solution to this dilemma is to utilize different optimal origin locations for pressure reconstruction on prediction plane and particle velocity on source surface. However, such a way will complicate the reconstruction process and increase computational load. Actually, as seen in Figure 4.11, when optimal distance for sound pressure prediction plane ($d_0 \approx 0.6D$) is used, the reconstruction of surface velocity also yields acceptable results with normalized L2-norm error $\xi < 30\%$. When computation complexity is a concern over

accuracy reconstruction of surface vibration information, optimal distance for pressure prediction is recommended.

Unfortunately, for far-field sound pressure prediction, since prediction distance Δd also affects optimal origin locations, there is no 'one size fits all' guidelines for different prediction distance. To weigh the effect of source surface and prediction surface, the most direct and simplest thinking is to optimize d_0 with respect to a virtual surface located just in the middle of source surface and prediction surface by using guidelines for original HELS. More specifically, d_0 and Δd should fulfill a linear correlation and $d_0 + \Delta d/2$ should fall within $\pm$ 10% of D. Mathematically, the hypothesis relationship could be expressed as

$$d_0 = (0.9 \sim 1.1)D - \Delta d / 2, \tag{4.8}$$

In the example given in figure 4.11, the identified optimal d_0 is $0.6D$ and the prediction distance is $\Delta d = 0.2\text{m} \approx 0.6D$, which matches equation 4.8. Is this just an accidental coincidence? What if we place prediction surface closer or further to source surface? To address this problem, a series of numerical simulations are carried out at various prediction distances regarding different origin locations.

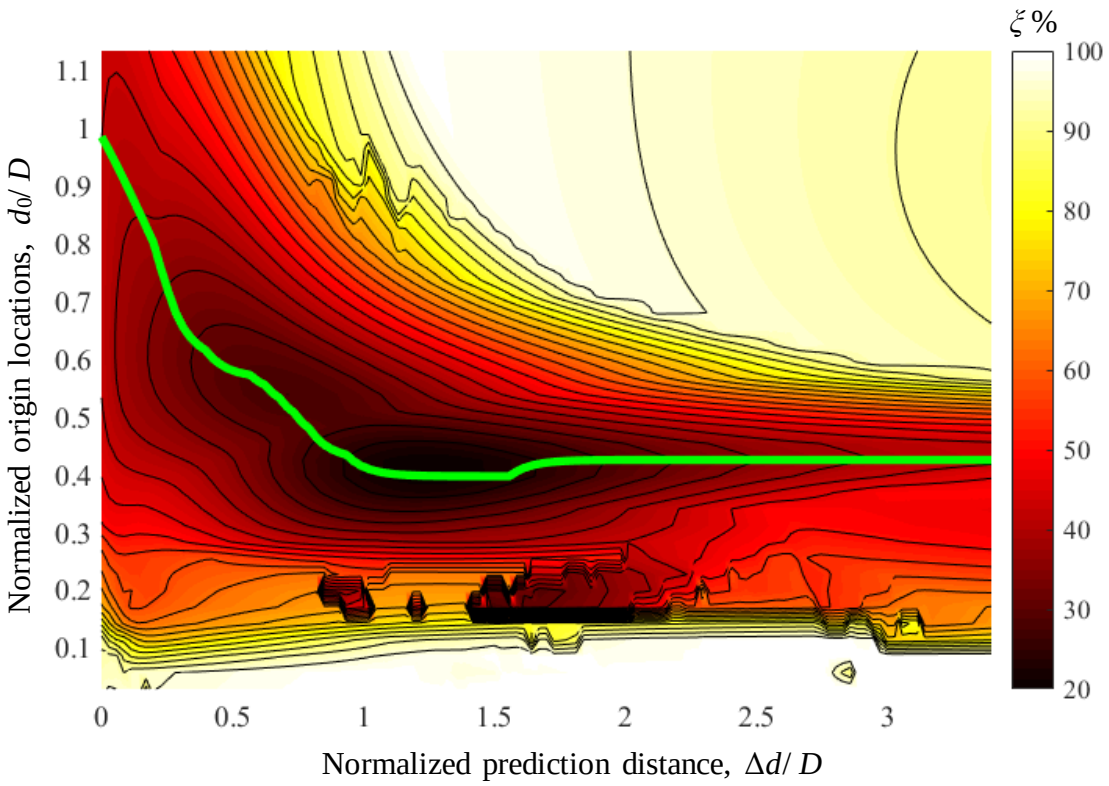

Figure. 4.12 Normalized L2-norm errors corresponding to various origin locations for different prediction distances.

The iteration results are shown in figure 4.12. The virtually prediction distance Δd varies from 0 to 3.4D. At each prediction distance, origin distance is changed from 0 to 1.2D. The reconstruction performances are still evaluated by normalized L2-norm errors and indicated by the hot map. The thus optimized d_0 for each prediction distance is indicated by a solid green line. To view this green curve as a whole, a negative correlation could be concluded between prediction distance and optimal origin distance. However, such negative correlation is non-linear. In the region of Δd= (0~1) D, the optimal origin distances decrease in a roughly linear manner and match the conjecture given in equation 4.8. However, when Δd is larger than D, the optimal d_0 is constrained within 0.4D and 0.5D. This is expected since origin cannot be placed too close to the source surface and it, of course, cannot exceed vibrating surface (d_0 >0). With prediction distance

increasing, the concomitantly decreased optimal d_0 must stop somewhere on the opposite side of source surface. So, the recommended optimal distance is numerically identified as

$$d_0 = \begin{cases} (0.9 \sim 1.1)D - \Delta d/2 & \Delta d < D \\ (0.4 \sim 0.5)D & \Delta d \geq D \end{cases}, \text{ or } d_0 = \begin{cases} D - \Delta d/2 & \Delta d < D \\ 0.45D & \Delta d \geq D \end{cases}. \quad (4.9)$$

4.4.4 Reconstruction at different prediction distance

In the above simulations, the sound pressure prediction points and verification points are in the same plane. In this subsection, while still utilizing optimized parameters identified from supplement verification microphones, the sound pressure prediction accuracies at locations away from verification surface will be examined. The simulations are still conducted with respect to summation of (2, 2) mode and (2, 3) mode at 1350 Hz. The supplemented microphones are placed 0.2m away from vibrating surface ($\Delta d'$=0.2m) and the prediction distance Δd is varied from 0.01m to 0.6m. The normalized L2-norm errors curve for each simulated case is in figure 4.13.

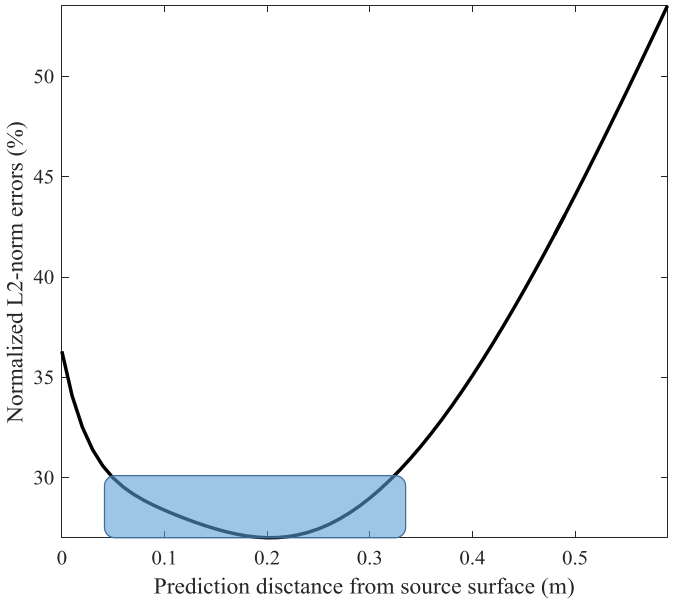

Figure 4.13 The normalized L2-norm errors curve for reconstruction of sound pressure with respect to different prediction distances

At Δd=0.2m, the minimum prediction error is achieved. This is reasonable since the utilized regularization parameters are optimized with respect to supplement microphones that are located

just at a plane 0.2m away from source surface. As indicated by shadows, when Δd changes from 0.05m to 0.33m, the prediction yields satisfactory results with ξ <30%. However, for even larger prediction distance, the prediction error increases gradually and finally tend to infinity. From these simulations, we can conclude that the variables optimized from supplement microphones are not only effective at verification surface but also valid at a 'small' region around these verification locations. If further locations need to be reconstructed, regularization process needs to be reconducted at locations near targeted places.

4.4.5 Reconstruction at different frequencies

The reconstruction accuracy of NAH is highly related to how much near-field effects (evanescent waves) could be captured. Whether a sound wave radiated from a vibrating structure is evanescent depends on the interrelationships between its acoustic wavenumber and structural wavenumber. So, in this subsection, these interrelationships in *k*-space are analyzed and their effects on reconstruction results are studied. Unlike the simulation given in section 4.3, the simulations are conducted with respect to the summation of (2, 2) mode and (2, 3) mode at two other frequencies (1050 Hz and 500 Hz). The simulation results are shown in figure 4.14 & 4.15.

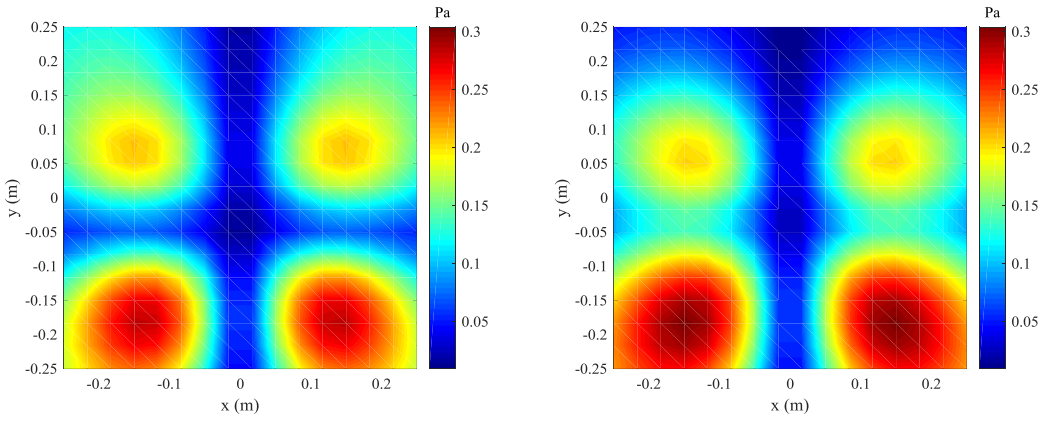

Figure 4.14 Comparison of sound pressure distribution on prediction plane (Δd = 0.2m) between benchmark data (left) and reconstructed results (right) at 1050 Hz

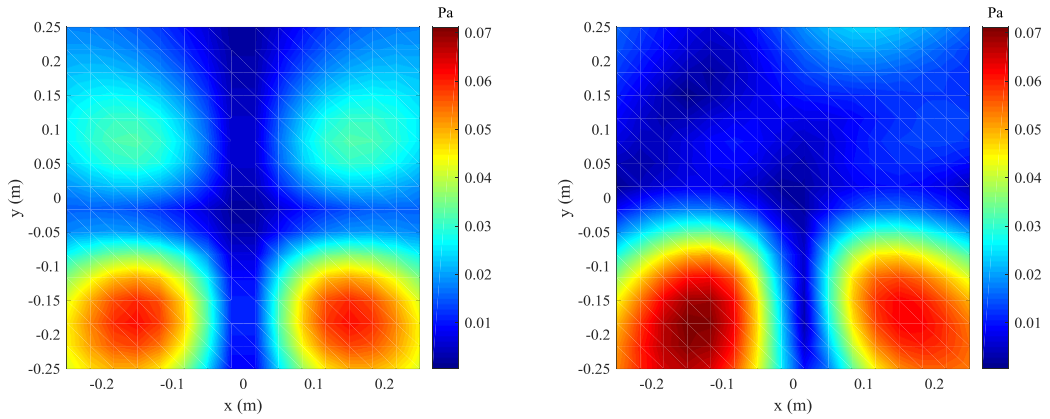

Figure 4.15 Comparison of sound pressure distribution on prediction plane ($\Delta d = 0.2m$) between benchmark data (left) and reconstructed results (right) at 500 Hz

The predictions at these two frequencies are not as good as 1350 Hz does (see figure 4.6). The reconstructed sound pressures don't obtain good agreements with benchmark data. This is mainly caused by incompleteness of necessary nearfield information.

Unlike traditional NAH which using sound pressures measured at a distance as an input, in this proposed approach, particle velocities obtained just on source surface are used as input. One may think that, theoretically, we captured all the nearfield effects. However, this might only be true when vibration information at every surface location is obtained, which is impossible in practice. In the data acquisition process, no matter how many points are measured, the obtained particle velocity distribution is always discrete. Thus, the missing information essential for evanescent waves cannot be reconstructed anyway. In order to restore detailed information, measurements at an excessive number of locations need to be taken. However, the increasing of sampling points will decrease transfer function's robustness to interference errors. This explains why the prediction accuracies of such evanescent waves will not be that satisfactory. The interrelationships between simulated acoustic wavenumber and spatial wavenumber in *k*-space are shown in figure 4.16.

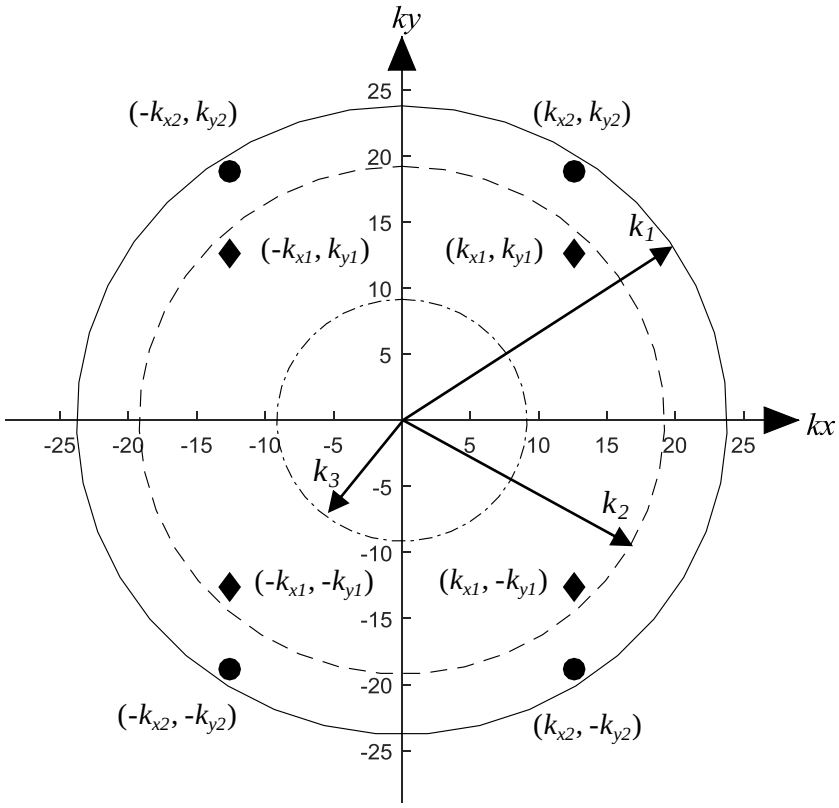

Figure 4.16 The relationships between acoustic wavenumbers and structural wavenumbers. The structural wavenumbers of simulated (2, 2) mode and (2, 3) mode are indicated by '♦' and '●' respectively. the radiation circles for three simulated frequencies 1350 Hz, 1050 Hz and 500 Hz are indicated by '——', '---' and '-•-' respectively.

The spatial wavenumbers of simulated (2, 2) mode and (2, 3) mode are designated as (k_{x1}, k_{y1}) and (k_{x2}, k_{y2}) respectively. The acoustic wavenumber at simulated frequencies 1350 Hz, 1050 Hz and 500 Hz are designated as k_1, k_2, and k_3. At 1350 Hz, we have $k_1 > \sqrt{k_{x1}^2 + k_{y1}^2}$ and $k_1 > \sqrt{k_{x2}^2 + k_{y2}^2}$, so the corresponding wavenumbers of the radiated sound wave are real which means that neither (2, 2) mode nor (2, 3) mode will generate evanescent waves. Similarly, at 1050 Hz, propagating sound wave will be generated by the structural wave of (2, 2) mode whereas no radiated sound wave will be produced by the structural wave of (2, 3) mode. However, at 500 Hz,

both these two simulated structural waves will not radiate sound into the far field. This explains why sound radiated from (2, 2) mode at 500 Hz and sound radiated from (2, 3) mode at 500 Hz and 1050 Hz are not reconstructed very well.

4.5 Conclusion

In this chapter, the reconstruction accuracies of modified HELS based NAH are verified under different conditions for a highly non-spherical surface. Compare to traditional HELS based NAH, by changing the input data from nearfield sound pressures to normal surface velocities, many parameters optimization processes have been changed. Through numerical simulation, the new parameter recommendation guidelines are determined. Although in these simulations, wide-band random white noise has been added to measurement signals, they are still not the real test. To validate the effectiveness in real life, series of real experiment validations are conducted in an anechoic chamber. Such results are demonstrated in chapter 6.

CHAPTER 5: FORCED VIBRO-ACOUSTIC COMPONENT (F-VAC)

In this chapter, through vibro-acoustic analysis based on modified HELS approach, a new concept of F-VAC will be given. F-VAC reveals the critical vibration component that is directly responsible for noise radiation. Such information could further provide engineers guidelines about how to control structural borne noise in the most cost-effective manner.

5.1 Introduction

The conventional thinking that suppressing vibration at a certain frequency will eliminate the sound radiated at that frequency has already been proved wrong by many peer-reviews academic papers for a long time. However, we cannot deny the fact that structure-borne noise is produced by structural vibration and structural borne noise control can be accomplished through vibration control. In other words, structural borne noise control must by conducted with respect to critical vibration components that directly related to sound radiation. To achieve such a goal, the first and foremost task is to find the interrelationships between vibration and resultant sound radiation.

One of the widely-used technique of find such relationship is FRF-reciprocity based vibro-acoustic analysis. However, the transfer functions obtained based on FRF- reciprocity principle are only valid at selected measurement locations and cannot expand to other non-examined places. So, it's a perfect technique for air-borne noise control, in which the vibrating structures can be treated as a finite number of point sources. As for structural-borne sound, the vibration behavior of the source structure need to be considered as a whole, So, an excessive number of measurement points are needed, which is obviously not practical.

The concept of radiation efficiency could reveal interrelationships between vibration and sound radiation in terms of normal modes. The different mode will perform different ability to radiate sound into far-field. Such an ability is evaluated by the ratio of radiated sound power to

spatially averaged square velocity, known as radiation efficiency. The normal modes based radiation efficiency analysis can provide each mode's contribution to sound radiation at a certain frequency. However, such results cannot tell engineers how to control structural borne sound in the most cost-effective manner. Since structural borne sound can only be effectively reduced by suppressing many high radiation efficiency modes together. By suppressing all those modes simultaneously, it is always cost too much. If you only control vibration of first dominant mode, it usually cannot provide satisfactory results. The optimal solution which locates somewhere in between cannot be revealed by modal analysis, for the simple reason that normal vibration modes are not directly related to sound radiation. As a set of orthogonal basis, normal modes are perfect tools for vibration analysis. However, they have nothing to do with sound radiation.

To better analysis sound radiation from vibrating structure, it is necessary to find another set of orthogonal basis that obtained directly from interrelationship between sound and vibration and further identify their relative contribution to sound radiation. In previous chapters, through modified HELS based NAH, interrelationships between structural vibration and acoustic radiation have already been established. These interrelationships can lead directly to transfer matrices between forced vibration and sound radiation. Singular value decomposition (SVD) of these transfer matrices will give out the desired orthogonal basis system which we name them F-VAC. Having the mutually orthogonal basis, the contribution of the individual F-VAC to sound radiation can be obtained by projecting structural vibration (normal surface velocity) onto corresponding F-VAC. By analyzing relative contribution of each F-VAC, the critical vibration component that directly responsible for sound radiation can be identified.

5.2 Forced Vibro-acoustic Component (F-VAC)

In this section, we will illustrate how to factorize the correlations between sound and vibration into an orthogonal basis system known as F-VAC. According to different application

requirements, there are two approaches to do the decomposition. If noise control targets at few particular field locations, F-VACs should be determined through spatially averaged square value of reconstructed sound pressures at desired locations. If noise control aims at reducing overall radiated acoustic power, F-VACs need to be evaluated with respect to the total radiated acoustic power. Next, these two approaches will be illustrated respectively.

5.2.1 F-VAC decomposition regarding spatially averaged square value of sound pressures

In modified HELS approach, the sound pressures at *N* field points $\left\{\mathbf{x}_n^{rec}\right\}$ can be reconstructed based on normal surface velocity at *M* surface locations $\left\{\mathbf{x}_m^{rec}\right\}$ through equation (3.28) which is duplicated below as equation (5.1).

$$\left\{\hat{p}\left(\mathbf{x}_n^{rec};\omega\right)\right\}_{N\times 1}=\left[G_{\hat{p}\hat{v}_n}\left(\mathbf{x}_n^{rec}\,|\,\mathbf{x}_m^{rec};\omega\right)\right]_{N\times M}\left\{\hat{v}_n\left(\mathbf{x}_m^{rec};\omega\right)\right\}_{M\times 1}, \tag{5.1}$$

where $G_{\hat{p}\hat{v}_n}\left(\mathbf{x}_n^{rec}\,|\,\mathbf{x}_m^{rec};\omega\right)$ donates the regularized transfer matrices that correlate surface normal surface velocities at *M* locations to sound pressures at *N* locations. Such transfer matrices are regularized per sound pressures measured at *N* supplemented field locations near reconstructed locations. If noise control just target at the areas near these reconstructed filed locations, we can simply use spatial averaged square value of reconstructed sound pressures to obtain F-VAC. The spatial averaged square value of sound pressures can be calculated as follows

$$\left\langle\hat{p}^2\left(\mathbf{x}_n^{rec};\omega\right)\right\rangle=\frac{1}{N}\left\{\hat{p}\left(\mathbf{x}_n^{rec};\omega\right)\right\}_{1\times N}^{H}\left\{\hat{p}\left(\mathbf{x}_n^{rec};\omega\right)\right\}_{N\times 1}. \tag{5.2}$$

For finding contribution of individual components, $\left\{\hat{p}\left(\mathbf{x}_n^{rec};\omega\right)\right\}_{N\times 1}$ in equation (5.2) is replaced by equation (5.1). And for easy reference, spatial averaged square sound pressures $\left\langle\hat{p}^2\left(\mathbf{x}_n^{rec};\omega\right)\right\rangle$ is replaced with $\Pi(\omega)$.

$$\Pi(\omega)=\frac{1}{N}\left\{\hat{v}_n\left(\mathbf{x}_m^{rec};\omega\right)\right\}_{1\times M}^{H}\left[G_{\Pi\hat{v}_n}\left(\mathbf{x}_n^{rec}\,|\,\mathbf{x}_m^{rec};\omega\right)\right]_{M\times M}\left\{\hat{v}_n\left(\mathbf{x}_m^{rec};\omega\right)\right\}_{M\times 1}, \tag{5.3}$$

where $\left[G_{\Pi\hat{v}_n}\left(\mathbf{x}_n^{rec}\,|\,\mathbf{x}_m^{rec};\omega\right)\right]_{M\times M}$ is the transfer matrices that correlates normal surface velocity to averaged square value of sound pressures. It can be calculated as follows

$$\left[G_{\Pi\hat{v}_n}\left(\mathbf{x}_n^{rec}\,|\,\mathbf{x}_m^{rec};\omega\right)\right]_{M\times M}=\left[G_{\hat{p}\hat{v}_n}\left(\mathbf{x}_n^{rec}\,|\,\mathbf{x}_m^{rec};\omega\right)\right]_{M\times N}^{H}\left[G_{\hat{p}\hat{v}_n}\left(\mathbf{x}_n^{rec}\,|\,\mathbf{x}_m^{rec};\omega\right)\right]_{N\times M}. \tag{5.4}$$

The transfer matrix $\left[G_{\Pi\hat{v}_n}\left(\mathbf{x}_n^{rec}\,|\,\mathbf{x}_m^{rec};\omega\right)\right]_{M\times M}$ is calculated through multiplying $\left[G_{\hat{p}\hat{v}_n}\left(\mathbf{x}_n^{rec}\,|\,\mathbf{x}_m^{rec};\omega\right)\right]_{N\times M}$ by its complex conjugate transpose, so it is a Hermitian matrix. It is known that the singular value of this special matrix must be real, and the corresponding singular vectors are linearly independent with each other. Mathematically, singular value decomposition of $\left[G_{\Pi\hat{v}_n}\left(\mathbf{x}_n^{rec}\,|\,\mathbf{x}_m^{rec};\omega\right)\right]_{M\times M}$ is expressed as below

$$\left[G_{\Pi\hat{v}_n}\left(\mathbf{x}_n^{rec}\,|\,\mathbf{x}_m^{rec};\omega\right)\right]_{M\times M}=[U_{\Pi\hat{v}_n}]_{M\times M}[\Sigma_{\Pi\hat{v}_n}]_{M\times M}[U_{\Pi\hat{v}_n}]_{M\times M}^{H}, \tag{5.5}$$

where $U_{\Pi\hat{v}_n}$ is all unitary matrices and $\Sigma_{\Pi\hat{v}_n}$ is a $M\times M$ rectangular diagonal matrix with positive real numbers on the diagonal. To introduce the concept of F-VAC, suppose that matrices $U_{\Pi\hat{v}_n}$ is decomposed into its column vectors and $\Sigma_{\Pi\hat{v}_n}$ is written in matrix form, we have

$$[U_{\Pi\hat{v}_n}]_{M\times M}=\left[u_{\Pi\hat{v}_n,1},u_{\Pi\hat{v}_n,2},\ldots u_{\Pi\hat{v}_n,M}\right], \tag{5.6}$$

$$[\Sigma_{\Pi\hat{v}_n}]_{M\times M}=\begin{bmatrix}\sigma_{\Pi\hat{v}_n,1} & 0 & \cdots & 0\\ 0 & \sigma_{\Pi\hat{v}_n,2} & \cdots & 0\\ \vdots & \vdots & \ddots & \vdots\\ 0 & 0 & \cdots & \sigma_{\Pi\hat{v}_n,M}\end{bmatrix}, \tag{5.7}$$

where $u_{\Pi\hat{v}_n,i}$ is *i*th column of $U_{\Pi\hat{v}_n}$ and $\sigma_{\Pi\hat{v}_n,i}$ is corresponding *i*th singular value. These columns of $U_{\Pi\hat{v}_n}$ represent the forced vibro-acoustic components for structural vibration, so the term F-VAC is used to represent these vectors $u_{\Pi\hat{v}_n,i}$, *i*=1,2,3 …, *M*. Since F-VAC is just a set of orthogonal basis functions, the plotted individual F-VAC shape doesn't directly shed light on what vibration component needs to be suppressed. Only when projecting normal surface velocity onto these F-VAC, can you obtain the target vibration deflection shape.

The singular values $\sigma_{\Pi\hat{v}_n,i}$ are ordering in descending manner, so it is seemingly that the first few F-VACs whose singular values are larger are dominant factors in sound radiation at frequency ω. However, there is more to it. The singular value alone cannot identify individual F-VAC component's contribution to sound radiation. This is because transfer matrices $G_{\Pi\hat{v}_n}\left(\mathbf{x}_n^{rec}\,|\,\mathbf{x}_m^{rec};\omega\right)$ are governed by geometry information of source surface, desired locations where the sound radiation are reconstructed and corresponding boundary conditions. It doesn't include the effects of different vibration components radiation ability. F-VAC with larger singular value may not necessary radiate more acoustic energy than F-VAC component associated with smaller singular value. Hence, to evaluate the importance of each F-VAC, source structures vibration information must also be taken into consideration. So, in order to identify the importance of each F-VAC, we recast the transfer matrices $\left[G_{\Pi\hat{v}_n}\left(\mathbf{x}_n^{rec}\,|\,\mathbf{x}_m^{rec};\omega\right)\right]_{M\times M}$ as products of these column vectors and corresponding singular value,

$$\left[G_{\Pi\hat{v}_n}\left(\mathbf{x}_n^{rec}\,|\,\mathbf{x}_m^{rec};\omega\right)\right]_{M\times M}=\sum_{i=1}^{M}\left[u_{\Pi\hat{v}_n,i}\right]_{M\times 1}\sigma_{\Pi\hat{v}_n,i}\left[u_{\Pi\hat{v}_n,i}\right]_{1\times M}^{H}. \tag{5.8}$$

Substituting equation (5.8) into equation (5.3) yields the correlation between structural vibration and spatial averaged square value of sound pressure in terms of decomposed singular values and corresponding F-VACs

$$\begin{aligned}\Pi(\omega) &= \frac{1}{N}\sum_{i=1}^{M}\left\{\hat{v}_n\left(\mathbf{x}_m^{rec};\omega\right)\right\}_{1\times M}^{H}\left[u_{\Pi\hat{v}_n,i}\right]_{M\times 1}\sigma_{\Pi\hat{v}_n,i}\left[u_{\Pi\hat{v}_n,i}\right]_{1\times M}^{H}\left\{\hat{v}_n\left(\mathbf{x}_m^{rec};\omega\right)\right\}_{M\times 1} \\ &= \frac{1}{N}\sum_{i=1}^{M}\sigma_{\Pi\hat{v}_n,i}\left|\left\{\hat{v}_n\left(\mathbf{x}_m^{rec};\omega\right)\right\}_{1\times M}^{H}\left[u_{\Pi\hat{v}_n,i}\right]_{M\times 1}\right|^2.\end{aligned} \tag{5.9}$$

Equation (5.9) can be interpreted as projecting reconstructed normal surface velocities onto a basis system known as F-VACs and contribution of each projection to spatial averaged square value of sound pressure at interested field points is indicated by corresponding singular value combined with normal surface velocities. Thus, by comparing relative contribution of each F-VAC to $\Pi(\omega)$ under certain excitation condition, critical vibration component for undesired sound radiation can be determined. Mathematically, the relative contribution of *i*th F-VAC to sound radiated at frequency ω can be expressed as below

$$\vartheta_{\Pi\hat{v}_n,i}(\omega) = \frac{\sigma_{\Pi\hat{v}_n,i}\left|\left\{\hat{v}_n\left(\mathbf{x}_m^{rec};\omega\right)\right\}_{1\times M}^{H}\left[u_{\Pi\hat{v}_n,i}\right]_{M\times 1}\right|^2}{\sum_{i=1}^{M}\sigma_{\Pi\hat{v}_n,i}\left|\left\{\hat{v}_n\left(\mathbf{x}_m^{rec};\omega\right)\right\}_{1\times M}^{H}\left[u_{\Pi\hat{v}_n,i}\right]_{M\times 1}\right|^2}\times 100\%. \tag{5.10}$$

The theoretical noise control potential of each F-VAC is also indicated by the ratio $\vartheta_{\Pi\hat{v}_n,i}$. However, in practice, the theoretical value is hard to be achieved by suppressing identified vibration component. Since suppressing certain vibration component without changing other structural properties is impossible in reality. Even so, it doesn't stop F-VAC analysis based structure-borne noise control to be the most cost-effective approach. Simply because the dominant vibration components to sound radiation are obtained through interrelationships between sound and vibration.

5.2.2 F-VAC decomposition regarding sound power

If the objective is to control acoustic power radiated into the entire field, it is necessary to find the critical vibration component that contributes most to sound power radiation and suppress it. To this end, F-VAC needs to be identified through interrelationship between surface vibration and radiated sound power.

Assume that the vibrating surface is divided into *K* discrete elements and area of the *k*th element is $\Delta S(k)$. There are *M* number of reconstructed locations $\left\{\mathbf{x}_m^{rec}\right\}_{M\times 1}$ on the entire surface and they are specially sorted per discretization process. The first discretized element contains points $\mathbf{x}_1^{rec}, \mathbf{x}_2^{rec}, \ldots \mathbf{x}_{S_1}^{rec}$ and when *k*>1, $\mathbf{x}_{S_{k-1}+1}^{rec}, \mathbf{x}_{S_{k-1}+2}^{rec}, \ldots \mathbf{x}_{S_k}^{rec}$ form the points set for the *k*th element. So, there are S_1 number of points in the first element and there are S_k- S_{k-1} number of points in the *k*th element. The sound power radiated from vibrating structure is calculated by summation of contributions of sound power radiated from each of the discretized surface element. Mathematically, such a relationship is expressed in equation (3.34) which is duplicated here as equation (5.11)

$$P(\omega) = \sum_{k=1}^{K} \Delta S(k) \left\langle \hat{I}_n\left(\mathbf{x}^{rec};\omega\right)\right\rangle_k . \tag{5.11}$$

where $\left\langle \hat{I}_n\left(\mathbf{x}^{rec};\omega\right)\right\rangle_k = \frac{1}{S_k - S_{k-1}} \sum_{i=S_{k-1}+1}^{S_k} \hat{I}_n\left(\mathbf{x}_i^{rec,};\omega\right)$ donates the spatial averaged normal component of sound intensity on the *k*th element. The time-averaged acoustic intensities on the entire surface at locations $\mathbf{x}_m^{rec}$, *m* = 1, 2, … M, are calculated by the product of the complex conjugate of the normal surface velocity and the complex amplitude of sound pressure at the same locations

$$\left\{\hat{I}_n\left(\mathbf{x}_m^{rec};\omega\right)\right\}_{M\times 1} = \frac{1}{2}\mathrm{Re}\left(\left\{\hat{p}\left(\mathbf{x}_m^{rec};\omega\right)\right\}_{M\times 1}.\left\{\hat{v}_n^{\,*}\left(\mathbf{x}_m^{rec};\omega\right)\right\}_{M\times 1}\right). \tag{5.12}$$

The M number of normal surface velocities on the entire surface are reconstructed from L number of measurement locations $\mathbf{x}_l^{meas}$,$l = 1, 2, \ldots$ L, through equations (3.24) and N number of sound pressures are further reconstructed from these normal surface velocities through equation (3.28). These two equations are duplicated here as equation (5.13) and (5.14)

$$\left\{\hat{v}_n\left(\mathbf{x}_m^{rec};\omega\right)\right\}_{M\times 1} = \left[H_{\hat{v}_n\hat{v}_n}\left(\mathbf{x}_m^{rec}\,|\,\mathbf{x}_l^{meas};\omega\right)\right]_{M\times L}\left\{\hat{v}_n\left(\mathbf{x}_l^{meas};\omega\right)\right\}_{L\times 1}, \tag{5.13}$$

$$\left\{\hat{p}\left(\mathbf{x}_n^{rec};\omega\right)\right\}_{N\times 1} = \left[G_{\hat{p}\hat{v}_n}\left(\mathbf{x}_n^{rec}\,|\,\mathbf{x}_m^{rec};\omega\right)\right]_{N\times M}\left\{\hat{v}_n\left(\mathbf{x}_m^{rec};\omega\right)\right\}_{M\times 1}. \tag{5.14}$$

Note that in equation (5.12), surface sound pressures and normal surface velocities at the same locations are needed. So, equation (5.14) is rewritten to equation (5.15) by replacing $\mathbf{x}_n^{rec}$ with $\mathbf{x}_m^{rec}$

$$\left\{\hat{p}\left(\mathbf{x}_m^{rec};\omega\right)\right\}_{M\times 1} = \left[G_{\hat{p}\hat{v}_n}\left(\mathbf{x}_m^{rec}\,|\,\mathbf{x}_m^{rec};\omega\right)\right]_{M\times M}\left\{\hat{v}_n\left(\mathbf{x}_m^{rec};\omega\right)\right\}_{M\times 1}, \tag{5.15}$$

where $\left[G_{\hat{p}\hat{v}_n}\left(\mathbf{x}_m^{rec}\,|\,\mathbf{x}_m^{rec};\omega\right)\right]_{M\times M}$ donates the transfer matrices for this special case that surface sound pressures at the same locations are desired. The reason of using a new term for this transfer function is not simply because of the differences in the number of reconstruction locations, its regularization process also differs from $\left[G_{\hat{p}\hat{v}_n}\left(\mathbf{x}_n^{rec}\,|\,\mathbf{x}_m^{rec};\omega\right)\right]_{N\times M}$.

In chapter 3, the transfer function $\left[G_{\hat{p}\hat{v}_n}\left(\mathbf{x}_n^{rec}\,|\,\mathbf{x}_m^{rec};\omega\right)\right]_{N\times M}$ is regularized with respect to another set of verification or benchmark data. However, instead of surface acoustic pressure, it is field acoustic pressures that are reconstructed in chapter 3. To use the same approach to reconstruct surface acoustic pressure, the verification data must be acquired in the near field around target surface by using an arbitrarily shaped microphone array just as traditional NAH, which is against our original intention. So, we are in the position of regularizing $G_{\hat{p}\hat{v}_n}$ without benchmark data.

Our solution is placing a constraining condition on the time-averaged acoustic power to determine the optimal number of expansion terms J_{opp}. Mathematically, the optimization process is expressed in equation

$$\min_{J}\left\langle\left[G_{\hat{p}\hat{v}_n}\left(\mathbf{x}_m^{rec}\,|\,\mathbf{x}_m^{rec};\omega\right)\right]_{M\times M}\left\{\hat{v}_n\left(\mathbf{x}_m^{rec};\omega\right)\right\}_{M\times 1}\left\{\hat{v}_n^{*}\left(\mathbf{x}_m^{rec};\omega\right)\right\}_{1\times M}^{H}\right\rangle\rightarrow J_{\text{opp}}, \tag{5.16}$$

Next, we do singular value decomposition to the transfer matrices and substitute them back into equation (5.15). Mathematically, it is expressed as below

$$\left\{\hat{p}\left(\mathbf{x}_m^{rec};\omega\right)\right\}_{M\times 1}=[V_{\hat{p}\hat{v}_n}]_{M\times M}[\Sigma_{\hat{p}\hat{v}_n}]_{M\times M}[U_{\hat{p}\hat{v}_n}]_{M\times M}^{H}\left\{\hat{v}_n\left(\mathbf{x}_m^{rec};\omega\right)\right\}_{M\times 1}, \tag{5.17}$$

Since $\left[G_{\hat{p}\hat{v}_n}\left(\mathbf{x}_m^{rec}\,|\,\mathbf{x}_m^{rec};\omega\right)\right]_{M\times M}$ is no longer a Hermitian positive matrix, unlike SVD of $\left[G_{\Pi\hat{v}_n}\left(\mathbf{x}_n^{rec}\,|\,\mathbf{x}_m^{rec};\omega\right)\right]_{M\times M}$ in equation (5.5), $V_{\hat{p}\hat{v}_n}$ and $U_{\hat{p}\hat{v}_n}$ are different. However, they still define two sets of orthogonal basis functions. Physically, $V_{\hat{p}\hat{v}_n}$ represents the vibro-acoustic components for surface acoustic pressure whereas $U_{\hat{p}\hat{v}_n}$ represent the forced vibro-acoustic components for structural vibration. So, columns of $U_{\hat{p}\hat{v}_n}$ are F-VACs obtained through controlling total acoustic power radiated from vibrating structure.

Similar to equation (5.8), $\left[G_{\hat{p}\hat{v}_n}\left(\mathbf{x}_m^{rec}\,|\,\mathbf{x}_m^{rec};\omega\right)\right]_{M\times M}$ is decomposed as outer product summation as shown in equation (5.18)

$$\left[G_{\hat{p}\hat{v}_n}\left(\mathbf{x}_m^{rec}\,|\,\mathbf{x}_m^{rec};\omega\right)\right]_{M\times M}=\sum_{i=1}^{M}\left[v_{\hat{p}\hat{v}_n,i}\right]_{M\times 1}\sigma_{\hat{p}\hat{v}_n,i}\left[u_{\hat{p}\hat{v}_n,i}\right]_{1\times M}^{H}, \tag{5.18}$$

where $v_{\hat{p}\hat{v}_n,i}$, i=1,2, … M, are columns of $V_{\hat{p}\hat{v}_n}$ and $u_{\hat{p}\hat{v}_n,i}$, i=1,2, … M, are columns of $U_{\hat{p}\hat{v}_n}$. Substituting equation (5.18) into equation (5.17), and substituting the result into equation (5.12), we obtain

$$\left\{\hat{I}_n\left(\mathbf{x}_m^{rec};\omega\right)\right\}_{M\times 1}=\sum_{i=1}^{M}\left(\frac{1}{2}\mathrm{Re}\left(\left\{v_{\hat{p}\hat{v}_n,i}\sigma_{\hat{p}\hat{v}_n,i}u_{\hat{p}\hat{v}_n,i}^H\right\}_{M\times M}\left\{\hat{v}_n\left(\mathbf{x}_m^{rec};\omega\right)\right\}_{M\times 1}.\left\{\hat{v}_n^{\,*}\left(\mathbf{x}_m^{rec};\omega\right)\right\}_{M\times 1}\right)\right),$$

(5.19)

As illustrated in previous section, the singular value $\sigma_{\hat{p}\hat{v}_n,i}$ just indicates the rank of *i*th F-VACs in the transfer matrix, hence singular values alone cannot identify F-VAC components that are mainly responsible for sound power radiation. However, the dominant F-VAC can be obtained by analyzing equation (5.19). The radiated sound intensity related to the *i*th F-VAC can be expressed as below

$$\left\{\hat{I}_{n,i}\left(\mathbf{x}_m^{rec};\omega\right)\right\}_{M\times 1}=\frac{1}{2}\mathrm{Re}\left(\left\{v_{\hat{p}\hat{v}_n,i}\sigma_{\hat{p}\hat{v}_n,i}u_{\hat{p}\hat{v}_n,i}^H\right\}_{M\times M}\left\{\hat{v}_n\left(\mathbf{x}_m^{rec};\omega\right)\right\}_{M\times 1}.\left\{\hat{v}_n^{\,*}\left(\mathbf{x}_m^{rec};\omega\right)\right\}_{M\times 1}\right). \quad (5.20)$$

What needs illustration is that although the time averaged acoustic intensity is obtained from surface acoustic quantities, it naturally indicates acoustic energy which will propagate into far-field. It is because that contribution of evanescent wave which not propagates into far-field is represented by the imaginary part of $\hat{p}\hat{v}_n^{\,*}$, by taking real part of $\hat{p}\hat{v}_n^{\,*}$, evanescent waves are excluded automatically. Substituting equation (5.20) into equation (5.11) could naturally lead us to the radiated acoustic power related to *i*th F-VAC

$$P_i(\omega)=\sum_{k=1}^{K}\Delta S(k)\left\langle\hat{I}_{n,i}\left(\mathbf{x}^{rec};\omega\right)\right\rangle_k. \quad (5.21)$$

Having the individual F-VAC's contribution to radiated acoustic power, the relative contribution of each F-VAC to sound radiation can be calculated as

$$\vartheta_{\hat{p}\hat{v}_n,i}=\frac{P_i(\omega)}{P(\omega)}\times 100\%. \quad (5.22)$$

5.3 Comparison between F-VACs and normal modes

F-VACs provide us a powerful tool to analysis sound generated by vibrating structures and structure's normal modes are very helpful for understanding structure vibration. They are totally different concepts.

F-VAC is obtained from the transfer matrices between normal surface velocity and sound radiation, so it directly reveals the link between sound and vibration. Whereas structure's normal modes themselves have nothing to do with sound radiation, they just represent independent vibration patterns. To establish a link between normal modes and sound radiation, the concept of radiation efficiency, which gives out certain mode's ability to radiate sound into far-field, is induced. However, it still cannot change the fact that normal modes are not directly related to sound radiation. So, suppressing vibration of normal mode with highest radiation efficiency may not provide satisfactory results. In order to get the best noise reduction results, contributions from several dominant modes need to be considered together, which is obvious, not economic.

Another difference is that natural modes are observable at resonant frequencies and each mode describes a unique vibration pattern. Quite the contrary, in terms of their shapes, F-VACs are non-observable and don't have intuitive physical meanings. Although F-VACs sometimes may look like nature modes shapes or ODS, they are just a set of basis vector system which is established through mathematical manipulations. The physical value of F-VACs is that, through projecting surface vibration onto them and applying certain constraining conditions, critical vibration component related to undesired radiated sound can be identified. Such information will further cast light on controlling structural borne noise in an effective manner.

Also, F-VACs are dependent on external excitation forces whereas nature modes are dynamic properties of a structure and are unconnected with excitation conditions.

5.4 Conclusion

In this chapter, the concept of F-VAC is discussed in detail, including mathematic formulas and its physical meaning. Since in terms of plotted shapes, the projection of normal surface velocity onto F-VAC look quite the same with structure normal mode shapes, the differences between F-VAC and normal mode are also given. F-VAC directly correlates structure vibration with sound radiation, so, it naturally sheds lights on how to reduce sound generated by structure vibration. Experimental determination of F-VACs and validation of F-VAC analysis based noise control will be demonstrated in next chapter.

CHAPTER 6: EXPERIMENTAL VALIDATION

In previous chapters, a modified HELS method based on combined normal surface velocities and field acoustic pressures and F-VAC analysis based structure borne noise control strategy are introduced mathematically. Here, in this chapter, a series of experiments are conducted to validate these theories.

6.1 Introduction

There are three main purposes of these experiments. First, the effectiveness of reconstructing the whole vibro-acoustic field based on normal surface velocities measurements by using modified HELS approach need to be verified. Then the dominant F-VAC responsible for specific radiated sound is required to be discerned by decomposition of the acquired transfer functions. Finally, comparison of noise reduction results between proposed F-VAC based approach and traditional modal analysis based approach is demonstrated.

So, in subsection 6.3, reconstructed normal surface velocities and field pressures are compared with measured benchmark data. In subsection 6.4, critical vibration components responsible for target noise reduction are identified through F-VAC analysis. In section 6.5, we suppress vibration component according to model analysis and F-VAC analysis respectively. Then their noise reduction results are compared with each other.

6.2 Test Setup

The experiment is conducted inside a fully anechoic chamber. The test object is the top surface of a metal cookie box. During the test, a Bluetooth speaker which is placed inside the cookie box is acting as the excitation source. To ensure that most of the sound is radiated from the top surface, the cookies box is put into a wooden box and enclosed with sound absorption foams. The normal surface velocities are measured by laser vibrometer and the sound pressures in the field are collected by a microphone array.

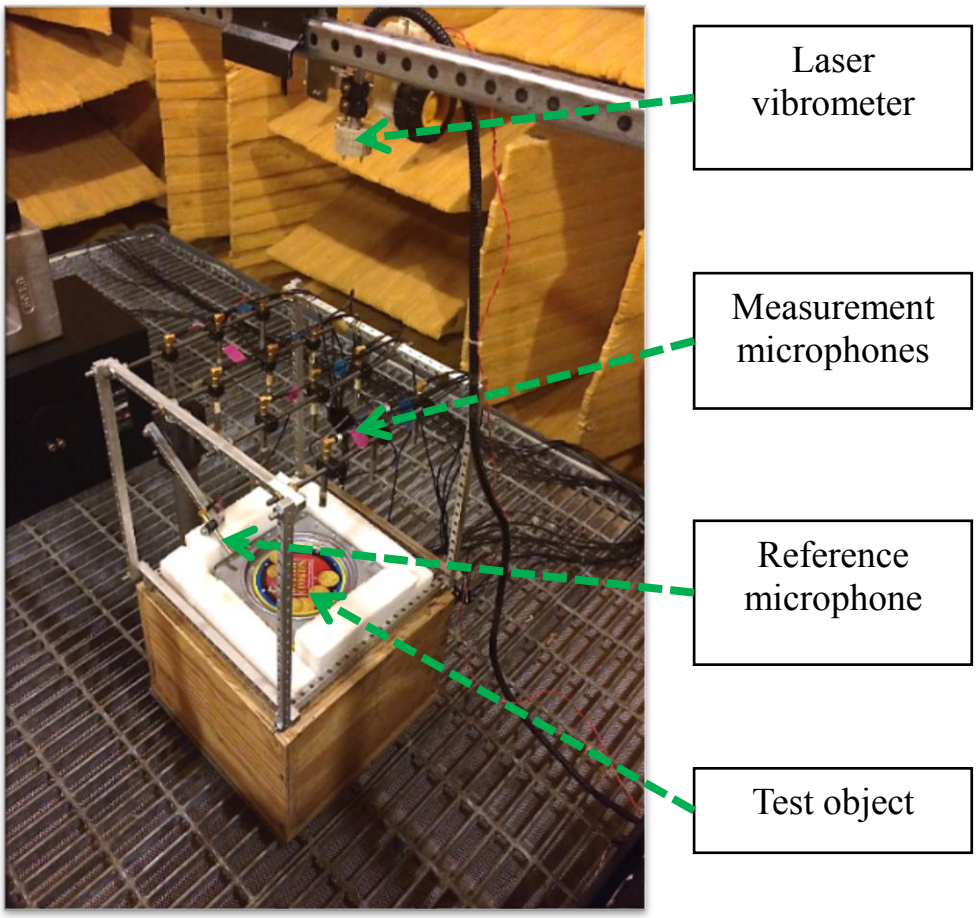

Figure 6.1 Experimental setup

Figure 6.1 shows the detailed experimental setup inside the anechoic chamber. The surface vibration of the top surface and its sound radiation is our target. Note that the top surface is not simple clamped plate, it's a highly non-spherical surface and the round lid in the center make it even more complicated. The single channel laser vibrometer head is located on the top. So, in order to measure normal surface velocities distribution at 32 locations (Figure 6.4) on the surface, 32 times of measurements are needed and the laser head are manually moved to next position each time. Therefore, phase discrepancy between different measurement exist. To compensate for these discrepancies, a reference microphone is put in the nearfield. There are another 12 microphones taking measurement in the far-field at a stand-off distance of 43 cm above the top surface. They

are used to determine optimal expansion coefficients and their measurements are also served as benchmark data to compare the noise reduction results.

Figure 6.2 Test object

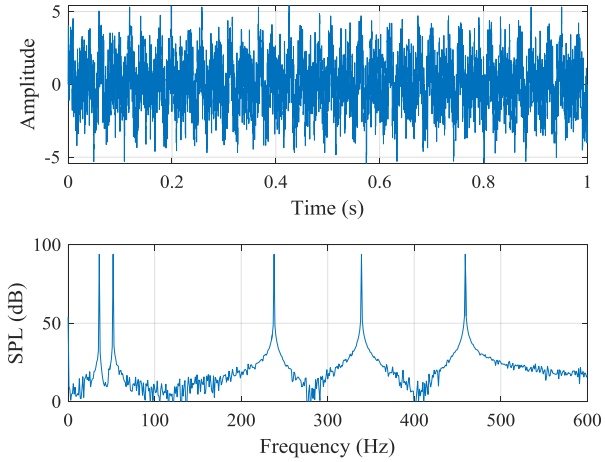

Figure 6.3 Excitation signals

A Bluetooth speaker playing excitation signals inside the cookie box act as excitation source (figure 6.2). In order to make sure that most of the sounds detected by microphones are radiated from the top surface, adhesive vibration damping tapes are put onto the other 5 surfaces which dramatically constrain their vibrations. Also, inside the box, the gaps between speaker and those 5 surfaces are filled with sound absorption materials. What's more, as can be seen in figure 6.1, the cookies box is put into a wooden box and enclosed with sound absorption forms during the test. The excitation sound is a mixed signal with peaks at 36Hz, 53Hz, 240Hz, 340Hz and 460Hz. Its waveform and corresponding spectrogram are shown in figure 6.3.

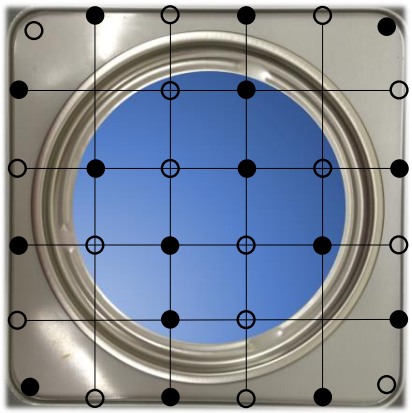

Figure 6.4 32 points measurement locations.
Solid dots: input data points; open dots: validation points.

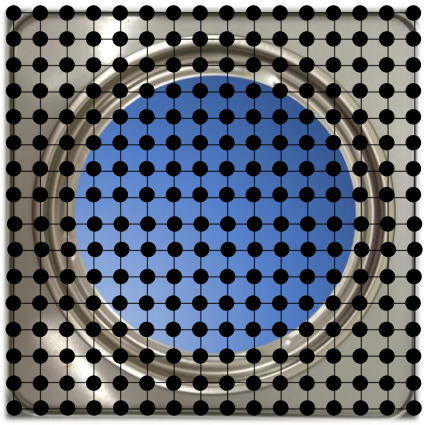

Figure 6.5 256 points reconstruction locations

The 32 normal surface velocity measurement locations as well as 256 reconstruction points distributed on a 16 × 16 grid are shown in figure 6.4 and 6.5. Note that the laser vibrometer cannot provide reliable results on non-flat part of the surface, so 4 points of the 6 × 6 grid which just locate near the lid edge are discarded. As shown in figure 6.4, to find the optimal number of expansion terms in reconstruction of particle velocities, only half of the 32 points indicated by solid dots are used as input data and the other half indicated by open dots are used for verification.

6.3 Reconstruction of vibro-acoustic field

The experiment's first and foremost task is to ensure that the proposed normal surface velocity based NAH could effectively reconstruct the whole vibro-acoustic field, including reconstruction of normal surface velocities and reconstruction of sound pressures.

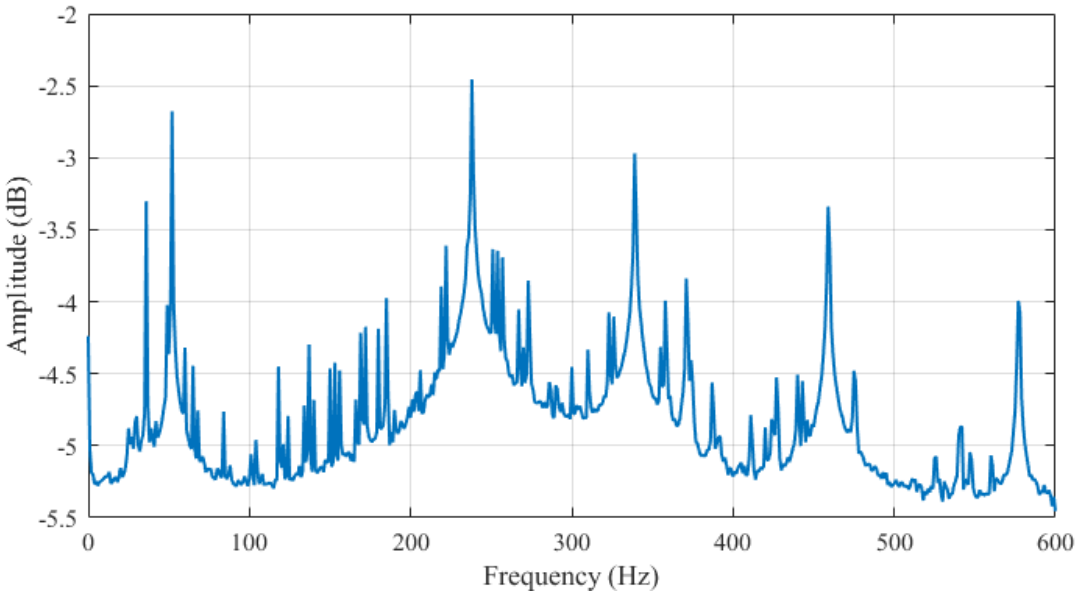

Figure 6.6 Spatial average of the square of measured normal surface velocity

Figure 6.6 demonstrates measured surface vibration response in terms of spatially averaged square value of normal surface velocity. It can be found that there are several obvious peaks at 36 Hz, 53 Hz, 137 Hz, 185 Hz, 240 Hz, 340 Hz, 372 Hz, 460 Hz, 475 Hz and 577Hz. Now that the surface vibration concentrates on these frequencies, we just use these frequencies' vibration to validate the effectiveness of modified HELS approach.

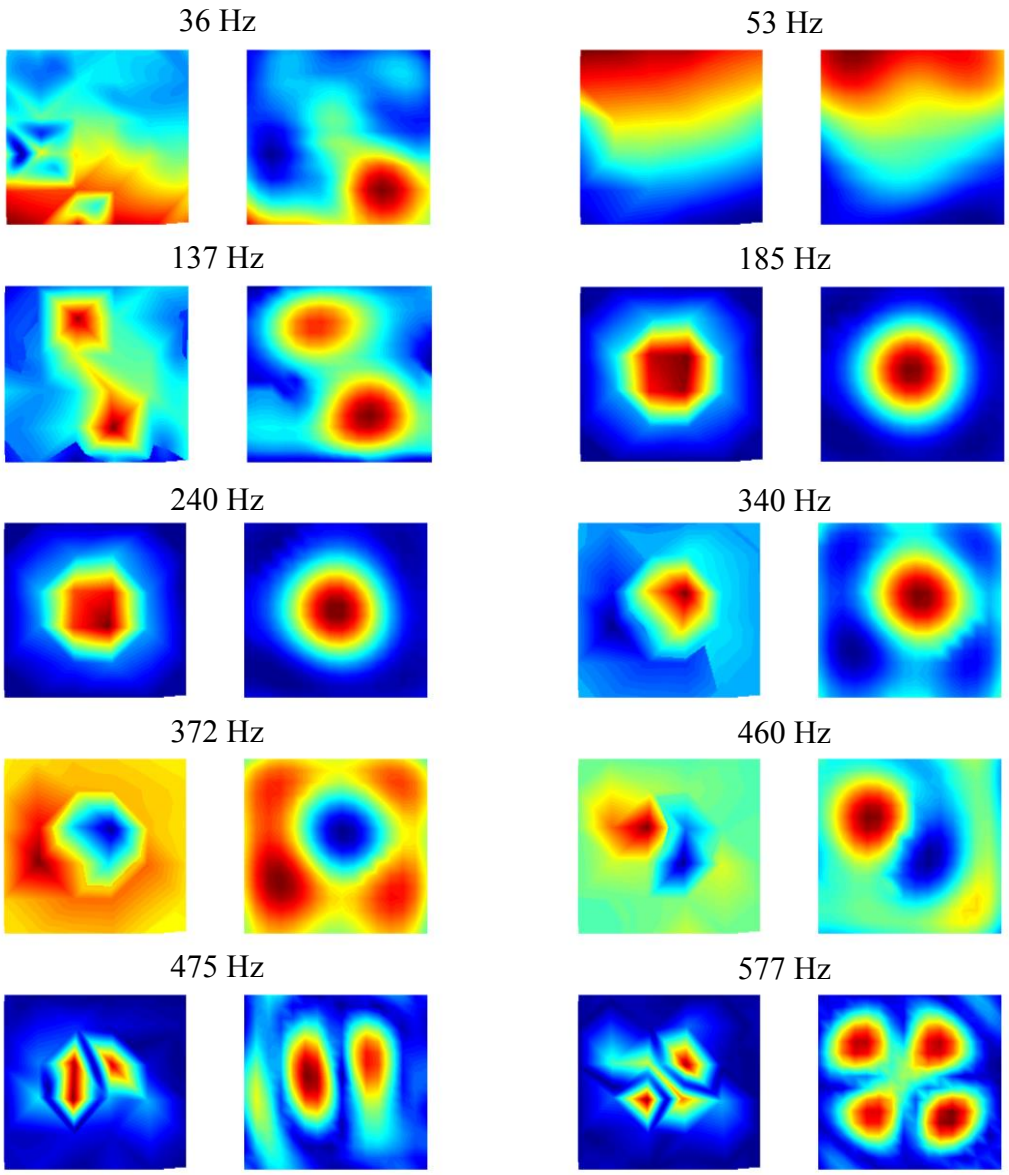

Figure 6.7 Comparisons of reconstructed normal surface velocities at 10 featured frequencies (Left: laser scanning results; Right: reconstructed results.)

Figure 6.7 shows comparisons between directly measured normal surface velocity distribution and reconstructed velocity field at frequencies of interest. The reconstruction results match measured data perfectly at all these frequencies. Compared with 32 points of directly measured data, the reconstructed normal surface velocities, which consist of 256 points, are smother and reveal more details information without satisfying accuracy. Next, these smooth normal surface velocities are used as input to predict sound radiation at 12 measurement locations.

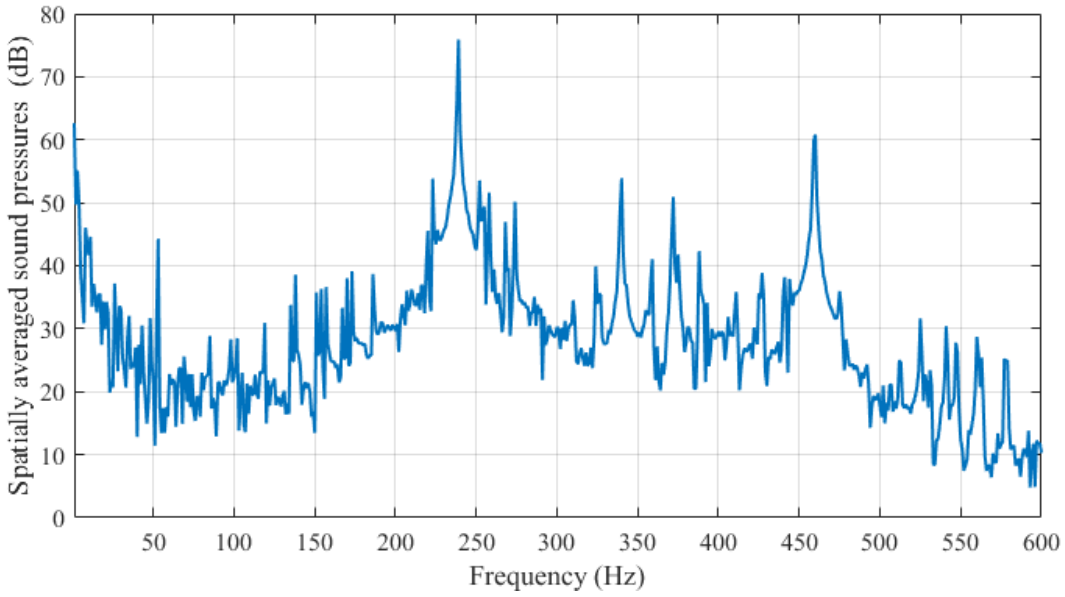

Figure 6.8 Spatial average of the square of measured sound pressures

The spatially averaged square values of sound pressures measured by 12 field microphones are shown in figure 6.8. The two obvious peaks locate at 240Hz and 460 Hz. Compared the spectrum of surface vibration (figure 6.6), it can be found that the vibrations at 36 Hz, 340 Hz and 577 Hz did not radiate much sound into far-field. This proved that sound is caused by vibration, however, not all kind of vibrations will produce sound.

For brevity, instead of comparing reconstruction results at all 12 benchmark microphone locations, we only show sound pressure prediction results at 4 microphone locations (see figure 6.9). The reconstructed spatially averaged square of sound pressures at these 12 microphone locations are also compared with benchmark data in figure 6.10.

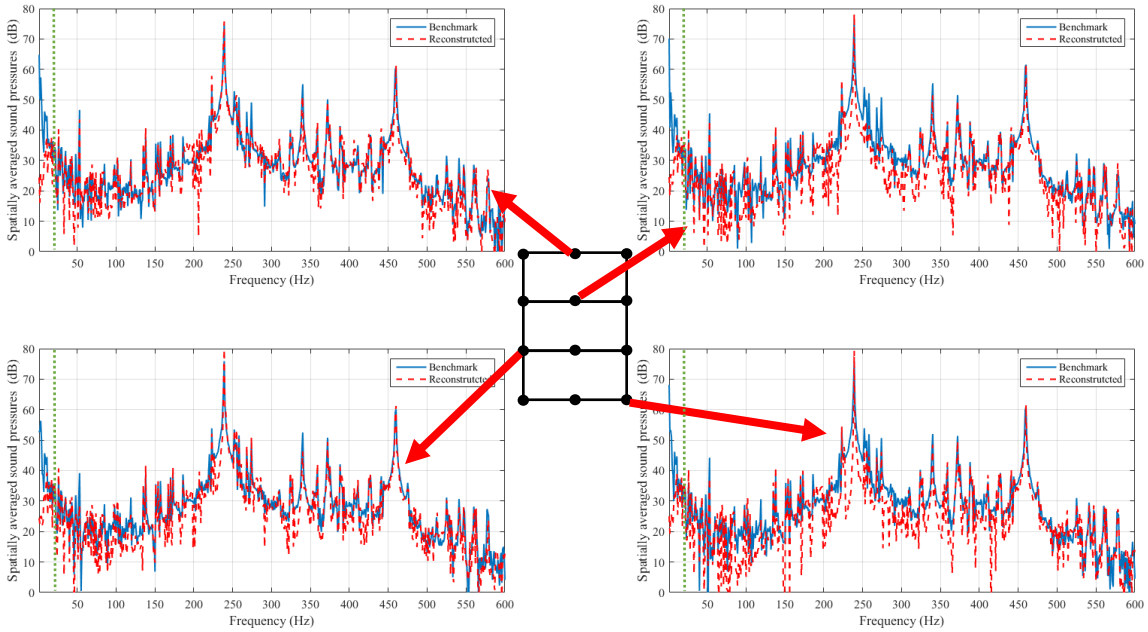

Figure 6.9 Comparisons of sound pressure reconstructions at four randomly selected far-field measurement locations

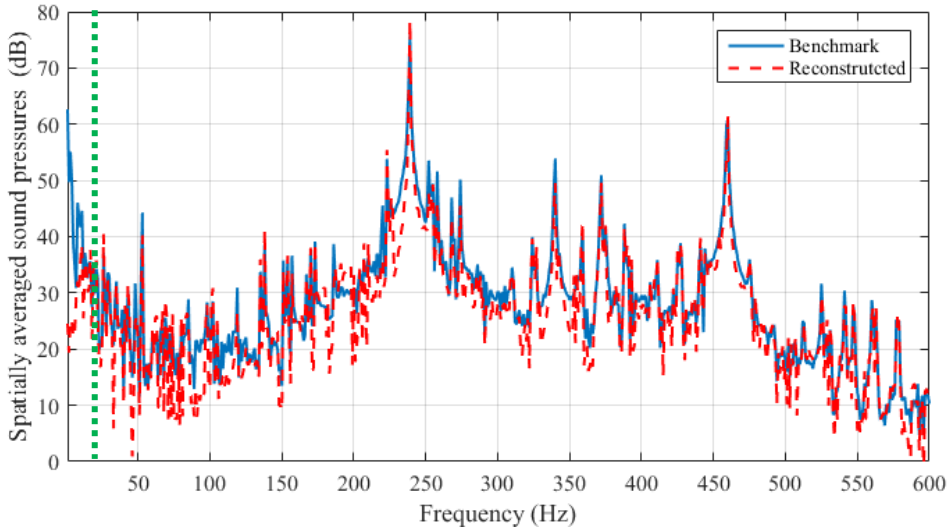

Figure 6.10 Comparisons of reconstructed spatially averaged square of sound pressures

The reconstructed sound pressures agree well with measured data at peak frequencies and their consistency are weaker at off-peak locations. This is because little energy is radiated out to the far-field at off-peak frequencies, undoubtedly leading to low signal to noise ratio (SNR). So, the errors embedded in the input data have more severe impacts on these low SNR frequencies. It can also be found that the prediction precision would become weaker with the increase in

frequency. This is because higher order expansion terms, essential for revealing vibro-acoustic field in higher frequencies, are removed through least-square minimization process. Note that the discrepancies indicated by green dotted lines from 0 to 20 Hz are due to the poor sensitivity of measurement microphones.

The 32 measurement locations cover the whole vibrating surface, however, because laser vibrometer could not provide satisfactory results for non-flat surface, 4 points located just on the lid edge are excluded. These successful reconstructions demonstrate the proposed approach's capability of using partial input data to reconstruct normal surface velocities over the entire surface and further correlate them to the sound radiation in the field. This is significant for practical implementation of NAH. Because there are always obstacles parts around the targeting surface which prevent us from getting vibration information over the entire surface, the flexibility of modified HELS approach could dramatically expand application of NAH theory.

6.4 Determination of F-VACs

Having the interrelationship between sound and vibration, next step is to further decompose these transfer functions into several F-VACs. The importance of each F-VAC is revealed by comparison of their relative contribution to sound radiation. After projecting normal surface velocities onto dominant F-VAC, pivotal vibration component that is accountable for sound radiation can thus be identified.

From figure 6.8, it can be found that peaks at 240 Hz, 340 Hz and 460 Hz are the most obvious ones, so these three frequencies are undoubtedly chosen to be frequency of interest. What's more, in order to demonstrate the flexibility of F-VAC based noise control strategy, except these three dominant frequencies, we also choose another weaker peak at 272 Hz. So, in this experiment, F-VAC decomposition and noise reduction are aiming at three frequencies, 240 Hz, 272 Hz, 340 Hz and 460 Hz.

As illustrated in chapter 5, there are two kinds of F-VAC decompositions. One regarding spatially averaged square value of sound pressures at certain measurement locations, such an approach is appropriate for directional noise control. Whereas the other decomposition target at controlling overall radiated sound power. In this experiment, both these two approaches' effectiveness will be examined.

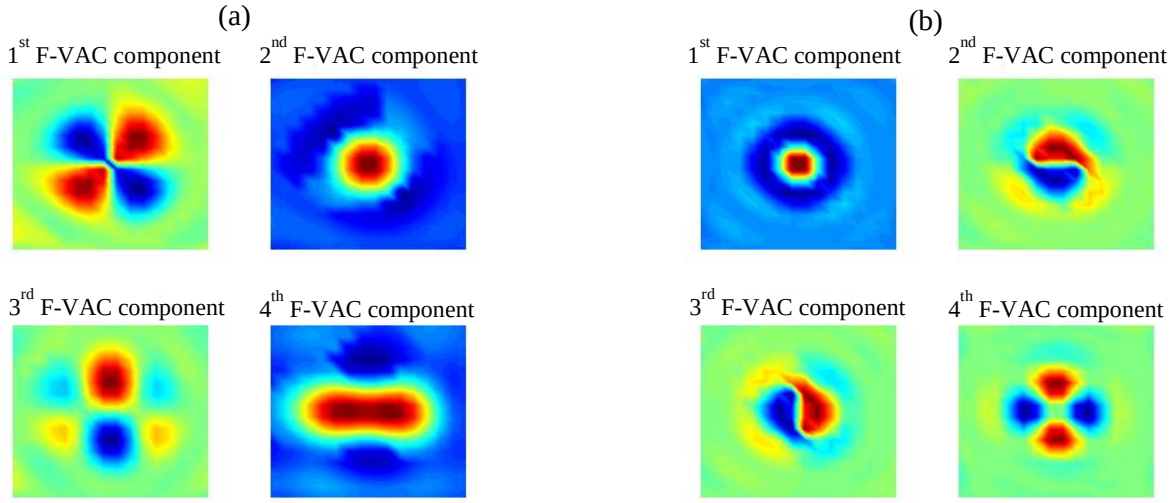

Figure 6.11 First 4 critical vibration components for sound radiation at 240 Hz obtained from F-VAC analysis (a) regarding spatially averaged square of sound pressures; (b) regarding sound power.

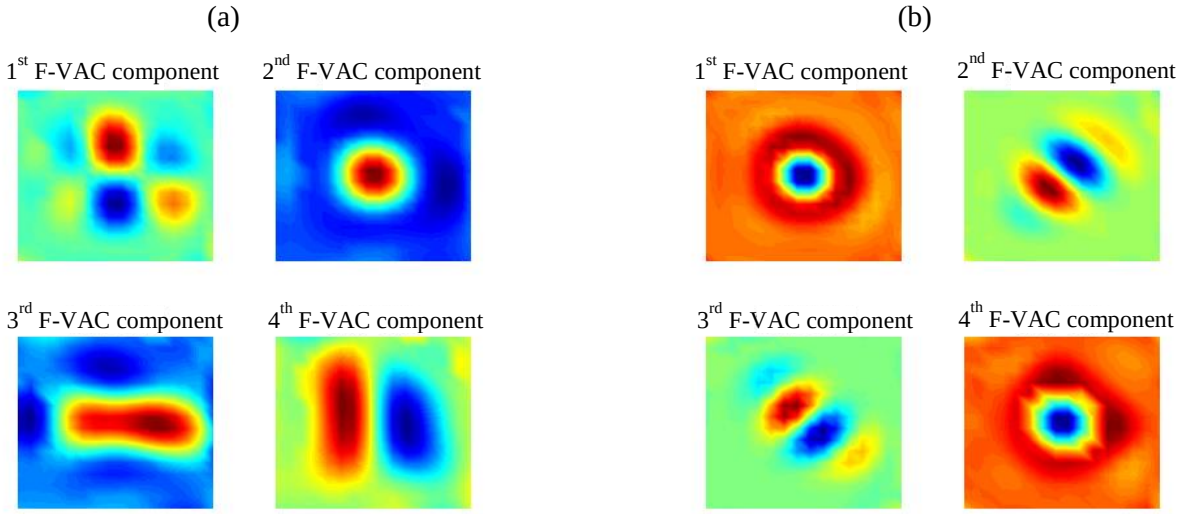

Figure 6.12 First 4 critical vibration components for sound radiation at 272 Hz obtained from F-VAC analysis (a) regarding spatially averaged square of sound pressures; (b) regarding sound power.

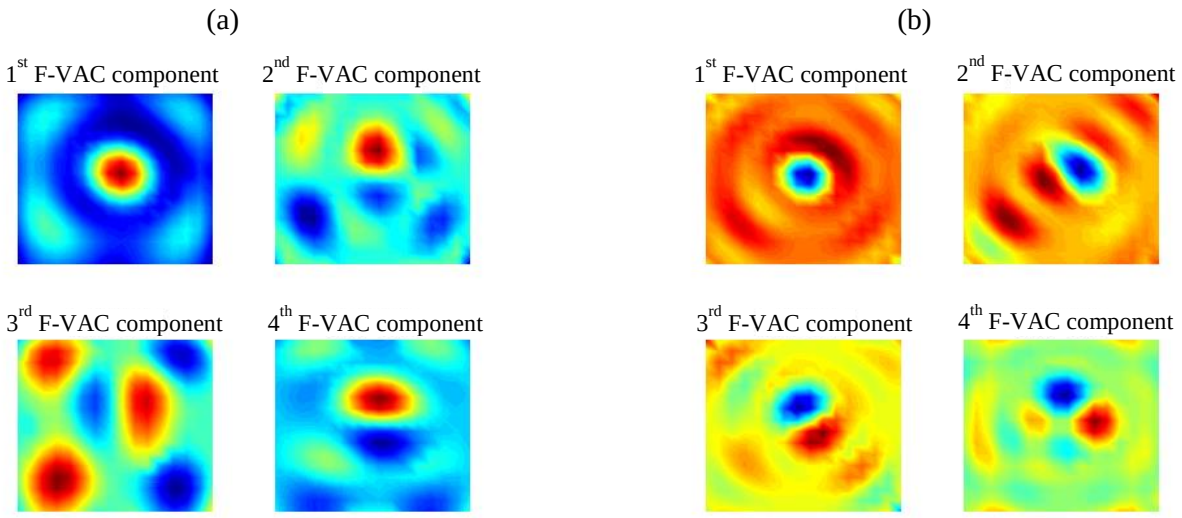

Figure 6.13 First 4 critical vibration components for sound radiation at 340 Hz obtained from F-VAC analysis (a) regarding spatially averaged square of sound pressures; (b) regarding sound power.

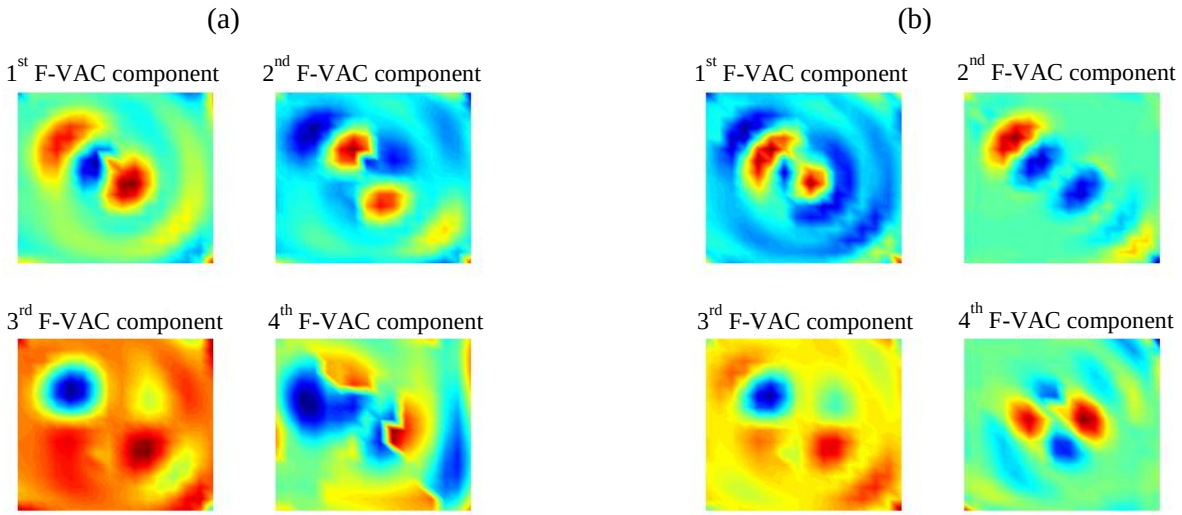

Figure 6.14 First 4 critical vibration components for sound radiation at 460 Hz obtained from F-VAC analysis (a) regarding spatially averaged square of sound pressures; (b) regarding sound power.

Figure 6.11 to figure 6.14 show first 4 crucial vibration components identified from both two kinds of F-VAC decompositions for 4 target frequencies respectively. These shapes are obtained by projecting normal surface velocity distribution onto individual F-VAC. It need to be emphasized again that these projections do look like normal mode shapes, however, they are totally different concepts. Their only common ground is that they all obtained from decomposition of

surface vibration. Except for this, these two concepts don't have any connections. Normal modes are dynamic properties of a structure and they are observable physical quantities. Whereas the projections of surface vibration onto F-VAC are forced vibro-acoustic properties of a structure and they are not observable. As for applications, model analysis is powerful for vibration control and F-VAC analysis is effective for structure borne noise control.

TABLE 6.1 Relative contributions of each vibration component obtained from F-VAC analysis regarding spatially averaged square of sound pressures

	Frequency			
	240 Hz	272 Hz	340 Hz	460 Hz
1st component	88.6%	94.3%	87.0%	51.2%
2nd component	7.3%	5.6%	12.1%	48.7%
3rd component	3.8%	0.1%	0.008%	0.1%
4th component	0.2%	0.01%	0.001%	0.004%

TABLE 6.2 Relative contributions of each vibration component obtained from F-VAC analysis regarding sound power

	Frequency			
	240 Hz	272 Hz	340Hz	460 Hz
1st component	36.7%	80.1%	70.1%	49.1%
2nd component	22.0%	15.8%	18.2%	40.1%
3rd component	20.0%	1.8%	2.6%	6.7%
4th component	4.3%	0.4%	1.3%	1.3%

These vibration components are ordered by their importance for sound radiation and their relative contributions calculated by equation 5.10 and equation 5.22 are listed in table 6.1 and table 6.2. At frequencies 240 Hz and 272 Hz, for F-VAC analysis targeting at spatially averaged square of sound pressures, relative contribution of first vibration component are about 90%, so the noise reduction for these two cases are just focusing at the first vibration component. For other 6 cases, first two or three vibration components need to be combined to get best noise reduction results. The combinations of these individual vibration shapes are listed from figure 6.15 to 6.20.

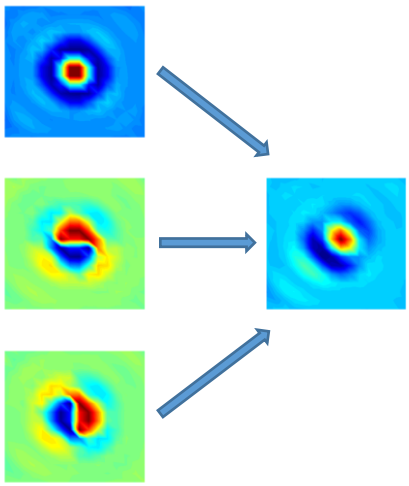

Figure 6.15 Combine first three F-VAC components at 240 Hz (see figure 6.11 (b)).

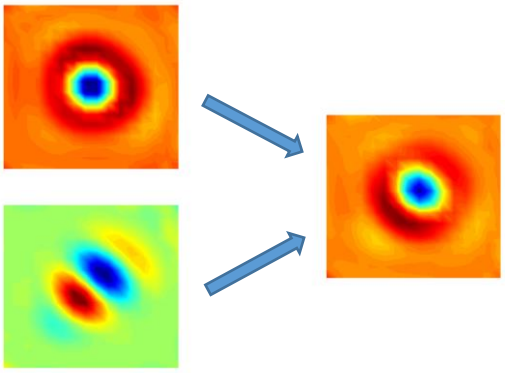

Figure 6.16 Combine 1st and 2nd F-VAC components at 272 Hz (see figure 6.12 (b)).

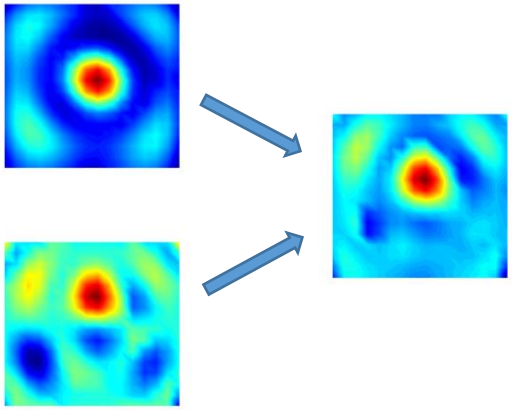

Figure 6.17 Combine 1st and 2nd F-VAC components at 340 Hz (see figure 6.13 (a)).

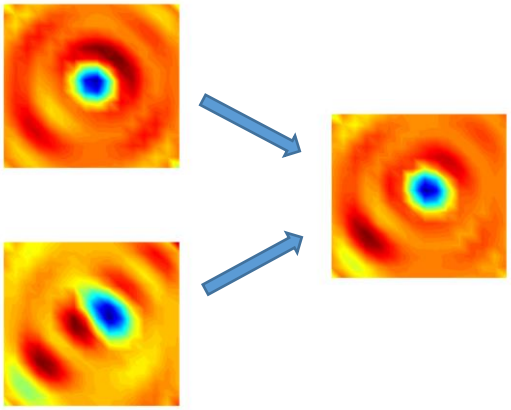

Figure 6.18 Combine 1st and 2nd F-VAC components at 340 Hz (see figure 6.13 (b)).

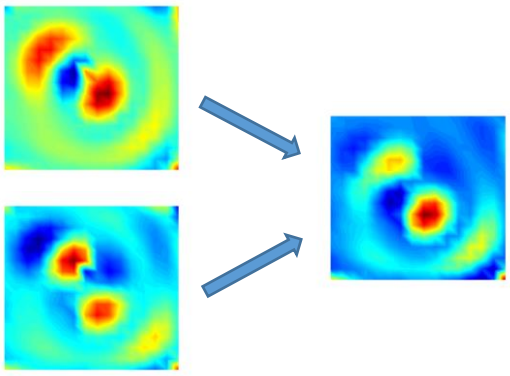

Figure 6.19 Combine 1st and 2nd F-VAC components at 460 Hz (see figure 6.14 (a)).

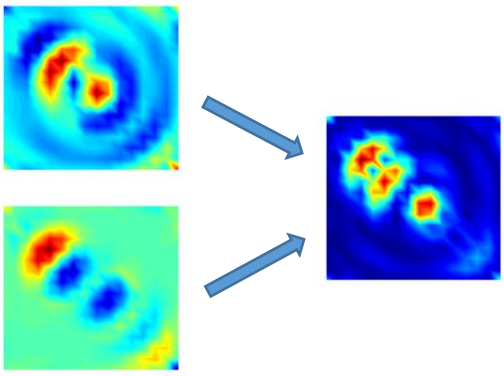

Figure 6.20 Combine 1st and 2nd F-VAC components at 460 Hz (see figure 6.14 (b)).

6.5 Comparison of noise reduction results

In this chapter, we will examine F-VAC analysis's application in structure borne noise control. In order to evaluate its effectiveness, the noise reduction results are compared with traditional modal analysis based approach. The dominant vibration shapes need to be suppressed are already determined in section 6.4. However, the corresponding normal mode shapes are still need to identified.

In this experiment, normal modes of the test object are identified through experimental modal analysis based on normal surface velocities measured by laser vibrometer. The test setup is the same with F-VAC analysis (see figure 6.1). The difference is that the excitation signal is changed to white noise. The resonant frequencies are acquired by analyzing peaks of vibration response spectrum. The 32 directly measured normal surface velocities forms the corresponding modal shapes. In order to get more smooth mode shapes, normal surface velocities at 256 points are reconstructed by using equation 3.19. It need to be emphasize again that such an operation requires precise measurement of phase information. The reference microphone placed in the near-field is crucial important for velocity reconstruction.

Normal modes that are closest to certain frequencies of interest are chosen to be the vibration shapes that need to be suppressed. So, mode shape at 201 Hz are chosen to control sound radiation at 240 Hz, mode shape at 300 Hz are chosen to control sound radiation at 272 Hz, mode shape at 377 Hz are chosen to control sound radiation at 340 Hz and mode shape at 468 Hz are chosen to control sound radiation at 460 Hz. The vibration response of modal analysis and these selected normal mode shapes are shown in figure 6.21.

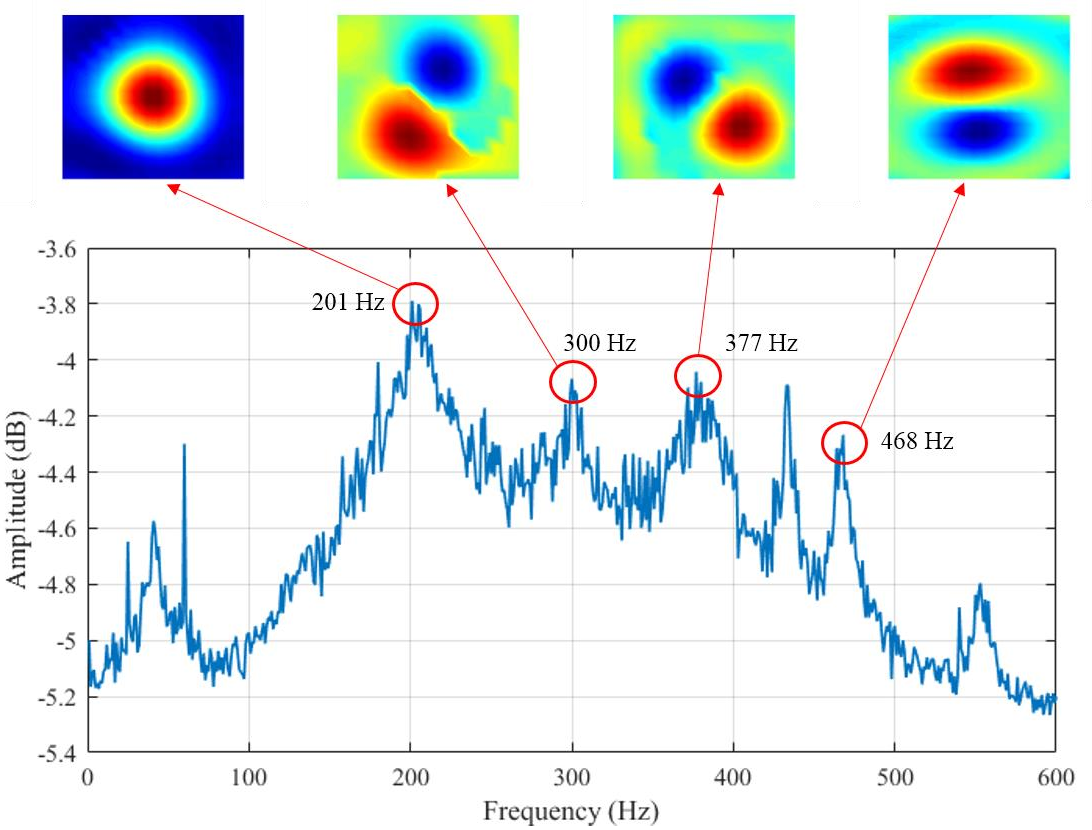

Figure 6.21 Selected normal modes of the test object

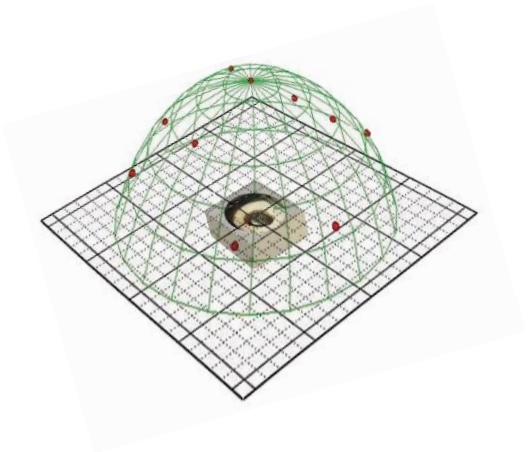

Figure 6.22 Far-field measurement points for sound power calculation

TABLE 6.3 Coordinates of sound power measurement locations

Point index	*x*	*y*	*z*
1	-0.52	0.23	0.20
2	-0.20	0.35	0.45
3	0.08	0.56	0.20
4	0.45	0.35	0.20
5	0.40	0.00	0.45
6	0.45	-0.35	0.20
7	0.08	-0.56	0.20
8	-0.20	-0.35	0.45
9	-0.52	-0.22	0.20
10	0.00	0.00	0.60

A common approach to vibration suppression without modifying structure is adding damping. So, to suppress the dominant vibration components obtained from F-VAC analysis and modal analysis respectively, several vibration damping patches are attached to the peak locations of corresponding shapes. See figure 6.23.

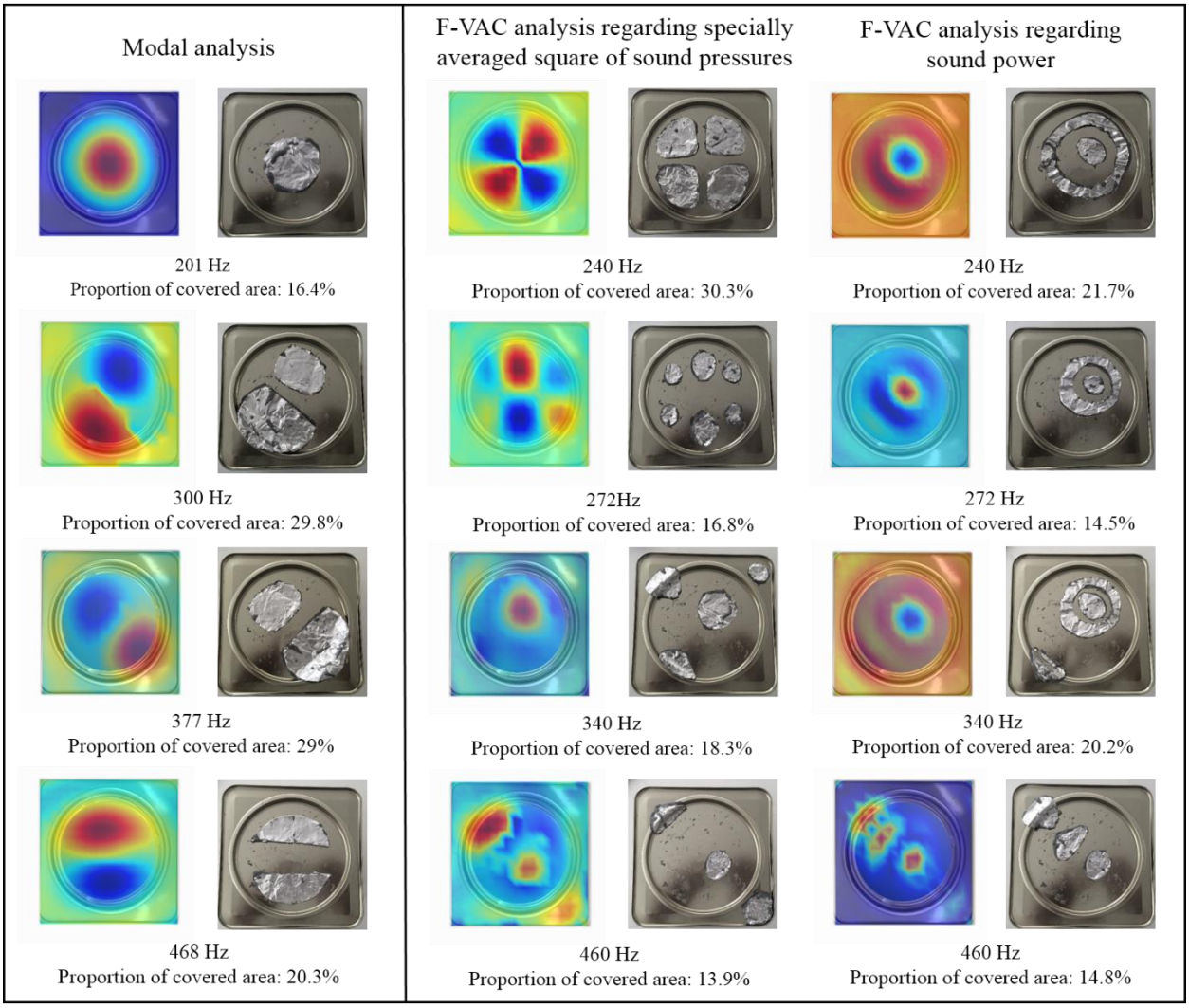

Figure 6.23 Modifications with respect to 12 different scenarios

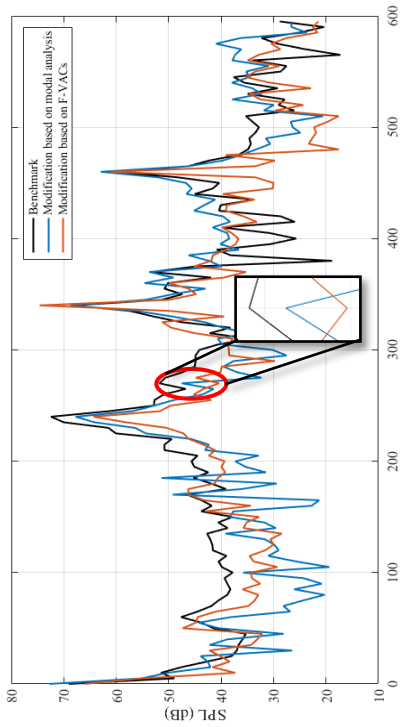

(a) Noise reduction targeting at 240 Hz

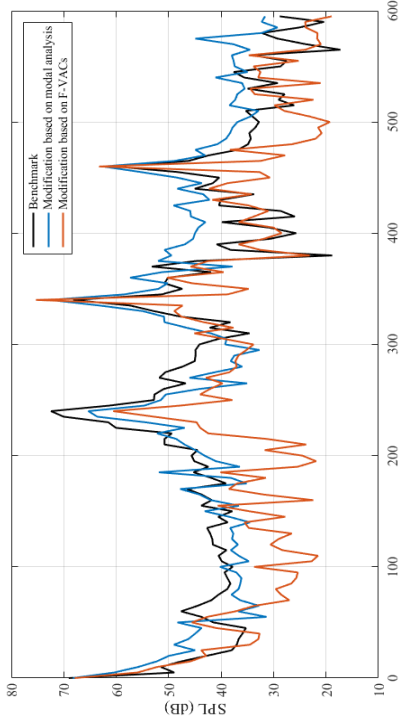

(b) Noise reduction targeting at 272 Hz

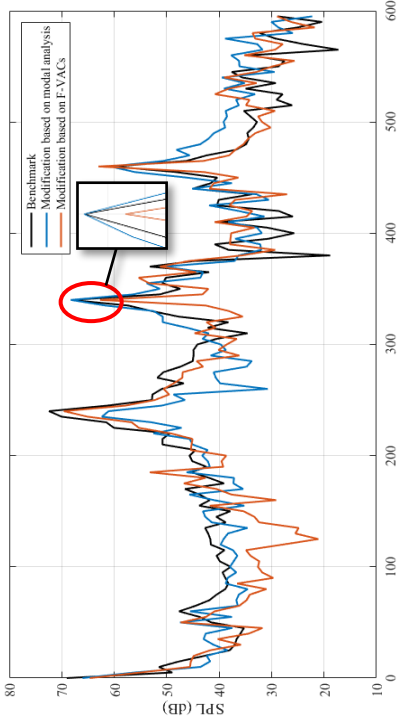

(c) Noise reduction targeting at 340 Hz

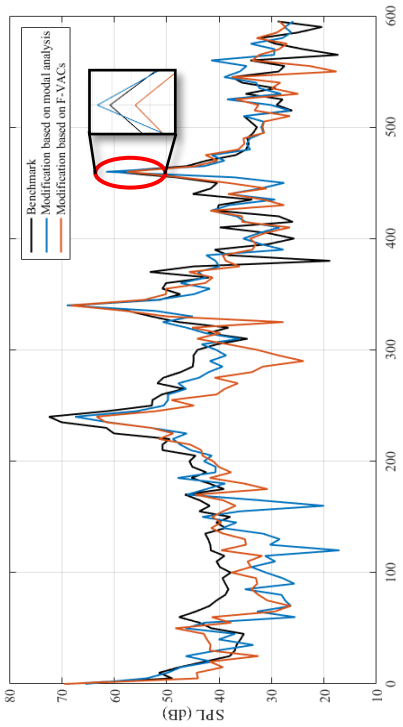

(d) Noise reduction targeting at 460 Hz

Figure 6.24 Comparisons of noise control results targeting at spatially averaged square of sound pressures

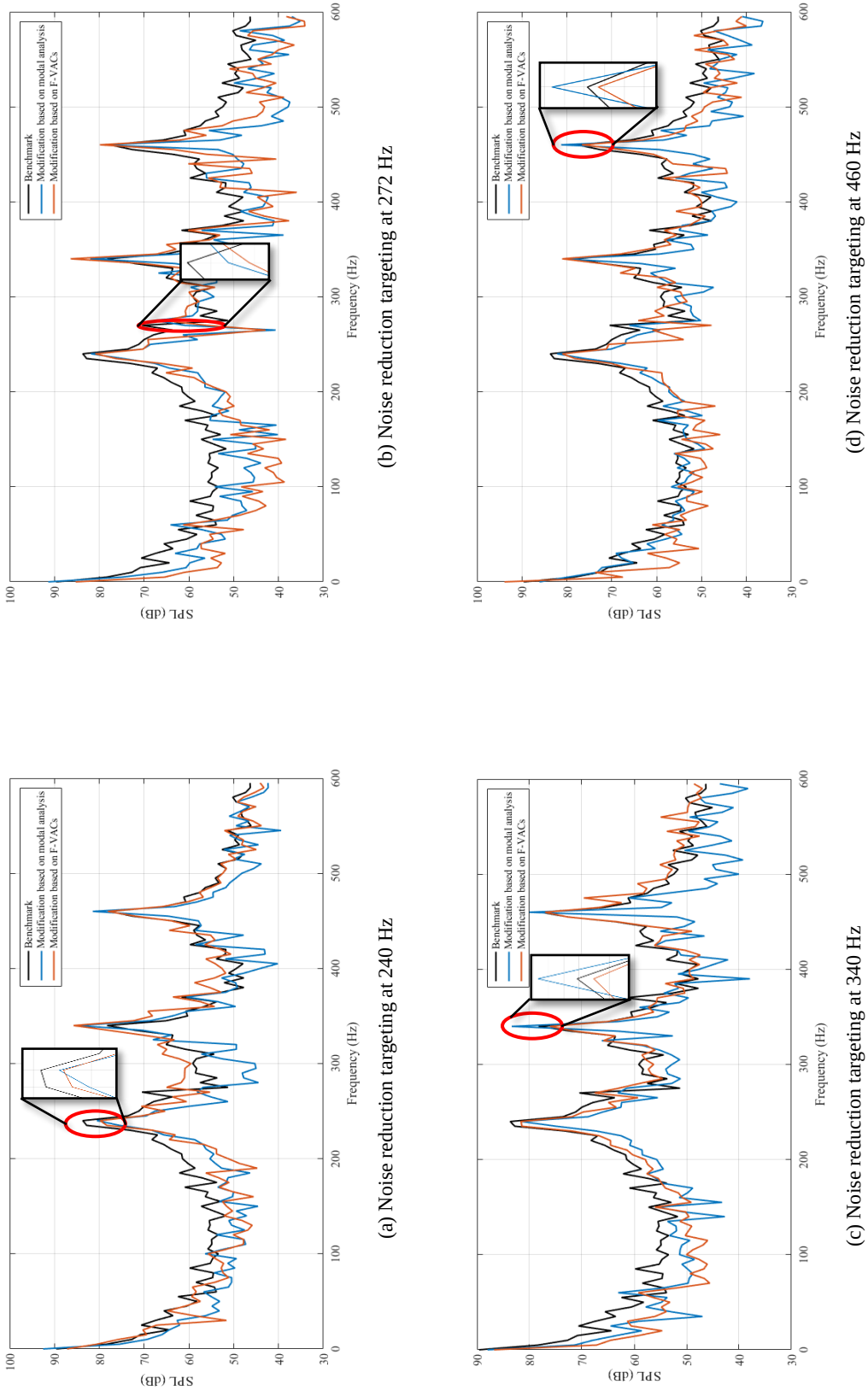

(a) Noise reduction targeting at 240 Hz

(b) Noise reduction targeting at 272 Hz

(c) Noise reduction targeting at 340 Hz

(d) Noise reduction targeting at 460 Hz

Figure 6.25 Comparisons of noise control results targeting at sound power

In figure 6.24, the spatially averaged square of sound pressures of modifications per F-VAC analysis and modal analysis are compared with benchmark data in narrow bands. And in figure 6.25, total radiated sound power of modifications per F-VAC analysis and modal analysis are compared with benchmark data in narrow bands. Detailed dB changes of each comparison are listed in table 6.4.a and table 6.5.a. The positive value indicates noise reduction with respect to benchmark data, on the contrary, negative value indicates increase in sound radiation. By subtracting modal analysis's dB changes from F-VAC's results, the net differences are shown in the third row.

TABLE 6.4.a dB changes of noise control targeting at spatially averaged square of sound pressures

	240 Hz	272 Hz	340 Hz	460 Hz
Modal analysis	7.2 dB	4.4 dB	0.3 dB	-1 dB
F-VAC analysis	11.9 dB	11.5 dB	6.3 dB	3.7 dB
Net enhancement	4.7 dB	7.1dB	6 dB	4.7 dB

TABLE 6.4.b Proportion of covered area for noise control targeting at spatially averaged square of sound pressures

	240 Hz	272 Hz	340 Hz	460 Hz
Modal analysis	16.4%	29.8%	29%	20.3%
F-VAC analysis	30.3%	16.8%	18.3%	13.9%
Net difference	13.9%	-13%	-10.7%	-6.4%

TABLE 6.5.a dB changes of noise control targeting at sound power radiation

	240 Hz	272 Hz	340 Hz	460 Hz
Modal analysis	3.2 dB	9.5 dB	-5.1 dB	-3.5 dB
F-VAC analysis	4 dB	14.3 dB	2 dB	1 dB
Net enhancement	0.8 dB	4.8 dB	7.1 dB	4.5 dB

TABLE 6.5.b Proportion of covered area for noise control targeting at sound power radiation

	240 Hz	272 Hz	340 Hz	460 Hz
Modal analysis	16.4%	29.8%	29%	20.3%
F-VAC analysis	21.7%	14.5%	20.2%	14.8%
Net difference	5.3%	-15.3%	-8.8%	-5.5%

In the first comparative test, for spatially averaged square value of sound pressures at 240 Hz, 11.9 dB of noise is eliminated through F-VAC analysis whereas that the suppression of nearest normal mode only gets 7.2 dB drop. Similarly, for 272 Hz, vibration suppression based on modal analysis lead to 4.4 dB reduction, in contrast, F-VAC based approach provides 11.5 dB level reduction. For the other two cases, vibration control per nearest mode shape did not cause much dB changes. The sound radiation at 460 Hz becomes even louder than original benchmark case. However, F-VAC analysis give out much better noise reduction results.

In the second comparative test, which targeting at reducing total radiated sound power, similar results are obtained, yet with lower level. For the comparisons at 340 Hz and 460 Hz, modifications based on modal analysis even increase the sound power by 5.1 dB and 3.5 dB respectively, which further proved the ineffectiveness of modal analysis's application in structure borne noise control.

Generally speaking, for both two group of experiments, the noise reduction results of 340 Hz and 460 Hz is not as good as 240 Hz and 272 Hz. It is because that in the original cases, most of the energy is concentrated upon 200 Hz ~ 300 Hz, which undoubtedly provide greater noise reduction potential. In addition, by suppressing the vibration patterns in the form of adding damping tapes, the effect is limited. This also causes the relatively poor results at 340 Hz and 460 Hz.

Another factor needs to be considered is the percentage of area covered by damping pads. In these experiments, sizes and locations of damping pads are determined from corresponding

target vibration components, so, proportions of covered area are different. These percentages for 12 scenarios are indicated in figure 6.23 and summarized in table 6.4.b and table 6.5.b. In the first group of experiments target at 240 Hz, modification according to modal analysis covered less area than F-VAC analysis cases. One may think that the better results of F-VAC analysis are because that more damping pads are used in those cases. However, in the other three groups of experiments, modifications per modal analysis utilize more damping pads than F-VAC analysis yet give out poor noise reduction results. So, the key factor is not how many damping pads are used, but whether these damping pads are placed in the right places. This from another perspective shows the importance of F-VAC analysis which could reveal the true vibration component needs to be suppressed.

These results demonstrate that dominant vibration component responsible for sound radiation at certain frequency is not necessarily to be the dominant mode shapes. Instead, impacts of every vibration patterns to sound radiation must be taken into a "comprehensive consideration", which can be achieved through F-VAC analysis. This is because that, theoretically, each F-VAC consists of contributions from infinite number of vibration patterns.

6.6 Conclusion

The series experiments demonstrated in this chapter show the flexibility of modified HELS based NAH and the power of F-VAC analysis in structure borne noise control. In the experiment, the whole vibro-acoustic field are reconstructed from partial normal surface velocity measurements supplemented with several verification sound pressure measurements. These successful reconstructions have profound influence on practical application of NAH because it broads NAH's implementation in scenarios when you cannot obtain vibro-acoustic quantities over the entire surface. Recall from numerical simulation with respect to different measurement locations in section 4.4.2, the measurement locations should cover as large area as possible and

the ratio of covered area to entire area is recommended no less than 0.5. In other words, although the proposed approach could do reconstruction based on partial normal surface velocity measurement, the measurement area could not be too small.

CHAPTER 7: CONCLUSIONS AND FURTHER WORKS

7.1 Conclusion

This dissertation presents an innovative vibro-acoustic response reconstruction technique and further introduces the concept of F-VAC analysis. Combination of these two methods enables one to diagnose and control structure borne sound in the most cost-effective manner.

The modified HELS method based on normal surface velocities supplemented with few field sound pressures is a new extension of HELS theory. By changing the input data from nearfield sound pressures to normal surface velocities, the data acquisition procedures are significantly simplified. What's more, the proposed modified HELS approach also shows its ability to reconstruct vibro-acoustic field based on partial data of normal surface velocities. Such feasibility extends its application to situations when there are immobile obstacle parts around vibrating surface that stop us from obtaining either near-field sound pressures or normal surface velocities near these locations.

Based on the interrelationships established by modified HELS method, the procedures of F-VAC analysis are introduced. The thus obtained F-VAC components give out intuitive guidance for engineers to solve structure borne noise problem in a smart way. An experimental study is conducted with respect to the top surface of a cookie box. Through comparison with benchmark data, the effectiveness of modified HELS approach is validated. Through comparison with traditional modal analysis based approach, the advantage of F-VAC analysis based structure borne noise control is shown.

7.2 Future work

As an inverse problem like NAH, no matter what kind of approach is used, when come to practical implementation, the first and foremost task is always regularization. The core content of HELS theory is making best approximation by matching measured data to priori assumptions. In

practice, no matter how many measurements are taken, what you could get are always limited discrete information. What's more, the limited input data, including acoustic quantity and structure geometry information, are inevitably contaminated with measurement errors. During reconstruction, such discrepancies will be exaggerated and might lead to unbounded reconstruction results. Our current solution to this is to supplement several verification sound pressure measurements in the field and apply a low-pass filter in wavenumber domain. The numerical simulations and experimental tests show the effectiveness of this approach. However, the shortcoming of this approach is the increasing of computational load, which is especially true for large number of measurement points. So, future work should focus on developing new regularization strategy which could ease the computational load yet still maintain high reconstruction accuracy.

Considering about time and resource available, the current experimental validation is conducted with respect to a cookie box, which is not a real industrial product. To further validate the effectiveness in industrial applications, more experiments could be conducted regarding real industrial parts such as gearbox, car engine, muffler etc.

REFERENCES

1 Ewins, David J. Modal testing: theory and practice. Vol. 15. Letchworth: Research studies press, 1984.

2 Schwarz, Brian J., and Mark H. Richardson. "Experimental modal analysis." CSI Reliability week 35.1 (1999): 1-12.

3 Peeters, Bart, and Guido De Roeck. "Reference-based stochastic subspace identification for output-only modal analysis." Mechanical systems and signal processing 13.6 (1999): 855-878.

4 Peeters, Bart, and Guido De Roeck. "Stochastic system identification for operational modal analysis: a review." Journal of Dynamic Systems, Measurement, and Control 123.4 (2001): 659-667.

5 Maidanik, Gideon. "Response of ribbed panels to reverberant acoustic fields." the Journal of the Acoustical Society of America 34.6 (1962): 809-826.

6 Wallace, C. E. "Radiation resistance of a baffled beam." The Journal of the Acoustical Society of America 51.3B (1972): 936-945.

7 Wallace, C. E. "Radiation resistance of a rectangular panel." The Journal of the Acoustical Society of America 51.3B (1972): 946-952.

8 Gomperts, M. C. "Radiation from rigid baffled, rectangular plates with general boundary conditions." Acta Acustica united with Acustica 30.6 (1974): 320-327.

9 Heckl, M. "Radiation from plane sound sources." Acta Acustica united with Acustica 37.3 (1977): 155-166.

10 Leppington, F. G., E. G. Broadbent, and K. H. Heron. "The acoustic radiation efficiency of rectangular panels." Proceedings of the Royal Society of London A: Mathematical, Physical and Engineering Sciences. Vol. 382. No. 1783. The Royal Society, 1982.

11 Williams, Earl G. "A series expansion of the acoustic power radiated from planar sources." The Journal of the Acoustical Society of America 73.5 (1983): 1520-1524.

12 Keltie, R. F., and H. Peng. "The effects of modal coupling on the acoustic power radiation from panels." ASME, Transactions, Journal of Vibration, Acoustics, Stress, and Reliability in Design 109 (1987): 48-54.

13 Snyder, Scott D., and Nobuo Tanaka. "Calculating total acoustic power output using modal radiation efficiencies." The Journal of the Acoustical Society of America 97.3 (1995): 1702-1709.

14 Li, Wen L., and Howard J. Gibeling. "Acoustic radiation from a rectangular plate reinforced by springs at arbitrary locations." Journal of sound and vibration 220.1 (1999): 117-133.

15 Naghshineh, Koorosh, Gary H. Koopmann, and Ashok D. Belegundu. "Material tailoring of structures to achieve a minimum radiation condition." The Journal of the Acoustical Society of America 92.2 (1992): 841-855.

16 Koopmann, Gary H., and John B. Fahnline. Designing quiet structures: a sound power minimization approach. Academic Press, 1997.

17 Fuller, Christopher R. "Active control of sound transmission/radiation from elastic plates by vibration inputs: I. Analysis." Journal of Sound and Vibration 136.1 (1990): 1-15.

18 Metcalf, V. L., et al. "Active control of sound transmission/radiation from elastic plates by vibration inputs, II: experiments." Journal of sound and vibration 153.3 (1992): 387-402.

19 Maillard, J. P., and C. R. Fuller. "Active control of sound radiation from cylinders with piezoelectric actuators and structural acoustic sensing." Journal of Sound and Vibration 222.3 (1999): 363-387.

20 Vipperman, J. S., R. A. Burdisso, and C. R. Fuller. "Active control of broadband structural vibration using the LMS adaptive algorithm." Journal of Sound and Vibration 166.2 (1993): 283-299.

21 Fahy, F. J. "Some applications of the reciprocity principle in experimental vibroacoustics." Acoustical Physics 49.2 (2003): 217-229.

22 Van der Linden, P. J. G., and J. K. Fun. Using mechanical-acoustic reciprocity for diagnosis of structure borne sound in vehicles. No. 931340. SAE Technical Paper, 1993.

23 Hald, Jørgen, and Jakob Mørkholt. "Panel Contribution Analysis in a vehicle cabin using a dual layer handheld array with integrated position measurement." SAE International Journal of Passenger Cars-Mechanical Systems 2.2009-01-2171 (2009): 1458-1469.

24 Metherell, Alexander F., et al. "Introduction to acoustical holography." The Journal of the Acoustical Society of America 42.4 (1967): 733-742.

25 Williams, Earl G., and J. D. Maynard. "Holographic imaging without the wavelength resolution limit." Physical review letters 45.7 (1980): 554.

26 Williams, Earl G., and J. D. Maynard. "Numerical evaluation of the Rayleigh integral for planar radiators using the FFT." The Journal of the Acoustical Society of America 72.6 (1982): 2020-2030.

27 Maynard, Julian D., Earl G. Williams, and Y. Lee. "Nearfield acoustic holography: I. Theory of generalized holography and the development of NAH." The Journal of the Acoustical Society of America 78.4 (1985): 1395-1413.

28 Veronesi, W. A., and J. Do Maynard. "Nearfield acoustic holography (NAH) II. Holographic reconstruction algorithms and computer implementation." The Journal of the Acoustical Society of America 81.5 (1987): 1307-1322.

29 Williams, Earl G., Henry D. Dardy, and Karl B. Washburn. "Generalized nearfield acoustical holography for cylindrical geometry: Theory and experiment." The Journal of the Acoustical Society of America 81.2 (1987): 389-407.

30 Williams, Earl G., Brian H. Houston, and Joseph A. Bucaro. "Broadband nearfield acoustical holography for vibrating cylinders." The Journal of the Acoustical Society of America 86.2 (1989): 674-679.

31 Bernhard, R. J. "A noise source identification technique using an inverse Helmholtz integral equation method." (1988).

32 Veronesi, W. A., and J. D. Maynard. "Digital holographic reconstruction of sources with arbitrarily shaped surfaces." The Journal of the Acoustical Society of America 85.2 (1989): 588-598.

33 Huang, Yanmin. "Computer Techniques for Three-Dimensional Source Radiation." (1990).

34 Bai, Mingsian R. "Application of BEM (boundary element method)-based acoustic holography to radiation analysis of sound sources with arbitrarily shaped geometries." The Journal of the Acoustical Society of America 92.1 (1992): 533-549.

35 Wang, Zhaoxi, and Sean F. Wu. "Helmholtz equation–least-squares method for reconstructing the acoustic pressure field." The Journal of the Acoustical Society of America 102.4 (1997): 2020-2032.

36 Wu, Sean F. "On reconstruction of acoustic pressure fields using the Helmholtz equation least squares method." The Journal of the Acoustical Society of America 107.5 (2000): 2511-2522.

37 Rayess, Nassif, and Sean F. Wu. "Experimental validations of the HELS method for reconstructing acoustic radiation from a complex vibrating structure." The Journal of the Acoustical Society of America 107.6 (2000): 2955-2964.

38 Wu, Sean F. "Hybrid near-field acoustic holography." The Journal of the Acoustical Society of America 115.1 (2004): 207-217.

39 Wu, Sean F., Huancai Lu, and Manjit S. Bajwa. "Reconstruction of transient acoustic radiation from a sphere." The Journal of the Acoustical Society of America 117.4 (2005): 2065-2077.

40 Wu, Sean F., and Logesh Kumar Natarajan. "Panel acoustic contribution analysis." The Journal of the Acoustical Society of America 133.2 (2013): 799-809.

41 Wu, Sean F. "On reconstruction of acoustic pressure fields using the Helmholtz equation least squares method." The Journal of the Acoustical Society of America 107.5 (2000): 2511-2522.

42 Isakov, Victor, and Sean F. Wu. "On theory and application of the Helmholtz equation least squares method in inverse acoustics." Inverse Problems 18.4 (2002): 1147.

43 Loyau, Thierry, Jean-Claude Pascal, and Paul Gaillard. "Broadband acoustic holography reconstruction from acoustic intensity measurements. I: Principle of the method." The Journal of the Acoustical Society of America 84.5 (1988): 1744-1750.

44 Jacobsen, Finn, and Yang Liu. "Near field acoustic holography with particle velocity transducers a." The Journal of the Acoustical Society of America 118.5 (2005): 3139-3144.

45 Leclère, Quentin, and Bernard Laulagnet. "Nearfield acoustic holography using a laser vibrometer and a light membrane." The Journal of the Acoustical Society of America 126.3 (2009): 1245-1249.

46 Harris, Michael C., Jonathan D. Blotter, and Scott D. Sommerfeldt. "Obtaining the complex pressure field at the hologram surface for use in near-field acoustical holography when pressure and in-plane velocities are measured." The Journal of the Acoustical Society of America 119.2 (2006): 808-816.

47 Zhang, Yong-Bin, et al. "Near field acoustic holography based on the equivalent source method and pressure-velocity transducers." The Journal of the Acoustical Society of America 126.3 (2009): 1257-1263.

48 P. Castellini, G. Revel, and E. Tomasini, "Laser Doppler vibrometer: a review of advances and applications," The Shock and vibration digest 30, 443-456 (1998).

49 Zhu, Wu. "Helmholtz Equation Least Squares Based Near-Field Acoustic Holography With Laser." (2016).

50 Chen, Lingguang, and Sean F. Wu. "Development of smart noise control technology." The Journal of the Acoustical Society of America 139.4 (2016): 2012-2012.

51Morais, Joao, H. T. Le, and Marco Antonio Pérez-de la Rosa, "Quaternionic spherical wave functions," Mathematical Methods in the Applied Sciences 39, 5118-5130 (2016).

52 Huancai Lu, and Sean F. Wu. "Reconstruction of vibroacoustic responses of a highly non-spherical structure using Helmholtz equation least-squares method," J. Acoust. Soc. Am. 125, 1538-1548 (2009).

53 L. K. Natarajan, et al. "Vibro-acoustic analysis of an arbitrarily shaped vibrating structure," J. Acoust. Soc. Am. 126, 2244-2244 (2009).

54 Tikhonov, Andreĭ Nikolaevich, and Vasiliĭ ÎAkovlevich Arsenin. Solutions of ill-posed problems. Vol. 14. Washington, DC: Winston, 1977.

55 E. G. Williams, "Regularization methods for near-field acoustical holography," J. Acoust. Soc. Am. 110, 1976-1988 (2001).

56 Tikhonov, Andrey. "Solution of incorrectly formulated problems and the regularization method." Soviet Math. Dokl.. Vol. 5. 1963.

57 Landweber, Louis. "An iteration formula for Fredholm integral equations of the first kind." American journal of mathematics 73.3 (1951): 615-624.

58 Kirsch, Andreas. An introduction to the mathematical theory of inverse problems. Vol. 120. Springer Science & Business Media, 2011.

59 G. B. Warburton, "The vibration of rectangular plates." Proceedings of the Institution of Mechanical Engineers 168, 371-384 (1954).

60 Leissa, Arthur W. Vibration of shells. New York: Acoustical Society of America, 1993.

61 Wu, Sean F. "The Helmholtz Equation Least-Squares Method." The Helmholtz Equation Least Squares Method. Springer New York, 2015. 27-62.

62 Lu, Huancai, and Sean F. Wu. "Reconstruction of vibroacoustic responses of a highly nonspherical structure using Helmholtz equation least-squares method." The Journal of the Acoustical Society of America 125.3 (2009): 1538-1548.

63 S.F. Wu, "On reconstruction of acoustic pressure fields using the Helmholtz equation least squares method," J. Acoust. Soc. Am. 107, 2511–2522 (2000).

64 Isakov, Victor, and Sean F. Wu. "On theory and application of the Helmholtz equation least squares method in inverse acoustics." Inverse Problems 18.4 (2002): 1147.

ABSTRACT

AN EFFECTIVE METHODOLOGY FOR SUPPRESSING STRUCTURE-BORNE SOUND RADIATION

by

LINGGUANG CHEN

December 2017

Advisor: Dr. Sean F. Wu

Major: Mechanical Engineering

Degree: Doctor of Philosophy

This dissertation is primarily concerned with the development of an effective methodology for reducing structure-borne sound radiation from an arbitrarily shaped vibrating structure. There are three major aspects that separate the present methodology from all the previous ones. Firstly, it is a non-contact and non-invasive approach, which is applicable to a class of vibrating structures encountered in engineering applications. Secondly, the input data consists of a combined normal surface velocity distribution on a portion of a vibrating surface and the radiated acoustic pressure at a few field points. The normal surface velocities are measured by using a laser vibrometer over a portion of the structural surface accessible to a laser beam, while the field acoustic pressures are measured by a small array of microphones. The normal surface velocities over the rest surface of the vibrating structure are reconstructed by using the Helmholtz Equation Least Squares (HELS) method. Finally, the acoustic pressures are correlated to structural vibration by decomposing the normal surface velocity into the forced-vibro-acoustic components (F-VAC). These F-VACs are mutually orthogonal basis functions that can uniquely describe the normal surface velocity. The weightings of these F-VACs represent the relative contributions of structural vibrations into the

sound radiation. This makes it possible to suppress structure-borne acoustic radiation in the most cost-effective manner simply by controlling the key F-VACs of a vibrating structure. The effectiveness of the proposed methodology for reducing structure-borne acoustic radiation is examined numerically and experimentally, and compared with those via traditional experimental modal analyses. Results have demonstrated that the proposed methodology enables one to reduce much more acoustic radiation at any selected target frequencies than the traditional approach.

AUTOBIOGRAPHICAL STATEMENT

LINGGUANG CHEN

EDUCATION

2013-present Ph.D. of Mechanical Engineering; Wayne State University, Detroit, MI

2010-2013 Master of Vehicle Engineering, Zhejiang University, Hangzhou, China

2006-2010 Bachelor of Mechanical Engineering, Yangtze University, Jingzhou, China

JOURNAL PUBLICATIONS

1. Chen, Lingguang, Sean F. Wu, Yong Xu, William D. Lyman, and Gaurav Kapur. "Calculating Blood Pressure Based on Measured Heart Sounds." Journal of Computational Acoustics (2017): 1750014.
2. Chen, Lingguang, Sean F. Wu, Yong Xu, William D. Lyman, and Gaurav Kapur. "Blind separation of heart sounds." Journal of Computational Acoustics (2017): 1750035.
3. Chen, Lingguang, Sean F. Wu. “Reconstructing vibro-acoustic responses of a vibrating structure based on partial data of the normal surface velocity and field acoustic pressure.” in preparation.
4. Chen, Lingguang, Sean F. Wu. “Structure-borne noise control based on vibro-acoustic analysis.” in preparation.

CONFERENCE PROCEEDINGS

1. Chen, Lingguang, Sean F. Wu, Yong Xu, William D. Lyman, and Gaurav Kapur. "Blind separation of heart sounds." The Journal of the Acoustical Society of America 137, no. 4 (2015): 2388-2388.
2. Chen, Lingguang, Sean F. Wu, Yong Xu, William D. Lyman, and Gaurav Kapur. "Estimating blood pressures based on directly measured heart sounds." The Journal of the Acoustical Society of America 139, no. 4 (2016): 2224-2224.
3. Chen, Lingguang, and Sean F. Wu. "Development of smart noise control technology." The Journal of the Acoustical Society of America 139, no. 4 (2016): 2012-2012.